EVALUATING SELF-SEGREGATION OF SEMINAL FLUID COMPONENTS VIA SURFACE-ENHANCED RAMAN SPECTROSCOPY

A thesis presented to the faculty of the Graduate School of Western Carolina University in partial fulfillment of the requirements for the degree of Master of Science in Chemistry

By

Michael Anthony Bond

Director: Dr. David D. Evanoff, Jr.

Associate Professor of Chemistry

Department of Chemistry & Physics

Committee Members:

Dr. Carmen L. Huffman, Chemistry & Physics

Dr. Scott W. Huffman, Chemistry & Physics

July 8, 2020

ACKNOWLEDGEMENTS

I would like to thank my advisor Dr. Evanoff for all of the guidance he has given me over the course of this project. I am extremely grateful for the privilege to work under an advisor who goes about his work with such enthusiasm and dedication. As I continue my chemistry career, I will strive to approach challenges with the same levels of insight and patience that he has shown. I would also like to thank my thesis committee members, Dr. Carmen Huffman and Dr. Scott Huffman, for all of the valuable lessons and perspectives they taught me both in class and during committee meetings. I extend my gratitude to the rest of the faculty and staff of the Chemistry and Physics Department, for their many contributions to the great experience I have had at Western.

I also want to thank my extended family, my parents, my brother Kyle, and my dog Mimi for all of the emotional (and financial) support, and for always believing in me. A very special thank you to David Song, for all of the support you've given me. I would also like to thank my friends in the graduate Chemistry program at Western, especially Jesse Ingham, Cecilia Baumgardner, and Daniel Free, who helped make this a wonderful past two years.

I want to again thank everyone above for the resilience, reliability, and understanding they have all shown during the ongoing COVID-19 pandemic; the completion of this document would not have been possible without all of you.

Lastly, I would like to thank the National Institute of Justice for grant (2015-NE-BX-K003), and the National Science Foundation (CHE-1040163) for funding the Raman spectrometer.

TABLE OF CONTENTS

LIST OF TABLES

LIST OF FIGURES

LIST OF ABBREVIATIONS

SAKs ..... sexual assault kits
PSA ..... prostate-specific antigen
SERS ..... surface-enhanced Raman spectroscopy
AgNPs ..... silver nanoparticles
CRR ..... constant radius regime
CCAR ..... constant contact angle regime
CCD ..... charge-coupled device
FT-IR ..... Fourier transform infrared (spectroscopy)
CAH ..... contact angle hysteresis
CV ..... coefficient of variation
SSD ..... sample standard deviation
AEF ..... analytical enhancement factor
IRAS ..... infrared reflective absorbance spectroscopy
SSR ..... sum of the square of the residuals

ABSTRACT

EVALUATING SELF-SEGREGATION OF SEMINAL FLUID COMPONENTS VIA SURFACE-ENHANCED RAMAN SPECTROSCOPY

Michael Anthony Bond, M. S.

Western Carolina University (July 2020)

Director: Dr. David D. Evanoff, Jr.

In recent years, Raman spectroscopy has proven to be a promising confirmatory test for seminal fluid found in sexual assault kits. Perhaps the main disadvantage to using Raman spectroscopy in this context is low signal, which results from both the low probability of Raman-scattered photons and the common scenario of trace amounts of analytes in forensic casework. Signal quality can be dramatically increased by way of surface-enhanced Raman spectroscopy (SERS), which can be done by growing silver nanoparticles (AgNPs) on nylon swab fibers. In order to establish this method as a confirmatory test, the nature of the adsorption of seminal fluid on silver needs to be understood. The following details a study involving fabrication of several AgNP-coated substrates, whose extents of percolation and surface wettabilities were determined. Findings from those experiments were used to explain trends in SERS signals and stain shapes from semen simulant and true semen samples deposited on these substrates. The percolation threshold was achieved at 15 nm thicknesses when grown thermally, and 61-minute reaction time when grown chemically. The thermally-grown layers were consistently more hydrophobic than the chemically-grown layers, which had a significant influence on stain spreading and shape.

SERS data showed that all droplets containing choline exhibited a drastic and statistically-significant increase in droplet spreading on AgNP-coated surfaces, which may have been the result of a chemical reaction between choline and silver. SERS semen spectra were also compared to a previous study conducted in this lab wherein SERS spectra of semen were collected on AgNP-coated swabs. By comparing residuals between semen spectra from the previous study and the current study, the SERS spectra collected on the swabs were assigned tentative locations along semen stains prepared on substrates fabricated for this study.

CHAPTER 1: BACKGROUND

1.1 Confirmatory testing of seminal fluid

Currently in the United States there is a large volume of sexual assault kits (SAKs) that are backlogged,[1] meaning samples have been collected and submitted to a crime lab for analysis but have yet to be tested. A contributing factor to the backlog is the significant time and resources involved in analyzing swabbed samples of bodily fluids included in a SAK. When evidence is suspected to include bodily fluids, the forensic scientist conducts a presumptive test to classify the evidence as a potential bodily fluid; if the test suggests the sample may be a bodily fluid, the scientist follows up with a confirmatory test to identify the specific fluid.[2] These confirmatory tests are specific to a single bodily fluid.[3] If a confirmatory test result is negative, enough sample must remain to conduct more confirmatory tests. Figure 1 shows an example of this process of choosing different confirmatory tests for semen, blood, and saliva. Due to the binary nature of these tests, definitive identification of these fluids involves iteration through these different tests until a positive result is reached. As a result, confirmatory testing of bodily fluid samples becomes very time-consuming.

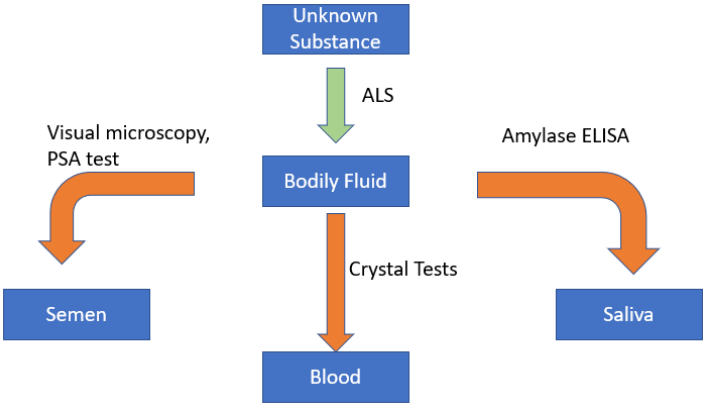

Figure 1: Presumptive (green) and confirmatory (orange) tests for bodily fluids. ALS = alternate light source, PSA = prostate-specific antigen, ELISA = enzyme-linked immunosorbent assay.

Additionally, confirmatory tests may not always be accurate or appropriate for all scenarios with a specific bodily fluid. For example, the current methods for confirmatory testing of semen are visual microscopy and prostate-specific antigen (PSA) testing.[3] Visual microscopy is the default confirmatory test because of its ease of use, as sperm cells have a very distinct morphology. This is usually done by performing the so-called Christmas Tree stain, wherein the heads of sperm cells are dyed red and the tails are dyed green. However, in cases where the donor has had a vasectomy or for any other reason has little to no sperm count (respectively referred to as oligospermia and azoospermia), visual inspection is not sufficient testing for definitive identification. In cases of azoospermia, immunological testing is used to detect the presence of PSA. Not only is this destructive to the sample, but it also has been shown to be especially prone to false positives. In one study, Lehrer et al. demonstrated that certain strains of cancers express elevated levels of PSA; these could easily lead to a positive result for PSA testing using this method.[4,5] Based on the current state of confirmatory testing methods, there is a

pressing need for accurate, rapid, and non-destructive confirmatory testing of semen. This need may be sufficiently addressed by Raman spectroscopy.

1.2 Raman spectroscopy

1.2.1 Fundamentals

When light is incident to the surface of the material, the material can deflect the light and cause it to propagate along a different trajectory; this process is known as scattering. Light can scatter from a surface either elastically, with no change in energy of the photon upon collision, or inelastically, with energy transferring between the photon and the material. Perhaps the most familiar example of elastic scattering of light is Rayleigh scattering, which occurs when the light scatters off of a particle much smaller than its wavelength, and is responsible for the blue color of the sky.[6] Raman scattering, a type of inelastic scattering, is possible because the energy transferred during the inelastic collisions corresponds to an energy transition in the material.[6] If the energy is transferred from the photon to the material, such that the photon scatters with less energy than it had originally, the process is called Stokes-shifted Raman. Conversely, if the material transfers energy to a photon upon collision, then the process is called anti-Stokes Raman. These transitions can be thought of as absorptions to and emissions from a "virtual" energy state that does not correspond to an actual energy level in the material. Jablonski diagrams depicting energy changes during different scattering events is shown in Figure 2 below. When using a light source in the visible range, this two-step process results in a net change in energy in the material between the ground state and a vibrational excited state.

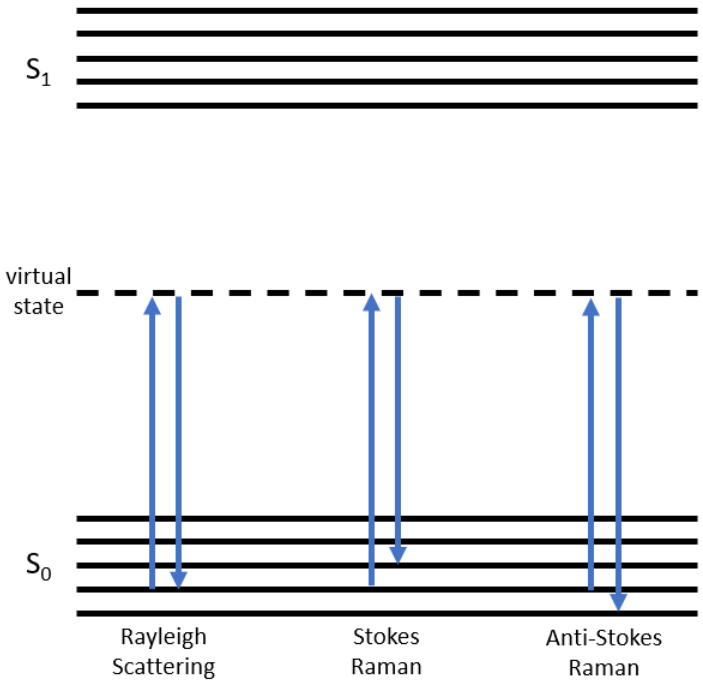

Figure 2: From left to right, Jablonski diagrams for Rayleigh scattering, Stokes Raman scattering, and anti-Stokes Raman scattering. Here, s_i corresponds to singlet states, where s_0 is the electronic ground state and s_1 is the first electronic excited state.

When Stokes-scattered photons are detected by a Raman spectrometer, the energy of the incident light (a laser) is compared to the energy of the scattered photons, and the difference is calculated in wavenumbers. Since the difference is with respect to the incident energy, these values are referred to as Raman shift or relative wavenumbers. Scattered light, after being diffracted from a high groove density grating, is detected by a charge-coupled device (CCD) detector and recorded as photon counts with respect to relative wavenumber. Just as in infrared absorption spectroscopy, Raman spectra give vibrational information indicative of the molecular bonding of the analyte, exhibiting vibrational frequencies similar to those frequencies in the mid-

infrared region of the electromagnetic spectrum absorbed during Fourier transform infrared (FT-IR) spectroscopy. Because of this ability to provide bonding information unique to a particular molecular species, Raman spectroscopy is well-suited for forensic analysis.

1.2.2 Applications in forensics

Raman spectroscopy has become an attractive option in forensics because of its non-destructive nature.[7] It is very common in casework to come across samples with only trace amounts of target analytes, so it is of great interest to gain as much discriminatory information from a sample as possible without altering it chemically. Additionally, virtually no sample preparation is required for Raman analysis. This advantage of Raman spectroscopy makes it especially well-suited for forensics, as the sample can be left in a pristine condition during analysis. Further, as a vibrational spectroscopy technique, Raman spectroscopy provides a unique spectrum for different substances, meaning it is well-suited as a confirmatory test that is not restricted to any specific sample, unlike currently-utilized confirmatory tests.

Lednev et al. have demonstrated that Raman spectra of semen and other bodily fluids are obtainable.[7] Since bodily fluids are comprised of a large number of solutes, the Lednev group rastered a semen stain deposited on glass and averaged all of the spectra together to yield an overall Raman spectrum for the fluid. This was repeated to obtain a spectrum for blood, sweat, and other bodily fluids. Using a variety of chemometric techniques including partial least squares-discriminant analysis, principal component analysis, and others, several major contributors to the overall Raman signature of semen were identified. While each method gave a different list of solutes contributing to the Raman spectrum for semen, there were six solutes that were identified repeatedly: urea, phenylalanine, choline, lactic acid, tyrosine, and spermine.[5,7-9]

Recently, the Lednev group determined that the Raman spectrum of seminal fluid (which does not contain sperm cells) and semen (which is comprised of both seminal fluid and sperm cells) are largely identical, meaning Raman spectroscopy could function as a confirmatory test for semen regardless of the sperm cell count in the sample.[9]

While recent work in using Raman spectroscopy for bodily fluid analysis seems promising, Raman spectroscopy is hindered by the low probability of Raman-scattered photons. It is estimated that for every 10^6 photons that are Rayleigh-scattered from a surface, only one will scatter inelastically.[6] The low probability of these scattering events often results in low-quality spectra, especially for low-concentration analytes, as is often the case in forensic casework. In order to circumvent this issue, this project employs surface enhanced Raman spectroscopy (SERS), a technique used to enhance Raman signal.

1.3 Surface-enhanced Raman spectroscopy (SERS)

1.3.1 Fundamentals

Surface-enhanced Raman spectroscopy (SERS) is a modification of Raman spectroscopy in which the sample under investigation is in close or intimate contact with a metallic nanostructured surface. By doing so, the intensity of Raman-scattered light can increase dramatically. This occurs due to the establishment of plasmons, or collective oscillations of electrons in the metal nanoparticle, induced by the electric field of the incident light.[10] These plasmons will oscillate at a frequency equal to that of the incident laser light, called the plasmon frequency. Plasmons are believed to lead to signal enhancement through some combination of two mechanisms, both of which are based on the principle that Raman signal intensity is directly proportional to the polarizability of a vibration.[11] One of these mechanisms is chemical; a bond

that forms between a molecule and the metallic nanostructure allows electron density to flow from the nanostructure directly to the molecule. The other mechanism is electromagnetic; since a plasmon is an oscillation of point charges, an electric field is established, which oscillates and couples with the electric field of the molecule. These processes lead to a considerably higher signal when the scattered light is collected by the detector of a Raman spectrometer, and consequently a higher-quality spectrum results.

All metals are capable of establishing plasmons because they are comprised of delocalized conduction-band electrons. The coinage metals gold, silver, and copper are typically chosen as SERS substrates because they are the only metallic nanoparticles that have plasmon resonance frequencies, or frequencies at which the electron oscillations become self-sustained, in the visible range.[12] Silver is of particular interest because it has the greatest capability to promote electrons to the conduction band, and thus attribute them to the plasmon.[13] Further, the size of a nanoparticle affects its plasmon resonance frequency; silver is the only known material that can have its plasmon resonance adjusted to anywhere in the visible range by altering the size to which the nanoparticles are grown.[12,13]

Metal nanoparticles are known to have a larger scattering cross section than geometric cross-section, meaning more light is scattered from it than is physically incident on it. This is captured by its complex dielectric function, given as

$$\varepsilon(\omega) = \varepsilon_1(\omega)+\varepsilon_2(\omega) \quad [1]$$

where ω is frequency and $\varepsilon_i(\omega)$ is the dielectric function, where indices i=1 and i=2 represent the real and imaginary components, respectively.[13] The real component of the dielectric function corresponds to scattering light, and the imaginary component corresponds to attenuation of

incident light by absorption (cf. Figure 3). Of all the metals with a visible spectrum plasmon resonance, the real-to-imaginary ratio is largest for silver nanoparticles, meaning that silver is the most efficient at transferring energy to the analyte molecule to induce the SERS phenomenon.

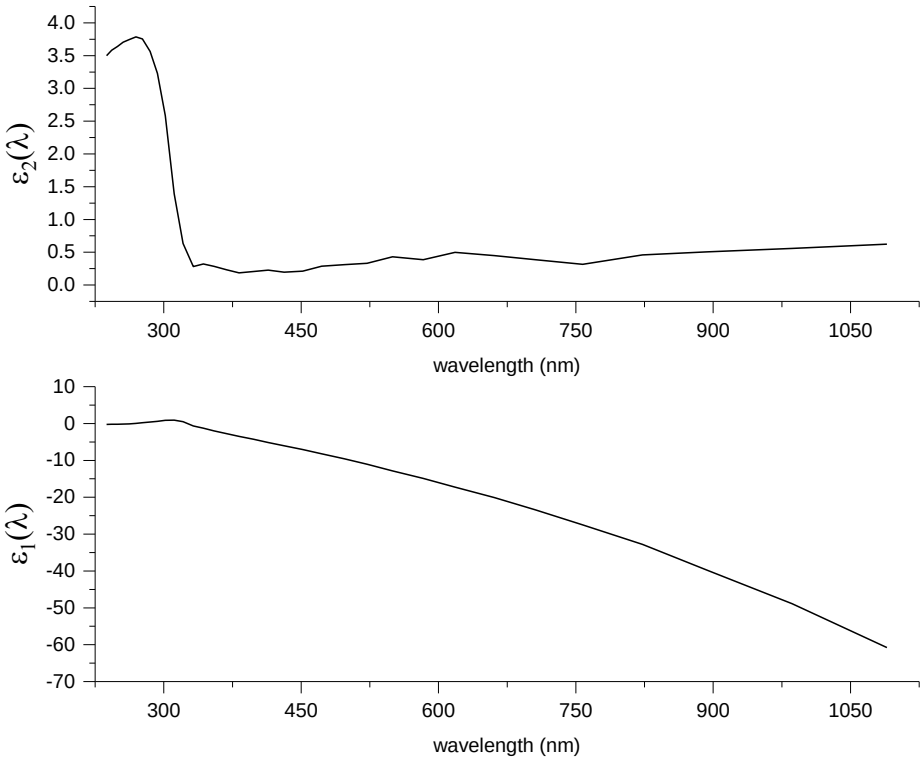

Figure 3: Dielectric function dependence on wavelength for silver.[13]

Further, if metallic nanoparticles are placed in close proximity to each other, the local electromagnetic fields of their respective plasmons can overlap, leading to longer-lasting,

coupled-plasmon resonances and a more intense electromagnetic field between the nanostructures.[12] These extended electric fields further polarize any molecules located in this overlap, leading to an even greater signal enhancement. Raman signal magnification of up to 10^{14}, enough to enable single molecule detection, has been reported.[14,15] These areas of intense signal enhancements are called "hot spots."[11] Figure 4 shows the establishment of a hot spot between two silver nanoparticles.

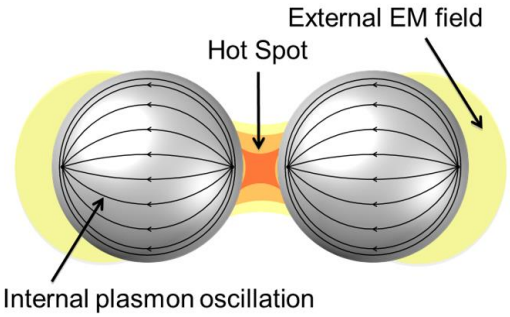

Figure 3: Surface enhancement and hot spot arising from plasmon oscillations in adjacent silver nanoparticles.

1.3.2 Silver-coated swabs

Given the capability of metal nanoparticles to significantly intensify scattered light, it has been proposed for forensic analysis, especially since signal intensity can compensate for the lack of analyte in evidence. To this end, Evanoff et al. developed a method for growing silver nanoparticles (AgNPs) directly onto the fibers of commercially-available nylon swabs, as shown

in Figure 5 below.[16,17] Rather than simply collecting samples in the field and depositing them onto a silver substrate in the lab, this method allows a crime scene investigator to greatly simplify sample preparation as an extra step by incorporating it into sample collection.

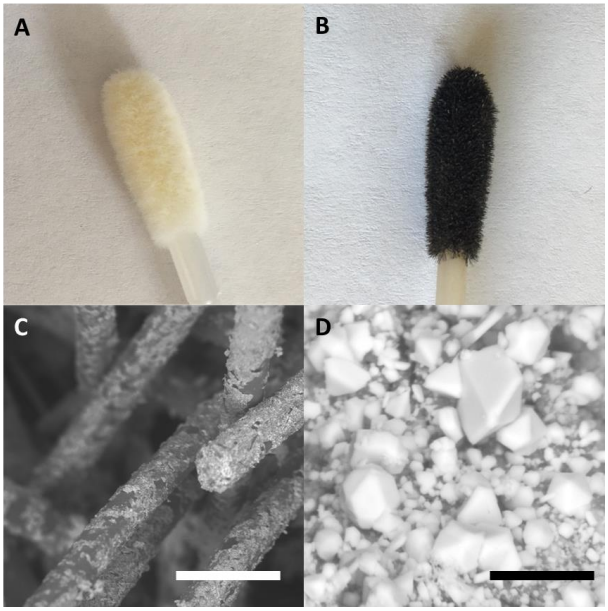

Figure 4: AgNP-coated nylon swab a) before coating, b) after coating, c) SEM image of coated fibers (scale bar = 500 μm), d) magnified view of AgNPs on a single fiber (scale bar = 5 μm).

1.3.3 Percolation threshold

To maximize the surface enhancement from a substrate coated with AgNPs, the nanoparticles should be grown to the extent that the largest possible amount of hot spots are established. It is of interest, then, to know how these growth times/thicknesses relate to the

percolation threshold of silver on nylon. The percolation threshold is the metal growth thickness at which separate metallic islands coalesce into a continuous network.[18] Since the substrate is typically an insulative material, the percolation threshold is the point at which the surface becomes conductive, which is a result of the continuous network of deposited metal.[19] Figure 6 below compares the difference between non-percolated and percolated layers of silver on nylon.

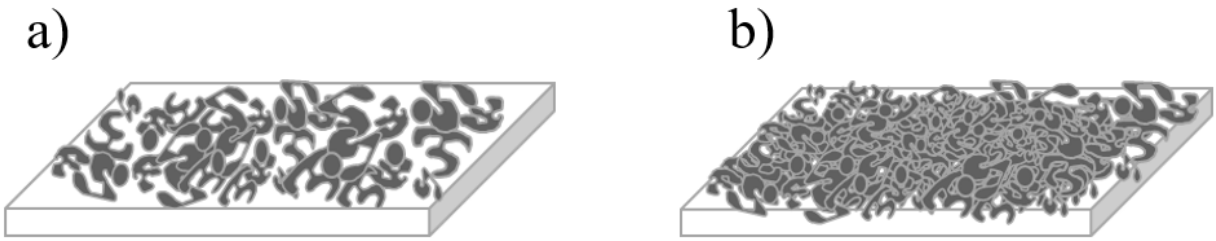

Figure 5: Schematic representation of silver grown on nylon a) before and b) after percolation.

Brouers et al. have modelled Raman scattering enhancement with respect to both incident wavelength and metal concentration for metallic films on dielectric substrates.[20] This work reports maxima in enhancement both above and below the percolation threshold and wavelengths from the visible to the far-infrared regions. This concept was further explored by Gadenne et al., who determined that enhancement was maximized just below the percolation threshold and increases again just after the threshold.[21]

According to Enders et al., the reason for Raman enhancement just below the percolation threshold is because, at that point, the distance between the growing metallic islands has decreased to the size necessary to establish hot spots.[22] This would also explain why enhancement seems to decrease after this point, agreeing with Brouers and Gadenne, given that further growth of the islands would shrink these gaps below the separation needed to form a hot spot.[20,21] After the percolation threshold is passed, the silver surface is still roughened; the existence of "nanoholes" in the silver network can give rise to hot spots and increase surface enhancement. Because of this, hot spot enhancement may occur above and below the percolation threshold for silver on nylon. Therefore, it is of interest to be able to grow silver layers on nylon either above or below this percolation threshold.

1.4 Complex stain analysis

While preliminary results with the AgNP-coated swabs are promising, there are a few obstacles that need to be addressed before employing them for confirmatory testing in a forensics setting. The current method of growing silver on the fibers does so at random,[16] so currently there is no way to control the distribution of nanoparticles on nylon. It follows that the distribution of gaps between the particles of appropriate size to enable hot spot enhancement also cannot be controlled.

The AgNP-coated nylon swabs have been used for identification of solids and simple liquids, including dye solution of ruthenium (bipyridine) and crystal violet.[16] Analysis becomes much more complicated when the sample is a complex mixture like bodily fluids. Complex mixtures tend to form heterogeneous stains, meaning that the components of homogeneous solutions/suspensions interact differently with the substrate and solvent front during the drying

process, leading to non-uniform deposition of the mixture across the substrate surface.[5] This complicates spectroscopy of these stains since any two point measurements taken along the stain are often different from each other, and neither will be representative of the fluid as a whole, as shown in Figure 7, which was made using the raw data from Reference 16 and shows four separate spectra taken from semen on the same SERS-active swab.

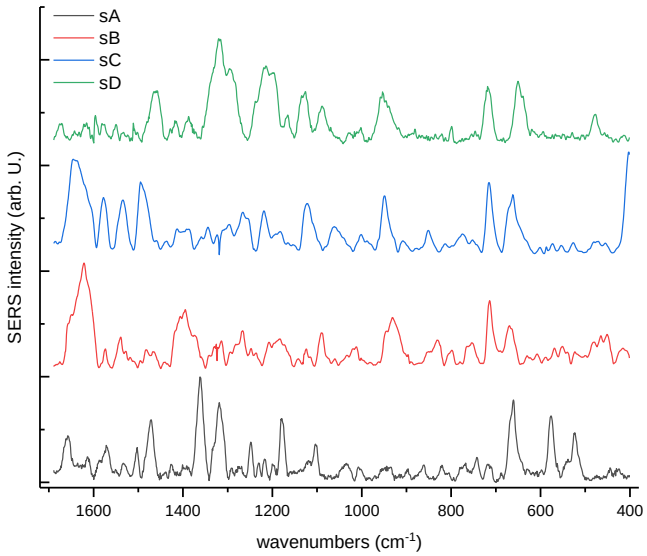

Figure 6: Spectra taken at four different locations (A-D) along a semen stain collected on a AgNP-coated swab.[16]

As mentioned above, Lednev et al. presented an overall spectrum for semen by averaging several point scans along a stain on glass in order to bypass the heterogeneity problem.[5]

Although they acknowledged the separation of solutes in a dried stain, they did not analyze any predictable distribution for these solutes. Therefore, in order to use these swabs for body fluid analysis, especially seminal fluid, there is a need for an understanding of how these complex mixtures dry on various substrates, including, as is pertinent to this research, silver-coated nylon.

1.4.1 Coffee ring effect

The basis for modeling the stains formed by semen on AgNP-coated surfaces is the so-called coffee-ring effect. When a droplet dries on a surface, it can form a stain where the solute particles aggregate on the periphery of the stain; the resulting ring of solutes is called a "coffee ring" as it resembles the ring of dried coffee that forms at the contact point of a surface and cup.[23] This pattern forms because the droplet evaporates from the outside in, and capillary flow from the center of the droplet push outwards to replenish the edge of the droplet as it dries. Capillary flow is the flux of solvent toward the pinned contact line that results from the difference between the amount of solvent removed from evaporation and the amount of solvent needed to be removed to maintain the hemispherical cap shape of the droplet, which is a result of surface tension.[24] Solute particles are carried along to the edge by capillary flow; by the time the droplet becomes a stain, most of the solute particles are deposited at the edges of the stain, forming the distinct ring pattern.[23,24] Figure 8 shows the step-by-step process for stain formation on a solid surface. The process and result for an aqueous droplet depend on the hydrophilicity of the solid surface.[23,25] When the droplet is first deposited on the surface, the edge of the droplet, called the contact line, spreads out; the more hydrophilic the surface, the further the contact line spreads.[26] Eventually, the contact line pins, or no longer spreads. On a hydrophilic surface, as shown in Figure 8a-8d2, the height of the droplet begins to decrease while the contact line remains pinned; this phase of the drying process is called the constant radius regime (CRR).

Since the CRR keeps the edge of the droplet locked for an extended period of time, most of the solute particles are transported to the periphery by capillary flow. After some time, the CRR gives way to the next phase, the constant contact angle regime (CCAR), in which the angle the droplet makes with the surface, or contact angle, is held constant and the contact line starts to retract. The CCAR continues until the solvent has completely evaporated and the droplet has become a stain. Silver and glass have been observed to be hydrophilic with respect to water droplets in the literature, with glass more hydrophilic than silver, so the above droplet drying process applies to both of these substrates.[27] On a hydrophobic surface, the CCAR and CCR are reversed (see Figure 8e-8h2). The hydrophobicity of the surface causes the contact line to slip more readily,[25] since the contact line spends less time at any one location, there is less time for solute particles to get deposited at the contact line. The end result is a distribution of solute particles along the stain. Both result in an aggregation of particles at the stain periphery, but nearly all of the particles do so on a hydrophilic surface and only some do so on a hydrophobic surface.

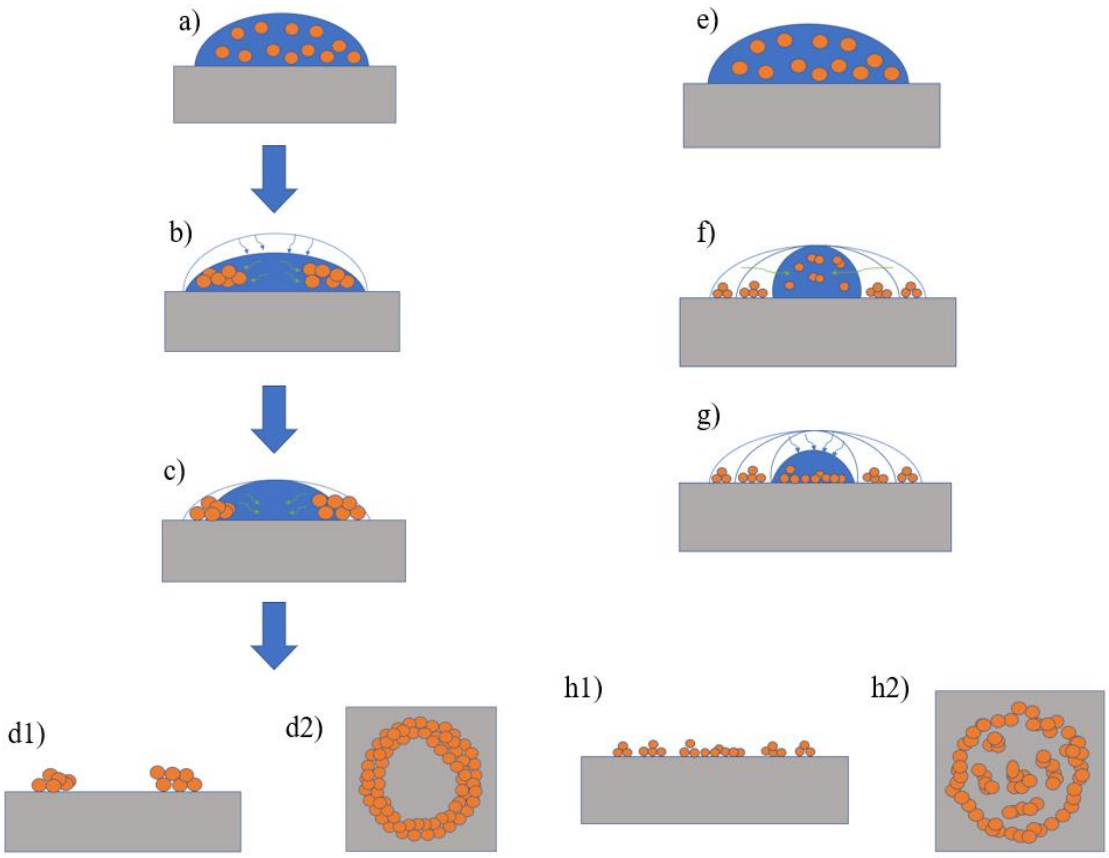

Figure 7: Stain formation from a drying sessile droplet on a hydrophilic surface (a-d) and on a hydrophobic surface (e-h). a, e) droplet is deposited on a surface, b) height decreases via evaporation (blue arrows) and solute particles are pushed outwards by capillary flow (green) during CRR phase, c) contact angle decreases as capillary flow (green) push inwards during CCAR phase, d1) side view of coffee ring stain resulting after solvent dries completely, d2) top-down view of coffee ring stain. A stain on a hydrophobic surface e) instead dries first through f) the CCAR phase, then g) transitions to the CRR phase, leaving a sporadic stain shown in h1 and h2.

Kumar et al. have previously compiled several factors involved in droplet spreading on solid surfaces.[28] For example, if a substrate is demonstrably hydrophilic, than increasing the roughness of the surface will increase the wettability, or propensity of a droplet to spread on the surface. Liquid properties such as viscosity, surface tension, and density also alter the spreading

of a droplet on solids, with an increase in any three parameters resulting in a decrease in wettability. Further, polar surfaces are generally more wettable with respect to aqueous droplets.[29]

1.4.2 Stains of heterogeneous mixtures

Promising results by Wong et al. show that the coffee ring effect leads to self-segregation of solutes in a ternary mixture.[30] In this study, a mixture of polystyrene spheres of three different sizes was deposited on a glass slide. After drying, it was observed that the stain formed three concentric coffee rings. The outermost coffee ring contained the smallest spheres, the middle ring contained the spheres of intermediate size, and the innermost ring contained the largest spheres. It was reasoned that this pattern occurred because the capillary flow in the droplet pushed the smaller particles further to the contact line of a droplet during its CRR phase. The same trend of coffee ring diameter varying inversely with solute mass was observed with a mixture of antimouse IgG antibodies, E. coli, and B-lymphoma cells,[30] indicating this model may work for both particles and smaller molecules.

The Wong et al. study showed self-segregation of solutes from a mixture while drying, but these "solutes," suspended particles, were massive compared to many of the molecular structures found in a bodily fluid like semen. Self-segregation within a bodily fluid has been investigated by Filik and Stone in their analysis of tear fluid, demonstrating that the sort of separation seen by Wong et al. could be observable in bodily fluid stains.[31] Bodily fluids contain a vast amount of solutes, so a pristine set of concentric rings for every single solute is not expected. However, as found in this study on tear fluid, there appears to be a separation in Raman-active solutes based on solubility, with less water-soluble solutes appearing at the

periphery of a stain and more hydrophilic solutes depositing closer to the interior of the stain. In this study, protein, urea, and bicarbonate were found to be the major Raman-active components in tear fluids, as identified by principal component analysis. By depositing tear drops on CaF_2 slides, they determined the proteins aggregated on the edge of the droplet, while bicarbonate and urea deposited more interior to the stain, with bicarbonate located slightly more interior than urea. The fact that three Raman-contributing solutes were able to self-segregate in the same fashion as in the Wong study suggests the findings from the latter study are indeed applicable to bodily fluids, and the trends seen in both studies may apply to semen. Further, the Vroman effect, in which proteins of smaller molecular weight are displaced by those of higher molecular weight, has been observed in bodily fluids,[32] indicating the overall stain morphology may be a combination of both relative solute mass, as best illustrated by the Wong et al. study,[30] and relative water solubility, as best shown by the Filik et al. study.[31]

CHAPTER 2: INTRODUCTION TO RESEARCH

The primary goal of this project was to determine if the major contributors to the overall Raman signature of semen self-segregate on AgNP-coated substrates in any reproducible fashion. Simple mixtures of solutes that contribute the most to the overall Raman signature of semen, as identified by Lednev et al.,[5] were created with ultrapure water as the solvent. Based on the studies by Wong[30] and Filik,[31] these solutes may segregate into concentric coffee rings with diameters varying inversely with water solubility. More specifically by making a seminal fluid simulant by mixing urea, phenylalanine, and choline chloride together in ultrapure water, it was hypothesized that these solutes would self-segregate concentrically during stain formation. In this way, phenylalanine should migrate to the periphery of the stain, choline chloride should be concentrated in the center, and urea should be found in-between the two, on the basis of their relative water solubilities.

Since the hydrophobicity of a surface impacts how well coffee rings form,[23] it stands to reason that concentric ring definition may be a function of surface hydrophilicity. Since the surfaces in this study are AgNPs, it is useful to have an understanding of their relative hydrophobicity with respect to other substrates like bare nylon and glass. Therefore, this study aimed to quantify the hydrophobicity of AgNP-coated nylon.

This project also aimed to determine the percolation threshold of silver on nylon using two different growth methods, since these thresholds were not reported in the literature. Silver nanoparticles were grown using thermal deposition and chemical growth. The thermally-deposited layers were made at varying deposition rate and layer thicknesses to observe which

combinations gave non-percolated silver sheets and which gave percolated sheets. The determined thresholds were then used to study their relationship to surface enhancement to see, for example, if higher-quality spectra resulted from substrates just below and/or just above the percolation threshold.

CHAPTER 3: EXPERIMENTAL

3.1 Materials

Nylon sheets were purchased from Alfa Aesar at 1.6 mm thickness, and cut into squares roughly 2.5 cm long on all sides. Urea (98%, extra pure, pearls), L-phenylalanine (98.5%), and choline chloride (99%, nitrogen flushed) were all purchased from Acros Organics. Silver pellets (99.99%, ¼" diameter x ¼" long) used for thermal deposition were obtained from Kurt J. Lesker Company. For chemical growth of silver layers on nylon, silver (I) oxide (99.99%) was purchased from Alfa Aesar, and hydrogen (ultra-carrier grade) and argon (high-purity grade) gas were purchased from Airgas. Pooled human semen was obtained from Lee Biosolutions.

3.2 Instrumentation

All spectra presented herein were acquired using a Horiba Labram HR Raman microscope with an 1800 groove/mm grating, 800 mm monochromator, and Horiba Synapse CCD detector, in conjunction with a LabSpec 6 software package. The objective used was a planar-achromatic infinity-corrected 100x long working distance objective with a numerical aperture of 0.60 (f-number 26.5). The microscope was calibrated with NIST silicon and aspirin standards.

Thermally-grown layers of silver on nylon were prepared using a Denton Vacuum DV-502A Thermal Evaporator. A Signatone 4-point probe head coupled to a Kiethley 2400-series source meter was used to measure resistance at various points along each silver sheet. The tilting process was filmed using a Canon EOS Rebel T5i camera (SN: 242032001778) with a Canon EF

100 mm focal length f/2.8L Macro Lens with an ultrasonic motor and image stabilizer (SN: 7810002746).

3.3 Silver layer synthesis

3.3.1 Thermally-grown layers

Nylon squares of roughly 2.5 cm x 2.5 cm were cut with shears to fit into a 2x3 sample holder and placed in the thermal evaporator. A schematic for the evaporator is shown below in Figure 9. The evaporator contained an enclosure within which the pressure was reduced to less than 100 μTorr. The top of the enclosure featured a sample holder for six nylon pieces per run. A coiled filament sat at the bottom of the enclosure and would hold a silver pellet. At sufficiently low pressures, a current running though the coil would dissipate enough heat into the pellet to melt and then vaporize the silver. The silver vapor deposited onto the surface of the nylon substrates and on the inside walls of the enclosure since their temperatures were much lower. A quartz crystal balance within the enclosure was used to determine the rate of silver deposition and silver layer thickness. These silver layers were stored in jars flushed with argon gas.

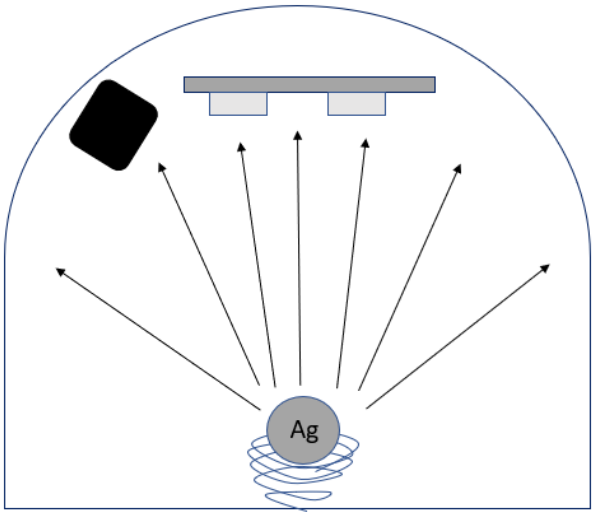

Figure 9: Schematic for the thermal evaporator. A bell jar encloses a silver pellet sitting on a metal coil. At low pressures, heat from the current in the coil sublimates the silver (vapor shown with arrows), which lands on the nylon squares in the sample holder (shown in light and dark grey, respectively). In black is the quartz crystal balance used to measure deposition rate and thickness.

3.3.2 Chemically-grown layers

To chemically prepare the layers of silver, nylon squares of roughly 2.5 cm x 2.5 cm were cut with shears rinsed with acetone and sonicated in ultrapure water for 15 minutes for pre-treatment/cleaning. The squares were then soaked in a bath of saturated silver (I) oxide solution overnight to allow adhesion of ionic silver and molecular silver oxide species. A quartz three-necked round-bottom flask was used as the reaction vessel; 0.25 g of silver (I) oxide powder was administered to 300 mL of ultrapure water in this flask. Three squares of nylon were added to the vessel, which was transferred to a heating mantle. The contents were heated to 70 °C and stirred at 125 rpm. After the temperature stabilized, the contents were stirred up to 700 rpm and

hydrogen gas was pressurized above the solution at 7.5 psi. This initiated the following redox reaction:

$$Ag_2O_{(aq)} + H_{2(g)} \rightarrow 2Ag_{(s)} + H_2O_{(l)} \quad \textbf{[1]}$$

Different batches were prepared in which the time of exposure of the reaction mixture to hydrogen was varied. Four-point probe measurements were used to determine the relationship between growth and percolation threshold for silver on nylon. These silver layers were placed in bottles of ultrapure water for storage.

3.4 Four-point probe measurements

As stated previously, a silver layer has achieved percolation when a continuous network of the silver has formed on the surface of the substrate. Before this threshold is reached, the silver nuclei will not coalesce on the nylon substrate and the surface will be insulative. Conversely, a conductive surface indicates the percolation threshold has been reached, since electrons can pass through an uninterrupted network of silver. Therefore, the percolation threshold can be determined through conductivity measurements on the surface.

Takele et al. have shown that resistivity of a metallic layer varies sigmoidally as a function of the concentration of metallic nanoparticles increases on a surface, where the lower and upper regions of the curve correspond to the conductivities of the substrate and metal, respectively.[33] That is, the resistivity of the layer does not vary gradually while the metal grows but rather suddenly at the point where the nuclei coalesce. Thus, the percolation threshold occurs at the particle concentration coincident with the inflection point of the sigmoid. To our knowledge, the literature does not currently include a report of the percolation threshold for the specific combination of silver on nylon. Although the instrumentation currently available at the

time of this study was not capable of giving sheet thickness, and thus resistivity values, the conductivities of the grown silver layers were measured instead. This was done using a Signatone four-point probe head with a Keithley 2400-series source meter.

A schematic for the probe is shown below in Figure 10. When the leads come into contact with a surface, a current is sent through the outside leads (shown as Leads 1 and 4). The middle two leads (2 and 3) measure the voltage drop between them as the current passes through the outside leads. The four point probe was interfaced with LabView to display a voltage (*V*) vs current (*I*) plot at each point of contact. Thermally-grown layers were made six at a time with silver on one side, so four points on each of the six sheets were sampled using the four-point probe to yield 24 data points per batch. Chemically-grown layers were made three at a time with silver on both sides, so four points were sampled on each side of each sheet, also yielding 24 data points per sample batch. The slopes from each of these 24 curves were averaged to provide an average conductance value for each silver layer.

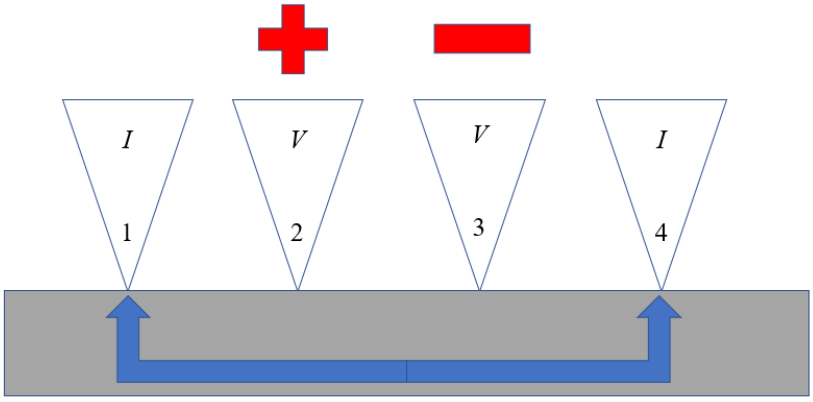

Figure 10: Schematic for the four-point probe. Current (*I*) flows between the outer leads (1 and 4) and voltage (*V*) is measured between the middle leads (2 and 3) on each silver layer (shown in grey).

3.5 Contact angle hysteresis measurements

When a droplet of water is deposited on a surface, its contact angle, or the angle the droplet forms with the surface, indicates the wettability of the surface; the larger the angle, the greater the hydrophobicity.[34] There are various ways to measure contact angles on a surface. These methods can generally be categorized as static or dynamic, where the droplet stays stationary in the former case and is moving in the latter. A dynamic contact angle measurement is considered more revealing of the roughness of the surface.[35] One way to perform a dynamic contact angle measurement is by calculating the contact angle hysteresis (CAH) of the droplet. When a droplet moves on the surface, it has an advancing front in the direction of droplet motion, and a receding front on the opposite side. The contact angles on these fronts are the advancing and receding angles, respectively. CAH is the difference between these two angle values. Figure 11 provides schematics comparing static contact angle and contact angle

hysteresis. Low hysteresis values are indicative of a smooth surface, and high hysteresis values correlate to very rough surfaces.[36]

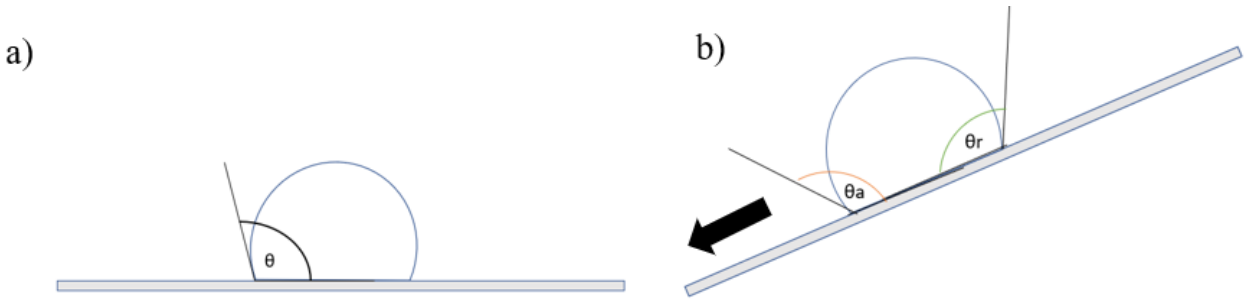

Figure 11: Schematics of a) static contact angle of a sessile droplet on a flat surface, and b) advancing (θ_a) and receding (θ_r) angles of a droplet, with a black arrow indicating the direction of motion of the droplet.

To quantify the wettability of the silver films, CAH measurements were performed on a rotating stage shown in Figure 12 below. The tilting method was employed in this study[37] wherein a sample was placed upon the rotating stage and tilted until a sessile water droplet on the surface of the sample began to slide. Tilting was filmed and footage of the tilting process was edited using Blender to procure film stills immediately before droplet tilting. At this moment in the tilting process, there is no external force acting on the droplet; that is, the friction the droplet experiences is exactly equal to the antiparallel component of the weight of the droplet (see Figure 12b). By measuring the advancing and receding angles at this moment, these angle measurements will not be influenced by any external forces. The Contact Angle plugin in ImageJ

software was used to trace out the sessile droplet and estimate the receding and advancing angles, from which CAH values were calculated.

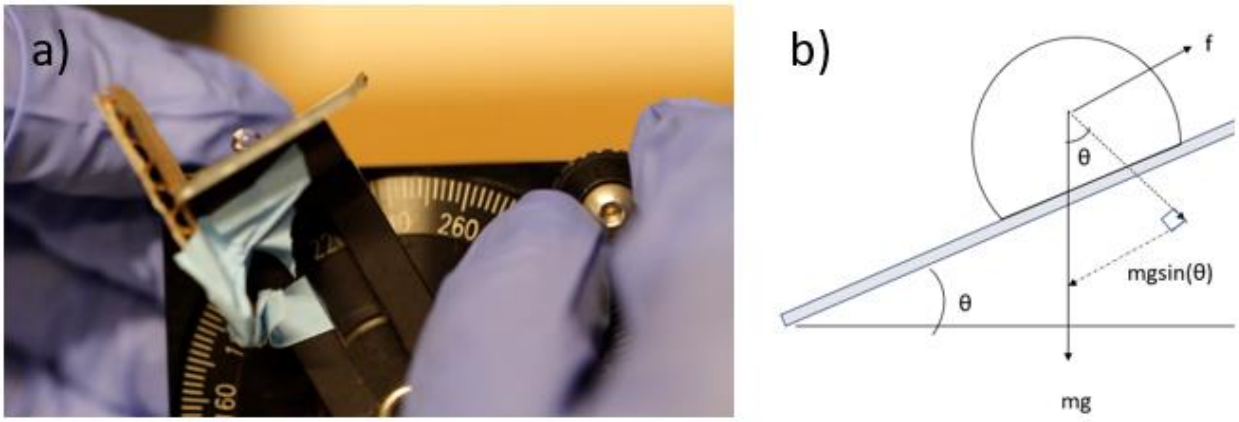

Figure 82: Tilting study performed with sessile water droplets on each substrate. a) setup used for tilting study, b) free-body diagram of the sessile droplet just before sliding along the substrate.

3.6 Semen simulant formation

A semen simulant was prepared to contain some of the major Raman-contributing solutes of semen dissolved in ultrapure water. Previous studies on the formation of semen simulants as well as various quantization studies were used to determine concentrations for the solutes. The respective concentrations for urea,[38] phenylalanine,[39] and choline[40] are included in Table 1. Preliminary results showed the low concentrations of urea and phenylalanine were difficult to capture in the Raman spectra of stains formed from 20 μL droplets of simulant solution. As a

result, the concentrations of both of these solutes were doubled for use in simulants; this change is reflected in Table 1. A 100 mL volumetric flask was used to prepare 100 mL solutions of urea, phenylalanine, and choline chloride, and the solutions were deposited onto five substrates: bare nylon, thermally-grown silver on nylon (both non-percolated and percolated), and chemically-grown silver on nylon (both non-percolated and percolated). Table 1 also shows vibrational modes for urea,[41] phenylalanine,[42] and choline[43] that will be used later for detecting these solutes in mixtures.

Table 1: Concentration of each solute used for preparing the semen simulant, compared to their physiological concentrations, along with Raman modes of interest.

	Physiological concentration (mg/dL)	***Concentration in simulant (mg/dL)***	***Raman band(s) of interest (cm^{-1})***	***Associated vibrations***
Urea	45	90	1012	NCN symmetric stretching
Phenylalanine	28	56	1001	ν_{12} in-plane symmetric stretch
Choline chloride	79.04	79.04	a) 713 b) 1012	a) quaternary ammonium symmetric stretch b) CH_2 rocking

3.7 Raman spectra acquisition

A droplet each of semen simulant solution and pooled semen were deposited onto nylon and silver as 20 μL droplets and allowed to dry overnight inside of a closed petri dish which sat on an air table and was covered in aluminum foil, allowing for droplets to spread more uniformly

across each substrate while drying. Fully-dried droplets are henceforth referred to as stains. Stains of semen did not afford sufficient Raman signal on their own regardless of substrate; for this reason, one 20 μL droplet of silver nanoparticle suspension was added to each semen stain to increase the intensity of their Raman spectra. The suspension used featured a particle concentration in the vicinity of 10^{12} mL^{-1}. After this addition of AgNPs to the stains, Raman spectra were obtainable.

For all stains unless otherwise specified, a 1-dimensional line scan with a step size of 400 μm was taken across the diameter of the stain using a 632.8 nm helium-neon laser. Laser power was 100% (7.49 mW) for scans on bare nylon and 10% (0.721 mW) for scans on AgNP-coated substrates. The laser power was reduced for scans performed on silver layers in order to avoid saturating the detector. Each spectrum was acquired for 3 seconds with 20 accumulations. All spectra presented herein were baseline corrected in the LabSpec 6 software suite. These corrections were all done using a ninth order polynomial with up to 256 points, with 4 noise points. A single line scan across the diameter was conducted since, if the solubility-based concentric coffee ring hypothesis were correct, the line scan should intersect with each coffee ring twice, so each solute and its respective migration pattern in the stain should be elucidated by this scan.

The Appendix features individual spectra collected along every line scan. For each sample, the spectra were further processed as follows in Microsoft Excel: any baseline tilt from the LabSpec baseline function was corrected by calculating a best fit line and subtracting, then the baseline was recalculated by ensuring that the minimum spectral intensity was set to zero, followed by normalization of the spectra on a scale of 0 to 1 by dividing all intensity values within a spectrum by the spectral maximum. Solutions of urea, phenylalanine, and choline

chloride were prepared on a SERS sandwich substrate made using the procedure outlined by Daniels and Chumanov;[11] the SERS spectra of these solutes and that of the SERS sandwich substrate were combined to compare to the individual simulant and semen spectra. This was done by giving a weight to each of the four spectra, to result in an overall "component fit" spectrum to plot against the spectra of the samples. The sum of the square of residuals between the two spectra was calculated. The Solver plugin in Excel was then used to calculate the distribution of weights for the component spectra such that the sum of the square of residuals was minimized, giving the closest fit between the "component fit" spectrum and the measured spectrum. These new weights were then used to calculate the contribution of each solute to each data spectrum. These contributions are reported below as peak areas of each component as a function of position along the line scan, with the origin being the center of the stain.

CHAPTER 4: RESULTS AND DISCUSSION

4.1 Percolation threshold of silver on nylon

Conductivity was calculated from the slopes of IV curves collected from silver layers grown either chemically or thermally on nylon in order to determine their respective percolation thresholds. In lieu of concentration or particle packing factor, the independent variables for these threshold plots were growth time for chemically-grown layers and both deposition rate and layer thickness, as estimated by using the aforementioned quartz crystal balance, for thermally-grown layers, since these variables could be directly controlled. Also, since film thickness measurements were not possible with the instrumentation available, conductance could not be converted to conductivity, which is typically how these results are reported in the literature,[44] so these results were left in terms of conductance. Since no percolation threshold for silver on nylon has been reported in the literature, these findings could be confirmed with future studies using surface thickness measurements and SEM images to report the data in conventional resistivity vs. packing factor figures. The findings herein serve as a preliminary exploration of these values.

4.1.1 Thermally-grown silver

Using the 4-point probe, current versus voltage curves were obtained by sampling four points along each surface of thermally-grown silver on nylon. Each silver layer was prepared at a unique combination of silver deposition rate and layer thickness. For each batch of samples with a given growth rate and layer thickness, the average conductance among all six samples in the batch is presented and plotted in Figure 13 below. These same averages, along with the standard deviation between these samples and their coefficient of variation, is included in the Appendix.

Thermally-grown silver layers were grown to one of four thicknesses: 10 nm, 15 nm, 20 nm, and 30 nm. The silver surfaces demonstrate a conductance greater than 1 mS at the larger layer thicknesses of 20 nm and 30 nm layers. This suggests that during the thermal deposition process, percolation of isolated silver clusters on nylon was obtained by the time 20 nm of silver had grown. Silver layers are largely non-percolated at 10 nm, with conductance values on the order of 10^{-10} S. Most of the silver layers grown at 15 nm have an intermediate conductance between 10^{-3} and 10^{-4} S. It should be noted that the coefficient of variation is consistently greater for these layers showing intermediate conductance values. This suggests that at a thickness of 15 nm, silver islands have begun percolating on nylon, but this coverage is limited. Based on the data obtained, it appears the percolation threshold of silver thermally grown on nylon is around 15 nm. Further, there does not seem to be any trend in deposition rate on percolation; the percolation threshold may well be only a function of layer thickness.

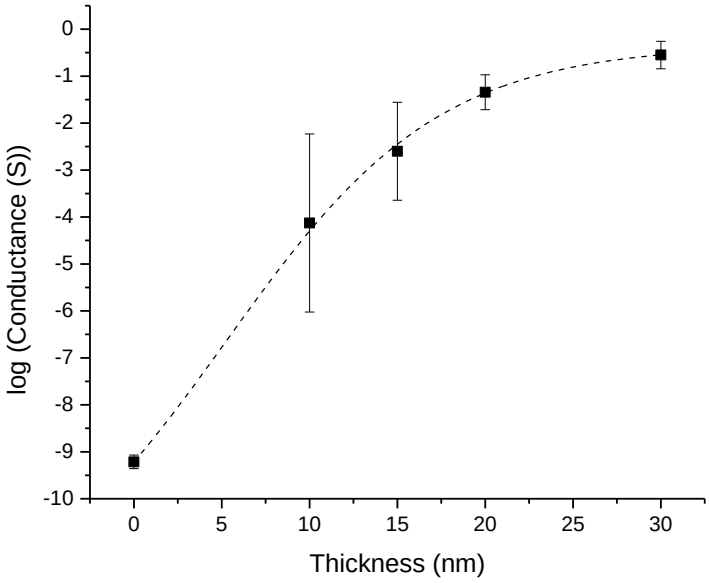

Figure 93: Plot of conductance vs layer thickness for thermally-grown silver layers on nylon. The sigmoidal best fit line ($R^2 = 0.999$) was calculated using the Dose-Response function in OriginPro.

Figure 13 shows average conductivity for all layers as a function of layer thickness. According to the literature, the data should form a sigmoid, with the percolation threshold located at the inflection point of the curve.[33] The conductance at a silver thickness of zero nanometers was measured for a sheet of bare nylon. Since only one data point on this plot represents a nonzero thickness of silver on nylon, these results should be followed up by thermally growing more silver layers at thicknesses below 10 nm to see if this is the conductivity associated with truly non-percolated silver on nylon. Thus this data provides preliminary support of the percolation threshold of silver on nylon at a layer thickness of 15 nm.

4.1.2 Chemically-grown silver

As in the previous section, four-point probe measurements were carried out on chemically-grown samples, where the silver layer was the product of a reduction of silver (I) oxide by hydrogen gas. The average, standard deviation, and coefficient of variation of conductance for each sample is presented in the Appendix. The averages were plotted as a function of reaction time in Figure 14, where the conductance at a reaction time for zero minutes was measured directly on bare nylon. A rapid increase in conductance occurs around 61 minutes, where conductivity jumps from nanoSiemens to milliSiemens. Above and below this threshold, as expected, conductivity values vary only slightly. Between 62-66 minutes, conductivity does vary significantly, as reflected in coefficients of variation for these growth times (see Appendix section A.5). Therefore, the percolation threshold may actually have occurred over the time span of 61-68 minutes. The lower end of the sigmoid was only one order of magnitude greater than the conductance for bare nylon.

The variation of conductivity within this time span of 61-68 minutes, as with the thermally-grown samples, is attributed to sparse coalescence of some silver islands across the surface while significant portions of the substrate remained uncoated. As a result, there may have been sites where the four-point probe measured a mixture of percolated and non-percolated silver, giving high coefficients of variation and conductivity values slightly lower than those seen beyond 68 minutes. The coefficient of variation for 90 minutes was higher than expected; since this growth time is well above the percolation threshold and is surrounded by growth times with smaller coefficients of variation, this may have come about from some error in measurement (e.g. inconsistent contact between the leads of the four-point probe and the silver surface, or insufficient drying time of the silver sample preceding measurement).

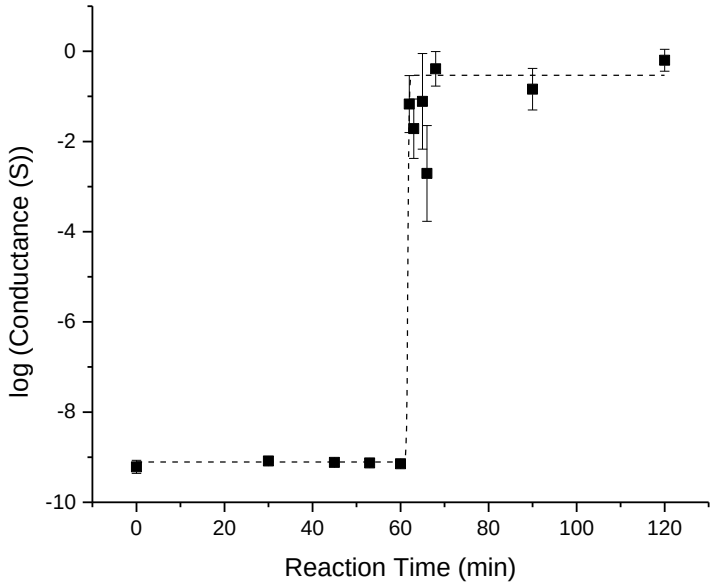

Figure 14: Conductance vs growth time for chemically-grown silver layers on nylon. Standard deviation values for non-percolated samples were on the order of 10^{-11} S. The sigmoidal best fit line ($R^2 = 0.995$) was calculated using the Dose-Response function in OriginPro.

Although the percolation threshold took place around 15 nm thicknesses and 61-minute growth time for thermally-grown and chemically-grown layers, respectively, it should not be concluded that at the chemically-grown silver layers reach a thickness of 15 nm at a growth time of 61 minutes. AgNPs growing in suspension for 61 minutes have previously been determined to be 50 nm in diameter;[45] SEM micrographs from earlier studies have shown these larger nanoparticles get abstracted from suspension to the surface of the nylon.[16] These micrographs also show that silver grown directly on nylon is smaller than these adsorbed nanoparticles, so it is possible that 15 nm is the average height between these two types of AgNPs on nylon. To confirm whether this is the case, thicknesses of the samples prepared under either condition

would have to be measured. A proposed method for doing this is ellipsometry, as done in the Oates study referenced earlier.[18] Further, this experiment needs to be followed up with a wider range of layer thicknesses for silver prepared thermally, especially between 10-20 nm. It is expected that the broadness of the vertical jump in the sigmoid for thermally-grown silver is attributed to only having measured silver layers at four different thicknesses. Also, non-percolated silver layers in Figure 13 had significantly higher conductivity than bare nylon, indicating that 10 nm may not be uniformly non-percolated. This could be the result of having probed only four locations on each surface; if the four locations chosen happened to be non-percolated but there was significant connection of silver elsewhere along the surface, then surface conductance was overestimated. To prevent this in the future, any replication should be done with more than four trials along any surface. Either way, the point in AgNP growth for either fabrication method at which coalescence is reached on nylon was tentatively identified, and allows a new avenue for exploring the utility of these methods for SERS applications.

Based on previous discussions about these conductivity plots, the literature suggests surface enhancement is best at growth thicknesses (for thermally-grown layers) and growth times (for chemically-grown layers) just before and just after the vertical discontinuities shown in Figures 13 and 14. For thermally-grown silver, this refers to layers grown at 10 nm and at 20 nm. Due to having both more complete data and more consistent standard error values for 30 nm layers (see section A.5), thermally-grown silver with layer thicknesses of 30 nm were chosen for further study. Therefore, the following Raman measurements utilized two types of thermally-grown layers: 10 nm layers, referred to as “non-percolated thermally-grown silver,” and 30 nm layers, or “percolated thermally-grown silver.” For chemically-grown silver, the two growth times tested closest to the threshold, outside of the range discussed above, were determined to be

at 53 and 90 minutes; samples with these growth times were used for the remainder of the study and referred to, respectively, as “non-percolated chemically-grown silver” and “percolated chemically-grown silver.”

4.2 Contact angle hysteresis measurements

The establishment of a coffee ring from a hydrophilic droplet is more pronounced on a hydrophilic substrate, as discussed earlier. While coffee rings of varying quality are expected for all sample/substrate combinations, well-defined ring stains should provide better separation between solutes. Further, well-defined rings are commonly utilized in drop-coat deposition Raman,[36] since the coffee ring effect concentrates the solute and gives a better signal. Therefore, determining the relative wettability of all substrates should reveal which substrate will give the best signal quality in subsequent Raman analysis. Signal quality is also impacted by surface roughness. For these reasons, static contact angle and contact angle hysteresis measurements were made and reported in Table 2.

Table 2. Contact angle hysteresis averages, standard deviation, and coefficients of variation for bare nylon, and chemically and thermally-grown non-percolated and percolated silver layers on nylon.

		Chemical Deposition		***Thermal Deposition***	
	Bare nylon	*Non-percolated*	*Percolated*	*Non-Percolated*	*Percolated*
Static contact angle (°)	105	78.0	80.0	74.9	81.6
Advancing angle (°)	95.1	97.9	103	98.6	95.3
Receding angle (°)	36.1	26.5	26.1	63.3	65.8
CAH average (°)	59.0	71.3	77.3	35.3	29.4
CAH SSD	16.5	12.3	9.69	11.9	13.6
CAH CV	0.280	0.172	0.125	0.337	0.462

The static contact angles for silver were similar, showing that the AgNP-coated surfaces were consistently hydrophilic, regardless of the method of fabrication or percolation state. As expected, nylon was more hydrophobic. While the advancing angles of all droplets were largely the same, the receding angles for water on silver varied depending on the method of silver growth. Chemically-prepared silver layers had smaller receding angles, while thermally-grown silver showed larger receding angles. Bare nylon showed an intermediate receding angle of the water droplet. Since contact angle hysteresis varies directly with surface roughness (c.f. Section 1.4.1), the data suggests that thermally-grown silver is the smoothest of all substrates prepared in this study. Chemically-grown silver layers were the roughest, and bare nylon had an intermediate roughness. Since the electromagnetic enhancement mechanism for SERS is roughness-dependent,[11] the chemically-grown layers may scatter light more intensely than the thermally-grown layers. For the four silver substrates, within the limit of uncertainty of the measurement, there is only slight variation in contact angle hysteresis between percolated and non-percolated layers, suggesting the method of preparation had more of an impact on the surface roughness than whether the silver was completely covering the nylon.

According to Kumar et al., surface roughness may be related to wettability, as smoother surfaces tend to have smaller hysteresis values.[28] Based on this, the data suggests that the thermally-grown layer is smoother than either bare nylon or chemically-grown silver, and that chemically-grown silver is the roughest of the three layers. AFM measurements of thermally-evaporated silver layers, such as those described by Li et al., tend to show that thermal evaporation leads to qualitatively smoother surfaces than we have seen in SEM micrographs of AgNP-coated swab fibers from previous studies in this lab.[16,46] Collecting surface roughness

measurements of AgNP-coated nylon sheets and swab fibers would be a useful future study to quantify the differences of thermally-evaporated and chemically-deposited silver films.

The difference in storage methods between thermally-prepared and chemically-prepared layers may have played a role in these results. Thermally-prepared layers were kept dry in argon-flushed vessels, whereas chemically-prepared layers were stored in ultrapure water, and allowed to air-dry before conducting contact angle hysteresis measurements. Remaining surface-bound water on chemically-prepared layers may have made these layers more wettable. To confirm this, two follow-up experiments should be considered: 1) heat-drying the chemically-grown layers to evaporate off any remaining water, and 2) storing thermally-grown silver in ultrapure water. The results of these experiments would not only present a more complete picture of how the surface wettabilities of the surfaces prepared by different methods compare, but also elucidate the impact of substrate storage on wettability. Regardless, there was a substantial difference in stain morphology in both simulant and semen stains between chemically-prepared and thermally-prepared substrates, as demonstrated in the next section.

4.3 Raman and SERS spectra

4.3.1 Urea, phenylalanine, choline chloride

Among the solutes of semen that contribute the most to the overall Raman spectrum of the fluid, urea, phenylalanine, and choline were chosen to determine their deposition pattern in semen stains. Below in Figures 15-17 are Raman spectra of each solute, where choline was used in the form of choline chloride. To determine the location of adsorption for each solute, a line scan was conducted along the diameter of every stain. To identify solutes in any spot along the line, a vibrational mode unique to each solute was identified; these markers are indicated by a

star on each spectrum along with a diagram of the molecule made in ChemSketch with the vibration associated with the marker on the spectrum. The marker for urea is at 1012 cm^{-1}, which Frost et al. attributes to the NCN symmetric stretch.[41] For phenylalanine, the marker is located at 1001 cm^{-1} and has been attributed by Jeffers et al. to a ν_{12} symmetric ring stretch.[42] The choline marker was chosen to be 1012 cm^{-1} which, as explained by Akutsu, is associated with CH_2 rocking.[43] Another prominent feature in the spectrum for choline chloride is the 713 cm^{-1} mode, which corresponds to the quaternary ammonium symmetric stretch.[43] These modes are compiled in Table 1.

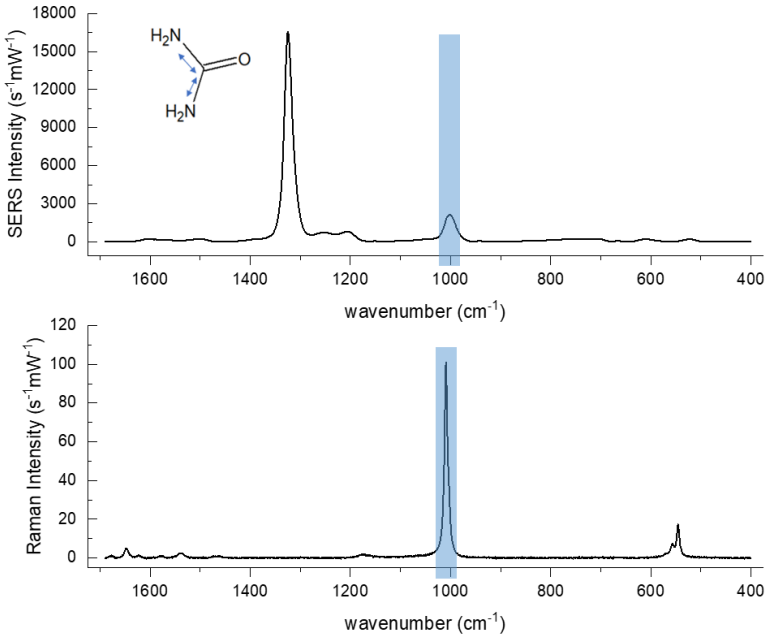

Figure 15: Normal Raman (bottom) and SERS (top) spectra for **urea**. Vibrational mode in blue box corresponds to the NCN symmetric stretch.

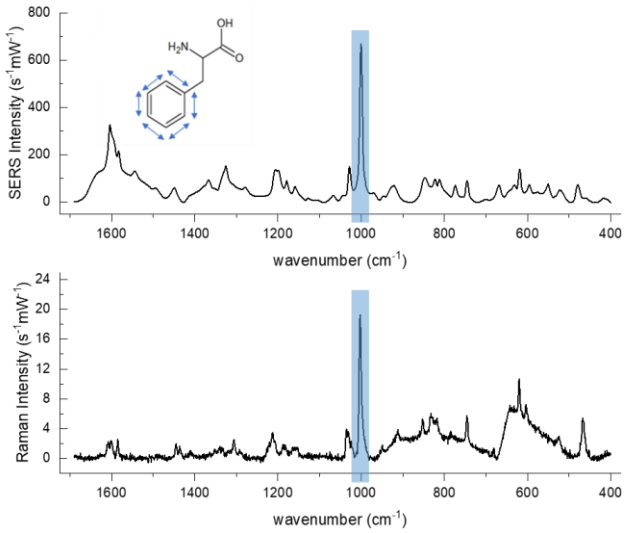

Figure 16: Normal Raman (bottom) and SERS (top) spectra for **phenylalanine**. Vibrational mode in blue box corresponds to symmetric ring stretch.

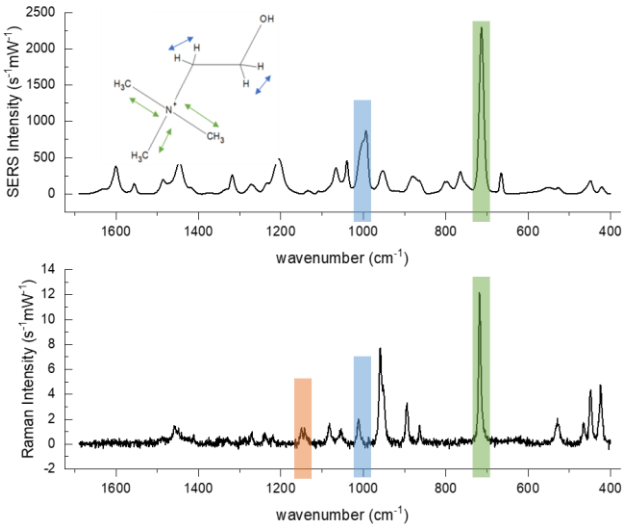

Figure 17: Normal Raman (bottom) and SERS (top) spectra for **choline chloride.** Vibrational mode in blue box corresponds to CH rocking while the mode in the green box corresponds to the quaternary ammonium stretch. The vibrational mode shown in the orange box corresponds to C-C stretching of gauche bonds in nylon,[47] not seen in the SERS spectrum.

Figures 15-17 shows crystalline spectra of urea, phenylalanine, and choline chloride on nylon, next to their respective SERS spectra prepared on sandwiches. The sandwich substrate was used here in lieu of the silver layers from the previous sections due to difficulties in obtaining spectra for urea and phenylalanine solutions. For those solutions, attempts to acquire spectra on the typical thermally- or chemically-deposited AgNP-nylon substrates, resulted in ablation/etching of the sample. This was evidenced by both the rapid visual appearance of dark spots where the laser interacted with the sample and the rapid spectral appearance of broad bands generally associated with carbon samples. This effect was not observed in either choline chloride stains or any mixture containing choline chloride. As will be described later, since choline chloride droplets spread out farther than droplets of urea or phenylalanine, it is expected that the spreading facilitated heat dissipation into the substrate, which circumvented damage to the sample.

As discussed in Section 1.3.1, the plasmon oscillations in irradiated AgNPs lead to a stronger Raman response from the materials deposited onto or near them. This is shown in Figure 17 wherein baseline-corrected standard Raman and SERS spectra for choline chloride are plotted and the overall counts across the choline chloride spectra are higher from the SERS substrate than for nylon. For a quantitative comparison, the analytical enhancement factor (AEF) for spectra of semen simulant collected on each substrate was calculated and reported in Table 3 below. The AEF is a dimensionless value expressing the extent of signal enhancement with respect to a specific vibrational mode, and is defined as

$$AEF=\frac{\frac{I_{\mathrm{SERS}}}{c_{\mathrm{SERS}}}}{\frac{I_{\mathrm{RS}}}{c_{\mathrm{RS}}}} \quad \textbf{[2]}$$

where I_{SERS} and I_{RS} are the intensities of the vibrational mode from averaged spectra collected on a SERS substrate and on a standard (i.e. non-SERS) substrate, respectively, and c_{SERS} and c_{RS} are the analyte concentrations on their respective substrates.[48]

Table 3 provides AEF values for all substrates with respect to the 713 cm^{-1} mode of choline chloride which, as mentioned previously, corresponds to a quaternary ammonium symmetric stretch in choline.[43] Based on the values reported in Table 3, the chemically-grown silver layers afford the strongest signal enhancement, with the non-percolated layer providing more signal than the percolated layer. The smallest signal enhancement comes from the percolated thermally-grown substrate.

Table 3: Analytical enhancement factors for each substrate with respect to the 713 cm^{-1} mode in choline chloride.

Substrate	***713 cm^{-1} intensity - integrated*** *($s^{-1}mW^{-1}$)*	***Choline chloride concentration*** *(moles/mm^2)*	***AEF***
Nylon	13.3	$1.56x10^{-5}$	--
Non-percolated thermally grown	$4.06x10^{5}$	$7.04x10^{-5}$	674
Percolated thermally grown	$1.27x10^{5}$	$2.66x10^{-5}$	558
Non-percolated chemically grown	$9.32x10^{5}$	$7.20x10^{-6}$	$1.51x10^{5}$
Percolated chemically grown	$7.08x10^{5}$	$6.66x10^{-6}$	$1.24x10^{5}$

The difference between the values presented in Table 3 are attributed to differences in surface roughness, since similar trends were found in the contact angle measurements summarized in Table 2, which demonstrated a significant change in wettability between

chemically-grown and thermally-grown layers. Both tables suggest that the chemical growth process resulted in rougher silver layers. This is consistent with the understanding that rougher surfaces allow for more hot spots to be established on a surface, since adsorbed solutes are likely to be affected by electric fields from plasmon resonances on neighboring AgNPs. However, the percolated chemically-grown layer was more wettable than the non-percolated chemically-grown layer, yet the latter has a larger AEF. Since the CAH values for chemically-grown layers from Table 2 are close together, and the differences in their AEF values are much starker, Table 3 provides more evidence that a follow-up study on the CAH measurements should be undertaken in the future to confirm wettability trends.

4.3.2 Semen simulant

As discussed in Chapter 3, the "simulant stains" were three-component solutions meant to mimic the Raman response of semen, and were made by mixing together three of the solutes found in semen: urea, phenylalanine, and choline chloride. 20 μL droplets of the simulant were deposited onto bare nylon, thermally-grown silver (both non-percolated and percolated), and chemically-grown silver (both non-percolated and percolated), and a line scan was taken along each stain. An example of this simulant stain preparation is given in Figure 18. The 1000 cm^{-1} mode was used for each stain because of its presence across all three solutes and marked enhancement between nylon and silver substrates.

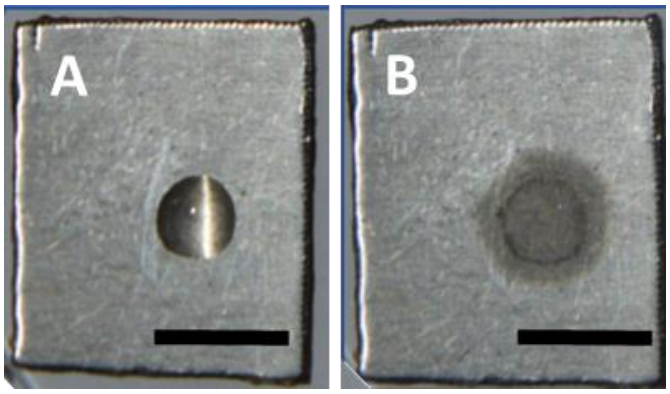

Figure 18: Semen simulant stain deposited on percolated chemically-grown silver. Left: droplet immediately after deposition. Right: stain after drying. Scale bar in each image is 1 mm.

4.3.2.1 Simulant on non-percolated thermally-grown silver

Both contact angle hysteresis and analytical enhancement factor calculations suggested that thermally-grown silver layers were smoother than their chemically-grown counterparts. Therefore, results on thermally-prepared silver are presented first, since these stains provide a clearer picture of how simulant stains form on silver, with a limited influence of surface roughness on the shape of the stain.

Figure 19 shows a simulant stain on a layer of thermally-grown layer of silver on nylon. Here, the simulation has formed a clear coffee ring as it did on nylon, with a visible ridge at the edges of the stain where solutes were deposited. Notably, the simulant drying involved a discoloration of the surface, the origin of which is posited in Section 4.5. After drying, the stain assumed a light-grey color.

Figure 19: Top-down view of simulant stain formed on non-percolated thermally-grown silver on nylon.

After Raman spectra were collected along the horizontal diameter of the stain, each spectrum was processed as described in Section 3.7 to calculate the peak areas at ca. 1000 cm^{-1} (total area from about 975 cm^{-1} to about 1026 cm^{-1}) for each position along the stain. The results are given in Figure 20 below, with sixth order polynomial curves to indicate possible trends in solute aggregation.

This stain was significantly smaller than the simulant stain formed on nylon (see Section 4.3.2.5), which follows from the contact angle hysteresis data showing that this substrate is more hydrophobic. This stain shows choline on all locations but especially towards the edges of the ring. Based on the fitting curves, urea has a local maximum in the center of the stain. While this could be evidence of the concentric coffee ring hypothesis, there is only slight separation between the solutes. Likewise, given that hydrophobic substrates are less likely to form well-defined coffee rings, the seemingly weak degree of separation may correlate to the results of the

contact angle hysteresis study that indicated that the thermally-grown substrates were hydrophobic. Choline chloride has the largest peak areas, and has a strong degree of overlap with the original data peak areas.

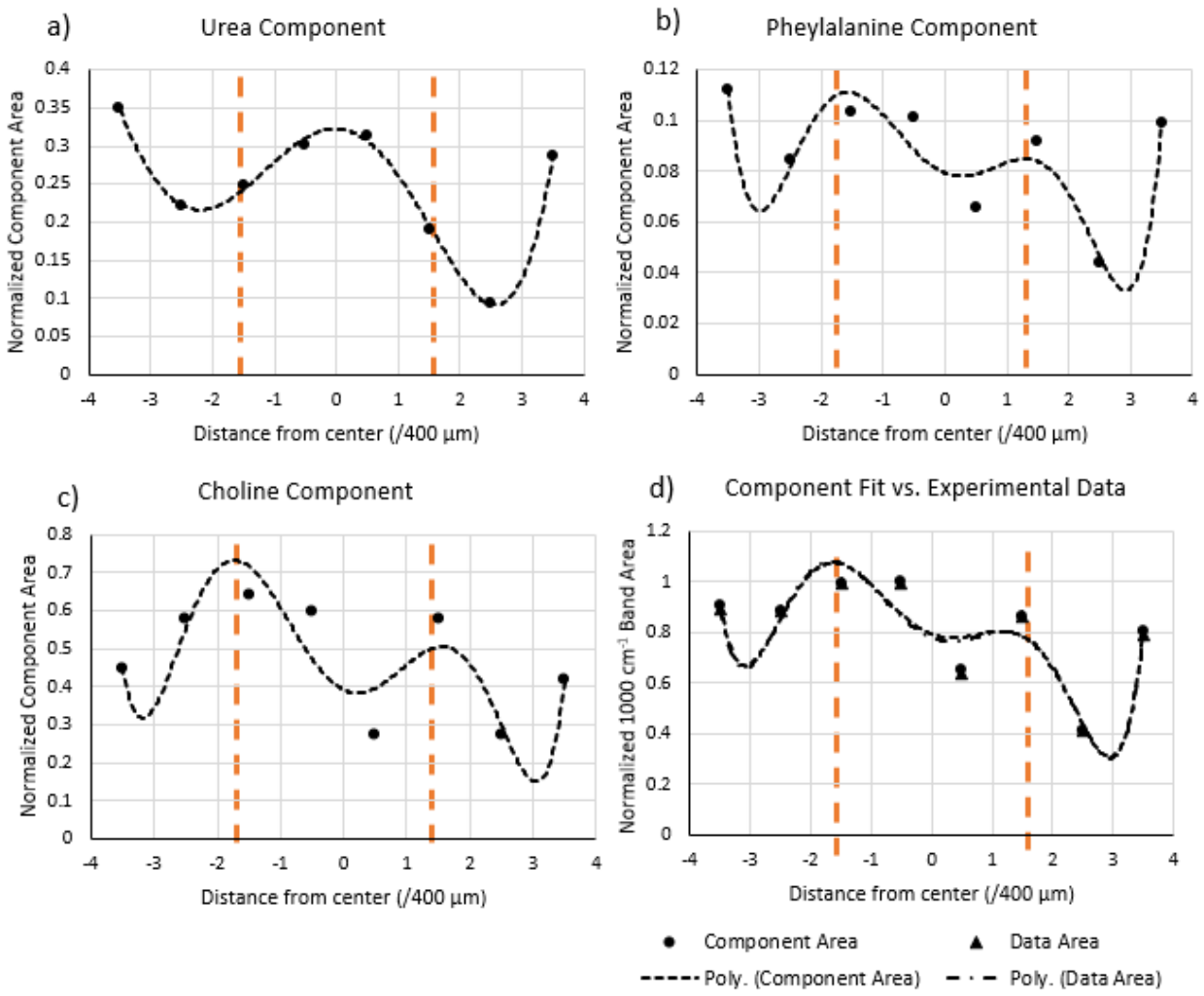

Figure 20: Peak areas of deconvoluted components of a) urea, b) phenylalanine, and c) choline chloride from the 1000 cm^{-1} mode of simulant SERS spectra on non-percolated thermally-grown silver. In d), the sum of these components is given in circles, and the original data area is given in triangles. All curves are sixth order polynomials. Orange lines demarcate the locations where the line scan is presumed to have intersected the contact line of the droplet.

4.3.2.2 Simulant on percolated thermally-grown silver

Figure 21 shows a simulant stain that appears very similar to the stain on non-percolated thermally-grown silver shown in Figure 19, in that a clear boundary to the stain is visible, and the discoloration around the stain is a light grey. Interestingly, not only is the stain itself larger than that of Figure 19, but the region of discoloration on the substrate is much larger.

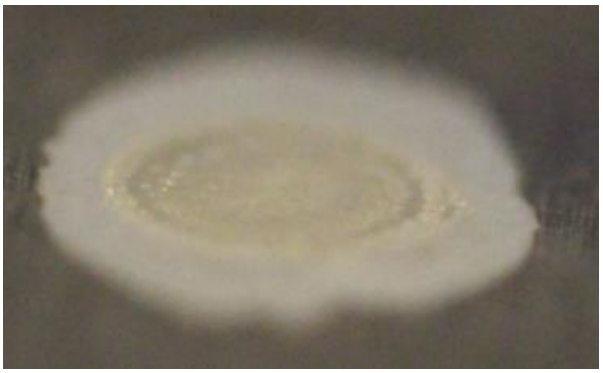

Figure 21: Side view of simulant stain formed on percolated thermally-grown silver on nylon.

In Figure 22, the peak areas from each solute trace out the same shape, with higher intensities corresponding to the edges of the stain, and a local minimum in the center from which solutes were carried away by capillary flow during stain formation. Here, the area of discoloration is much larger than it was for the non-percolated thermally-grown substrate. Spectra acquired in these discolored regions did show vibrational modes consistent with choline chloride (see Appendix sections A.1 and A.2).

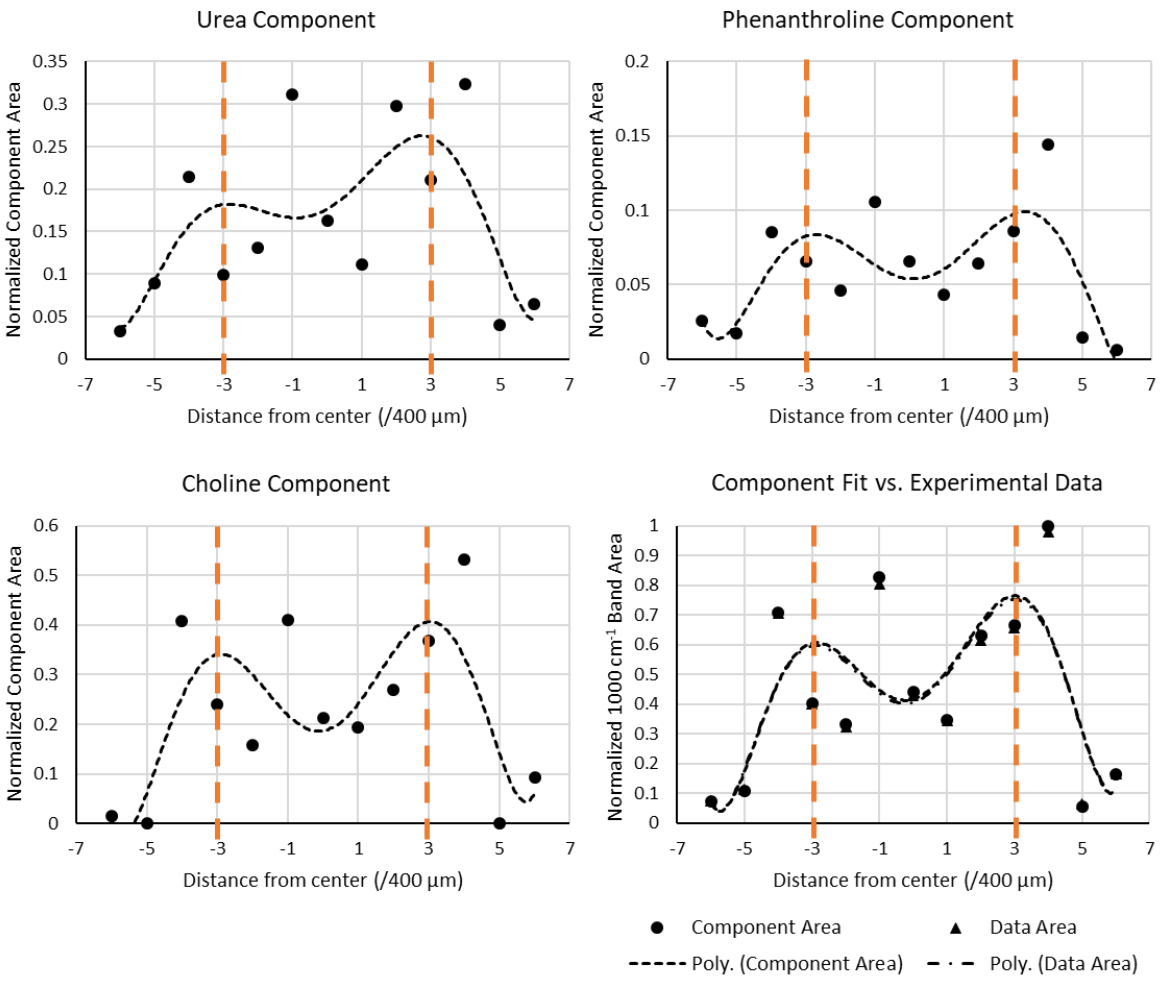

Figure 22: Peak areas of deconvoluted components of a) urea, b) phenylalanine, and c) choline chloride from the 1000 cm^{-1} band of simulant SERS spectra on percolated thermally-grown silver. In d), the sum of these components is given in circles, and the original data area is given in triangles. All curves are sixth order polynomials. Orange lines demarcate the locations where the line scan is presumed to have intersected the contact line of the droplet.

While there is some slight variability in the shape of the best fit curves in Figure 22, the panels are remarkably similar indicating little separation. To investigate further, the full spectra, from which the ca. 1000 cm^{-1} band areas were extracted in Figure 22, were used to conduct

principal component analysis (PCA) using OriginPro software. Three principal components accounted for 99.2% of the variance between the 13 spectra collected across the diameter of the stain on a percolated, thermally-grown silver substrate. Principal component scores for each spectrum were used to calculate the Euclidean distance between each spectrum. In Figure 23, the results of that analysis are shown in which the scores of the first two components are plotted in Panel A and a heat map of Euclidean distances between spectra is shown in Panel B. The data indicates that while there is some variation at the edges of the stain, there is limited spectral variation throughout most of the stain. Thus, the variations in shape seen in the plots of Figure 22, are more likely mainly due to differences in concentrations of the solutes, along with perhaps somewhat subtle differences caused by solute separation during drying.

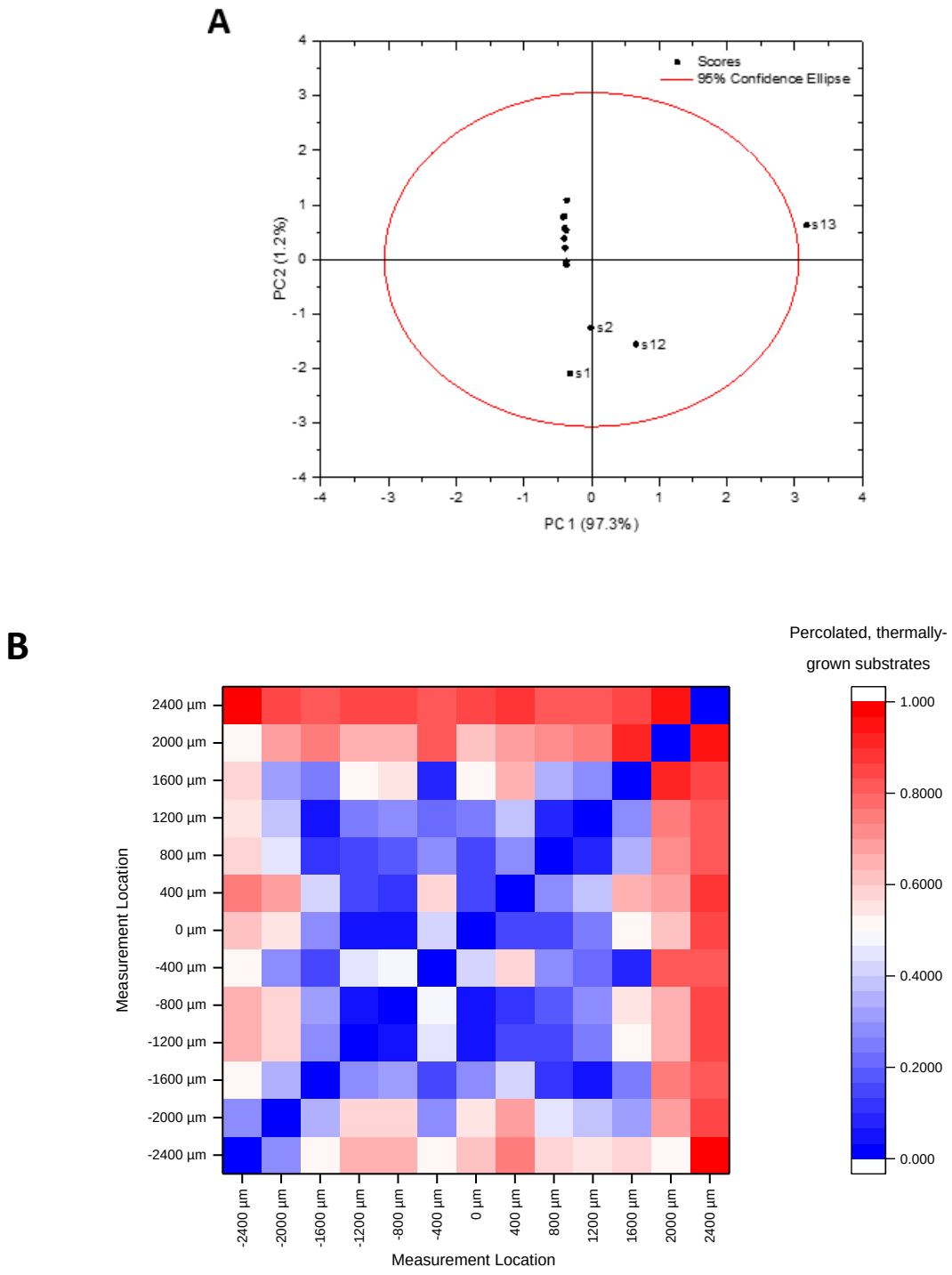

Figure 23: Principal component analysis of semen simulant spectra on percolated, thermally-grown substrates. A score plot is shown in Panel A while a heat map indicating Euclidean distances between spectra is shown in Panel B. The left edge of the stain is indicated as s1 or -2400 microns while the right edge is indicated as s13 or +2400 microns in the two panels.

4.3.2.3 Simulant on non-percolated chemically-grown silver

Figure 24 shows the simulant stain formed on non-percolated chemically-grown silver. The most striking detail of this stain is the discoloration of the silver surface to a golden-brown. These stains were also significantly larger than any stains formed on nylon or thermally-grown silver. Upon closer inspection, the center of the stain was slightly lighter than the edges of the stain; the separation between the lighter and darker zones was demarcated in Figure 23. This may have been the result of a coffee ring formation where some of the solutes are concentrated in the center of the stain. Also, the overall stain shape was not a well-defined ellipsoid as it was on the previous substrates. Small black scratches along the surface were attributed to defects along the bare nylon surface, as well as silver layers hitting each other while stirring together in the reaction vessel during the silver growth process.

Figure 24: Top-down view of simulant stain on non-percolated chemically-grown silver. Black circle added to show outline of contact line from simulant droplet.

The spectral areas given in Figure 25 were consistent with the expected coffee-ring shape: the peak areas were largest near the edges of the line scan, and a local minimum was found near the center of the stain. This shape of the trendlines in Figure 25 suggests the solutes aggregated preferentially toward the edges of the stain and away from the interior. The trendline for the data made the same shape as that of the summed fits, suggesting the component fits may have captured the behavior of the stain.

As seen in Figure 25, phenylalanine had higher peak areas towards the edges of the stain, and choline chlordie had nearly conistent areas all across the stain. The locations of the urea maxima may have been where the line scan intersected the dashed circle drawn in Figure 24. Again, the presence of choline chloride across the stain (see section A.1 for representative spectra) was consistent with the spread of discoloration seen in the figure above. This suggested the discoloration was the result of choline chloride interacting with silver. Further, Figure 25 shows that the choline peak areas largely mimic the peak area trends for the simulant as a whole, meaning choline contributes the majority of the Raman signals detected at any point.

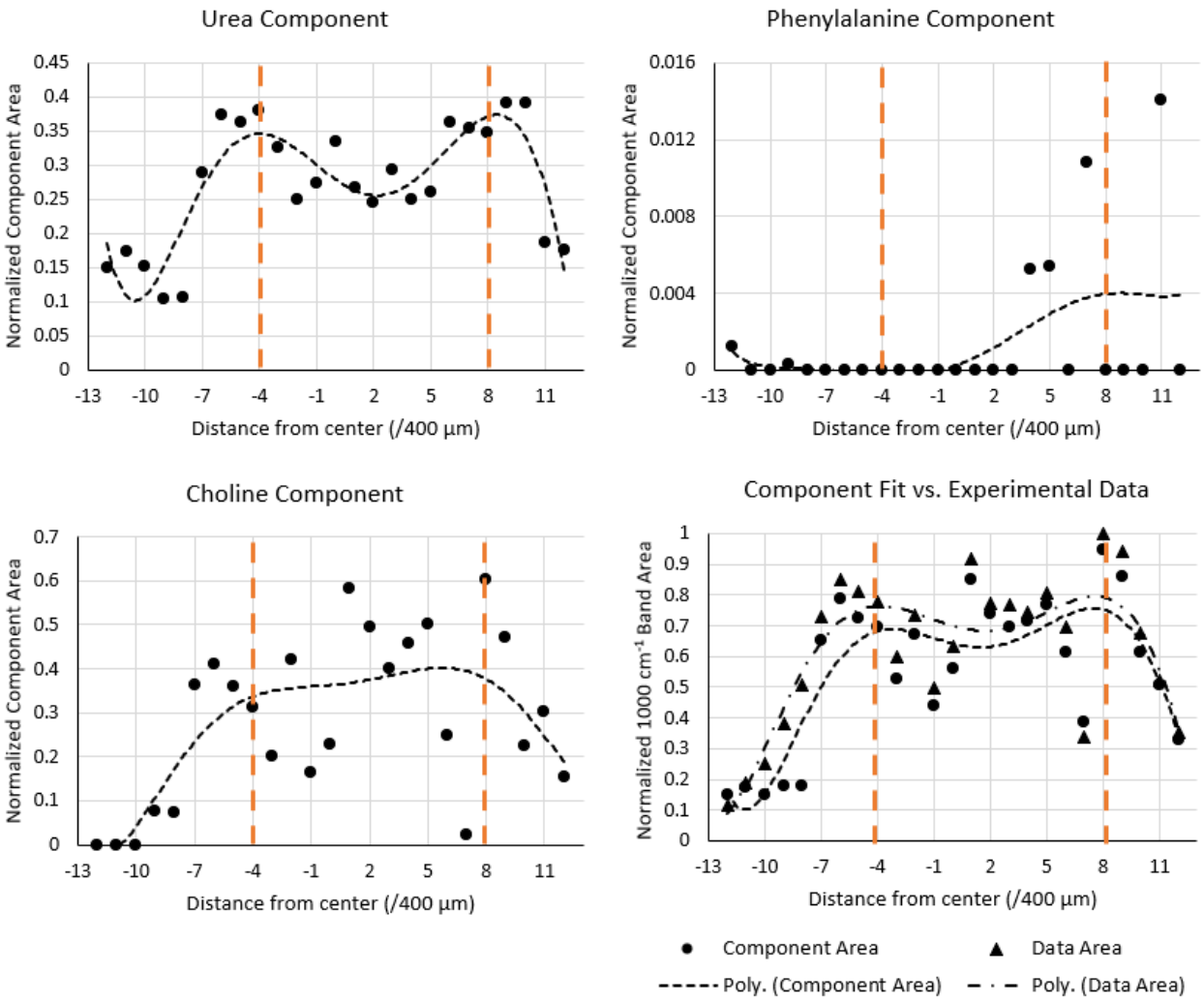

Figure 25: Peak areas of deconvoluted components of a) urea, b) phenylalanine, and c) choline chloride from the 1000 cm^{-1} mode of simulant SERS spectra on non-percolated chemically-grown silver. In d), the sum of these components is given in circles, and the original data area is given in triangles. All curves are sixth order polynomials. Orange lines demarcate the locations where the line scan is presumed to have intersected the contact line of the droplet.

4.3.2.4 Simulant on percolated chemically-grown silver

Macroscopically, the stain in Figure 26 looks the same as it does on non-percolated silver, as opposed to how the simulant stain formed on nylon or thermally-grown silver. The stain assumed a golden-brown discoloration, and the edges were not well-defined. As before, a circle is imposed on the image to separate the inner and outer rings of the stain that have slightly different colorations.

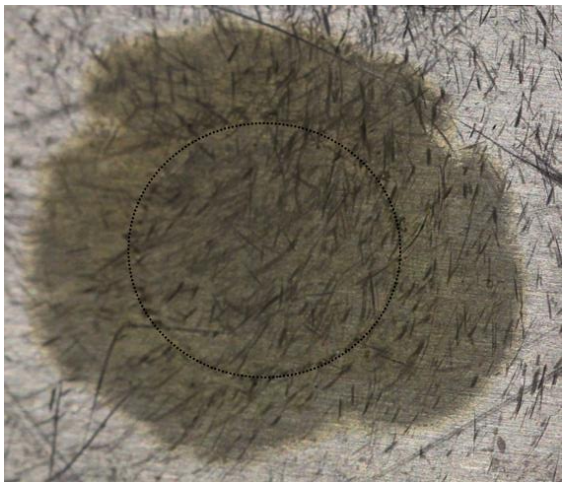

Figure 26: Top-down view of simulant stain on percolated chemically-grown silver. Black circle added to show outline of contact line from simulant droplet.

As before, Figure 27 below shows the normalized peak areas for each solute component fit, and the sum of these component peak areas compared to those of the corrected simulant spectra. The choline component had significant overlap with the data area curve, showing again

that the majority of the Raman signals come from choline chloride. Choline chloride did not have the same constant distribution as it had on non-percolated chemically-grown silver, but the choline intensity was large at all points through the stain, especially compared to urea and phenylalanine, again supporting the idea that the discoloration seen in Figure 26 comes from choline on silver. As seen in Figure 25d, higher Raman signal was gathered from the right side of the stain.

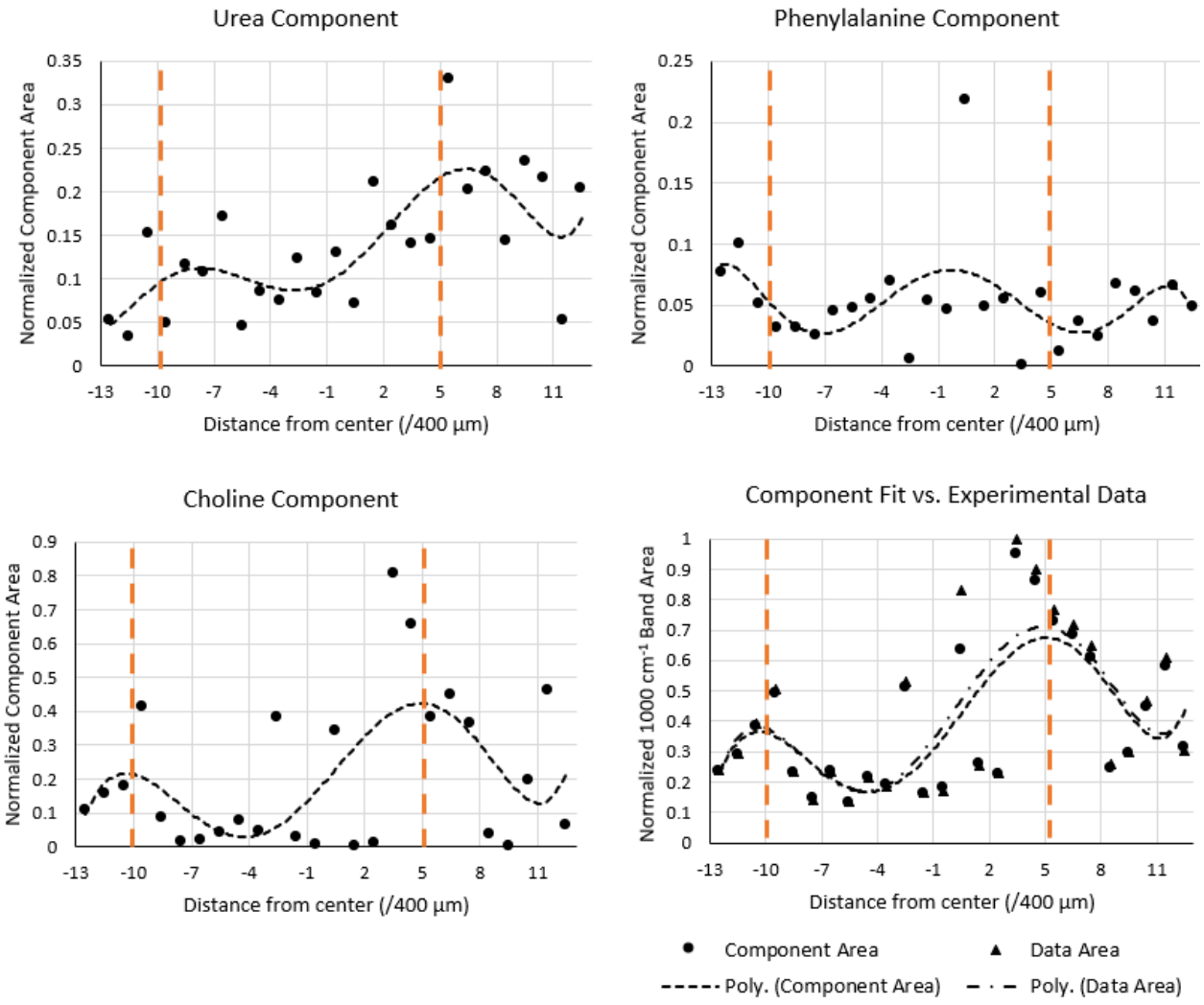

Figure 27: Peak areas of deconvoluted components of a) urea, b) phenylalanine, and c) choline chloride from the 1000 cm^{-1} mode of simulant SERS spectra on percolated chemically-grown silver. In d), the sum of these components is given in circles, and the original data area is given in triangles. All curves are sixth order polynomials. Orange lines demarcate the locations where the line scan is presumed to have intersected the contact line of the droplet.

Overall, the simulant stains demonstrated a large spreading of choline chloride along the silver surface, especially based on the detection of the 713 cm^{-1} mode in choline chloride form spectra taken in the discoloration regions around each stain (see Appendix). These regions of

discoloration surrounded the contact lines for the droplets that resulted in each stain, which is most readily apparent in simulant stains formed on thermally-grown silver. Further, the fact that the dashed lines in Figures 25 and 27 are not symmetric about the origin shows these stains were asymmetric; that is, the center of the wet droplet may not be the same as the center of its respective stain after drying.

Since this spreading and discoloration were not seen on nylon, and because the peak areas for choline chloride were large for the regions of discoloration as well as in the stain, this was believed to be a unique interaction between choline chloride and silver. To confirm this, as well as confirm that the simulant fluid was a faithful approximation of the true biological fluid, semen stains were deposited on bare nylon and chemically-grown silver; the results from their respective Raman measurements are discussed in the next section.

4.3.2.5 Simulant on bare nylon

After the simulant stain was allowed to dry on bare nylon overnight, the stain formed the coffee ring shown in Figure 28 below. The boundaries of the stain are easily perceptible because of the aforementioned deposition of solutes to the periphery. As discussed previously, the stain does not necessarily form a perfect coffee ring, especially on a hydrophobic substrate, which accounts for the appearance on the interior of the stain.

Figure 28: Simulant stain (urea, phenylalanine, and choline chloride in ultrapure water) on bare nylon.

A line scan was taken across the horizontal diameter of the simulant stain on nylon. The method of processing the data was similar to what was outlined above, with the exceptions that fitting was based on crystalline urea, phenylalanine, and choline chloride rather than from dried solutions on the nylon substrate. The results of simulant fitting data are given in Figure 29 below. The results are limited given that urea and phenylalanine were poorly detected without the aid of SERS, and as such the "component fit" has much poorer agreement with the data (cf. Figure 29d) than shown in previous figures, such as Figure 27d. Of note however, is that the total area of the ca. 1000 cm^{-1} band across the stain seems to vary much less than the simulant stains made on silvered substrates.

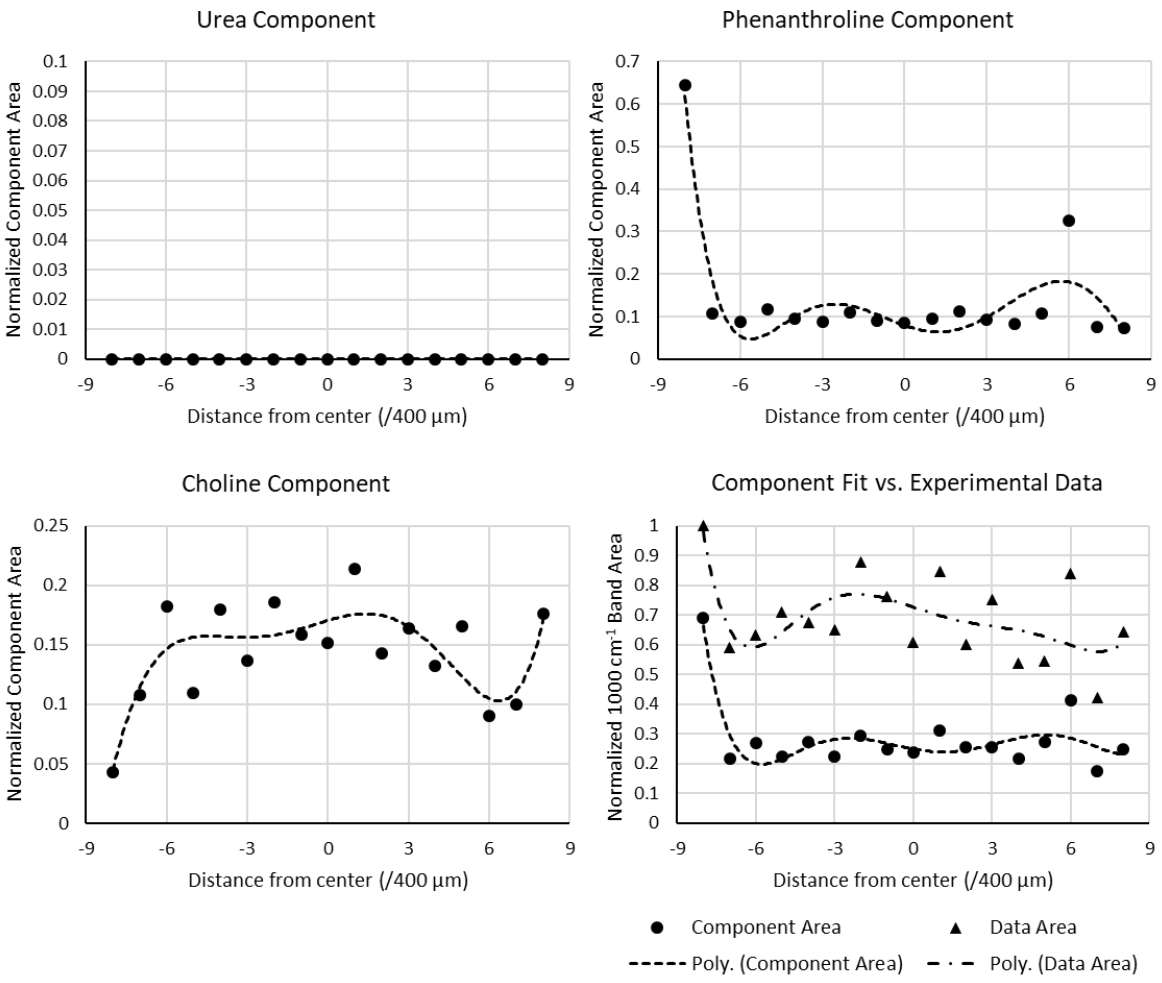

Figure 29: Deconvoluted components of a) urea, b) phenylalanine, and c) choline chloride from the 1000 cm^{-1} mode of the length of simulant spectra on bare nylon. In d), the sum of these components is given in circles, and the original data area is given in triangles; these were plotted together to show similarity between the fit and the original data. All curves are sixth order polynomials.

4.4.3 Semen

Whilst one of the objectives of determining the percolation threshold for silver on nylon was to determine how the extent of silver growth affects signal enhancement from SERS, initial attempts at collecting Raman spectra on pristine semen stains on any substrate were unsuccessful. The same issue was encountered previously.[16] As a result, 20 μL droplets of silver nanoparticle suspension were deposited onto these stains after they had already dried to yield the Raman peak areas presented in this section; an example of this is shown on nylon in Figure 30 (see section A.2 in the Appendix for individual spectra collected along the stain diameter on silver substrates). For either of the semen stains on bare nylon in Figure 30, it did not appear that significant spreading had occurred as it had on the silver-coated surfaces in the previous section. While the addition of AgNP suspensions in previous studies as well as this one (particle concentration typically 10^{12} mL^{-1}) was initially intended to enhance signal through the SERS effect, in retrospect it is more likely that the benefit may have more to do with the dilution of semen. In order to keep consistency throughout the experiments, the analyte was pipetted onto a substrate. The viscosity and total solute concentration of semen may inhibit close contact of analytes of interest with the SERS substrate, which is necessary for strong signal. Dilution of the semen lowers viscosity and total concentration allowing for better contact of analyte with the substrate and better ability to have both analyte and substrate within the laser collection volume. While the previously developed protocol of mixing AgNP with a neat semen stain was used here, in future studies a better alternative may be to dilute semen with water before pipetting or allow neat semen to dry on glass, wet a SERS substrate and press the wet substrate to the dried stain to better replicate the procedure in which semen samples would be collected on a swab.

The semen stains prepared on nylon, whether AgNPs were added after they had dried, did not provide adequate spectra and were thus not processed in the way the simulant spectra were; the Appendix contains individual spectra of semen on nylon after the nanoparticles were incorporated. Since previous studies have shown Raman spectra are obtainable for semen on silver swabs, it was concluded that the silver surfaces do provide some surface enhancement but hot spot enhancement, like what is accessible on silver-coated swabs, is necessary in order to yield sufficient signal.

Figure 30: Bottom-left: top-down view of semen stains on nylon, top-right: semen stain with AgNPs added, which resulted in the dark-brown color of the stain.

4.3.3.1 Semen on non-percolated chemically-grown silver

The semen stain formed non non-percolated chemically-grown silver appeared very similar to the simulant stain formed on the same substrate. The main difference was that the discoloration of the substrate did not appear to spread as far as it had for the simulant stain. As stated previously, the silver nanoparticles to augment the Raman signal were added after the stain had already formed; the discoloration was already present and was not an effect of the additional AgNPs. Further, Figure 31 shows the AgNPs did not spread over the entire area of the droplet; this suggests the AgNPs were constrained within the contact boundary of the droplet.

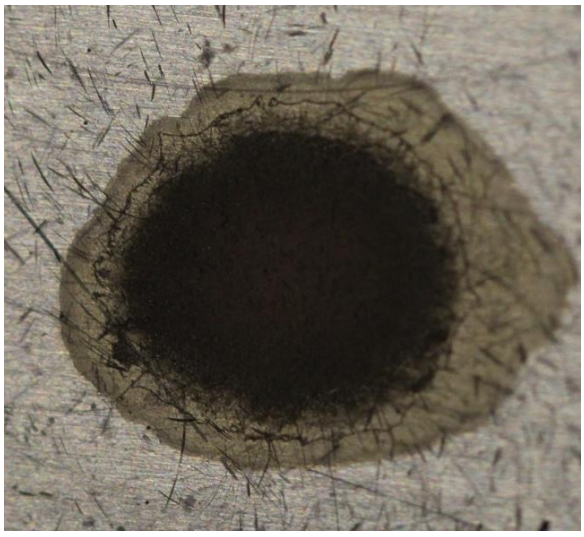

Figure 31: Top-down view of semen stain on non-percolated chemically-grown silver, with additional AgNPs added to the stain for further signal enhancement.

For the Raman analysis of semen on the non-percolated silver substrate, the 1000 cm^{-1} band fittings done for the simulant data did not detect the presence of choline at nearly any spot throughout the semen stain and resulted in poor fit overall. Therefore, the 713 cm^{-1} mode associated with symmetric stretching of the quaternary ammonium group in choline was used instead for fitting and peak area calculation. Given that choline should be the only signal contributor at this location, at least among choline, phenylalanine, and urea, only the choline component data and the overall collected data are reported. As seen in Figure 32 below, the shape of the integrated area profile is similar to that seen in the simulant stains (cf. Figure 25). A significant choline signal was detected at all locations along the stain. Although the choline peak areas were largest at the edges of the AgNP-filled ring, the areas were still substantial throughout the regions of discoloration, reinforcing the idea that choline was interacting with the silver substrate to cause this spreading and color change (see Section 4.5).

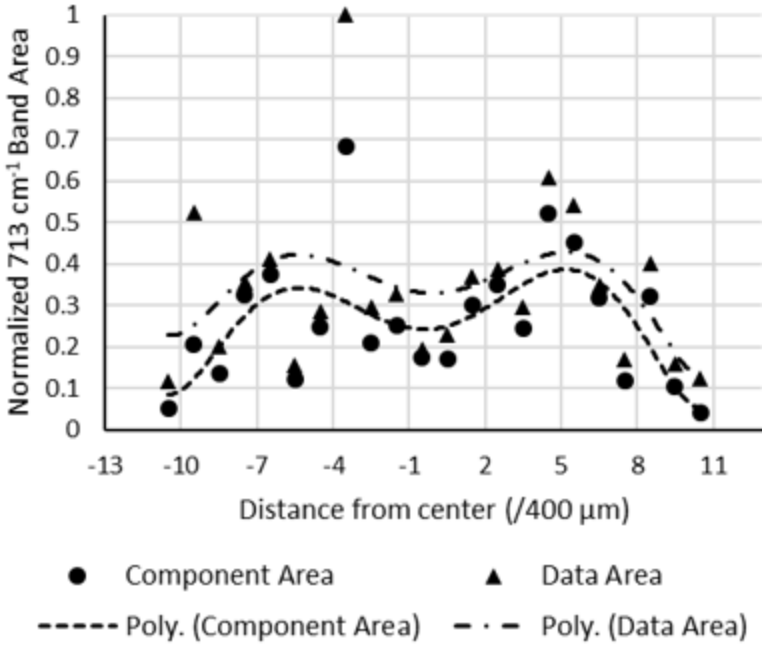

Figure 32: Peak areas of the sum of the three simulant components and the original data area for spectra collected from semen on non-percolated chemically-grown silver. All curves are sixth order polynomials.

Similar to the analysis that was completed for the simulant, PCA analysis was done for the spectra collected while moving across the stain diameter. Six principal components accounted for 86% of the variance between the 22 spectra collected across the diameter of the stain on a percolated, thermally-grown silver substrate. Given that semen is a mixture comprised of a large amount of solutes, this is not surprising. Principal component scores for each spectrum were used to calculate the Euclidean distance between each spectrum. In Figure 33, the results of that analysis are shown in which the scores of the first two principal components are plotted in Panel A and a heat map of Euclidean distances between spectra is shown in Panel B. The data indicates that there is more variation in spectra than seen previously (cf. Figure 23). However,

Panel A does not give any indication of clustering that would be expected if there were phase separation of the Raman-active solutes. In Panel B, the heat map indicates that the spectra at the center of the stain and at the locations that correlate to the contact line of the droplet are most similar (blue) with increased variability between those points (white). While, as before, the edge spectra seem to be slightly more distinct than the interior spectra, the greatest differences occur due to a single spectrum (s8, -1200 μm, see Appendix), which may have been caused by contamination or greater spectral sampling of the underlying nylon substrate.

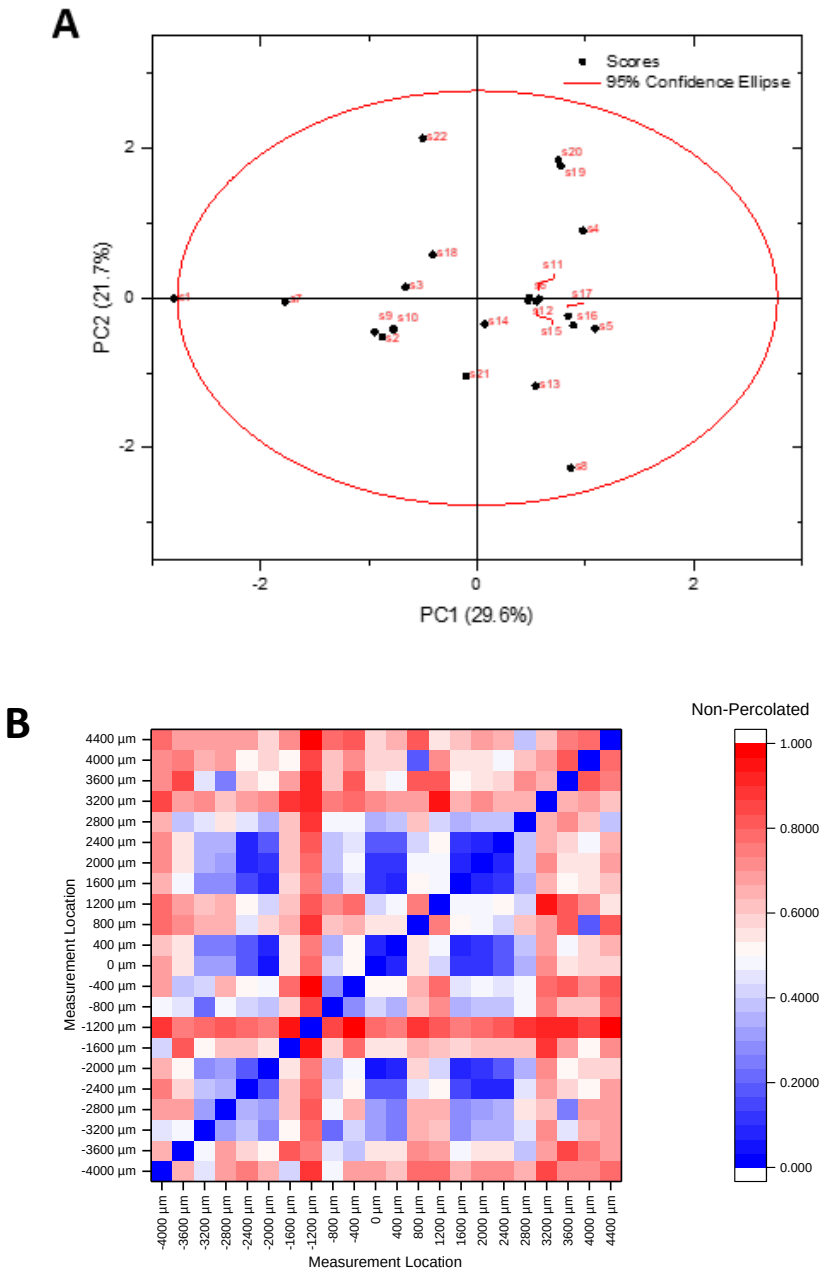

Figure 33: Principal component analysis of semen spectra on non-percolated, chemically-grown substrates. A score plot is shown in Panel A while a heat map indicating Euclidean distances between spectra is shown in Panel B. The left edge of the stain is indicated as s1 or -4000 microns while the right edge is indicated as s22 or +4400 microns in the two panels.

4.3.3.2 Semen on percolated chemically-grown silver

Figure 34 shows the semen stain formed on percolated chemically-grown silver. The semen stain closely resembles the one formed on non-percolated silver. Again, the AgNPs added to improve the Raman signal stayed in the interior of the droplet and did not extend to the area of discoloration around the stain. This stain appeared slightly more misshapen than the one from Figure 31, so at the very least they likely have similar wettabilities, which supports the contact angle hysteresis measurement findings.

Figure 34: Top-down view of semen stain on percolated chemically-grown silver, with additional AgNPs added to the stain for further signal enhancement.

For Figure 35, the 713 cm^{-1} mode of choline was used in lieu of the 1000 cm^{-1} mode in order to capture the distribution of choline in the droplet, which fittings of the latter mode were

not able to do. Choline was found at all locations along this stain, with a shape similar to that seen with the simulant on a percolated, chemically-grown substrate (cf. Figure 27). This extended to the edges of the droplet where discoloration was seen, once again supporting the idea that this golden-brown region was a result of a choline-silver interaction. This spreading, however, did not seem to be affected by the addition of AgNPs to the center of the stain.

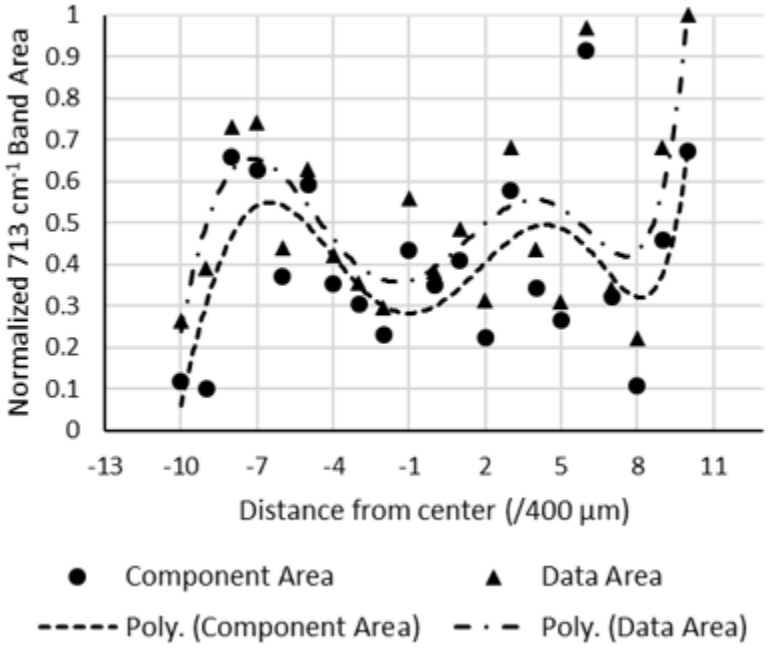

Figure 35: Peak areas of the sum of the three simulant components and the original data area for spectra collected from semen on percolated chemically-grown silver. All curves are sixth order polynomials.

In Figure 36, PCA analysis (6 principal components, 80% of total variance) of the spectra across the percolated, chemically-grown silver substrate shows a pattern somewhat different than that of the non-percolated substrates shown in Figure 33. The score plot, shown in Panel A seems to indicate that a majority of the data is concentrated in one area of the plot while a few other spectra are closer to the edge of the confidence ellipse. The heat map in Panel B indicates that the spectra at the right edge of the stain are markedly different than the majority of the stain. However, unlike the non-percolated substrates, the interior of the stain seems to be somewhat more homogeneous. In Figure 33, the Euclidean distances between the spectra at the contact edge and the center were near zero and thus appearing as large islands as dark blue as the diagonal. In the case of the percolated substrate, those similarities seem to be not as strong, perhaps indicating slightly more separation of components across the stain. The spectra in Figure 36 Panel A appear to form two clusters; one including spectra 1, 2, 8, 13, and 19, and the other including all the others. Figure 37 below shows averages of the spectra in the two apparent clusters in Figure 36 Panel A. These averaged spectra were very similar to each other, so what appears to be potential grouping of the scores in Figure 36 Panel A may just be happenstance and not truly indicative of significant variation.

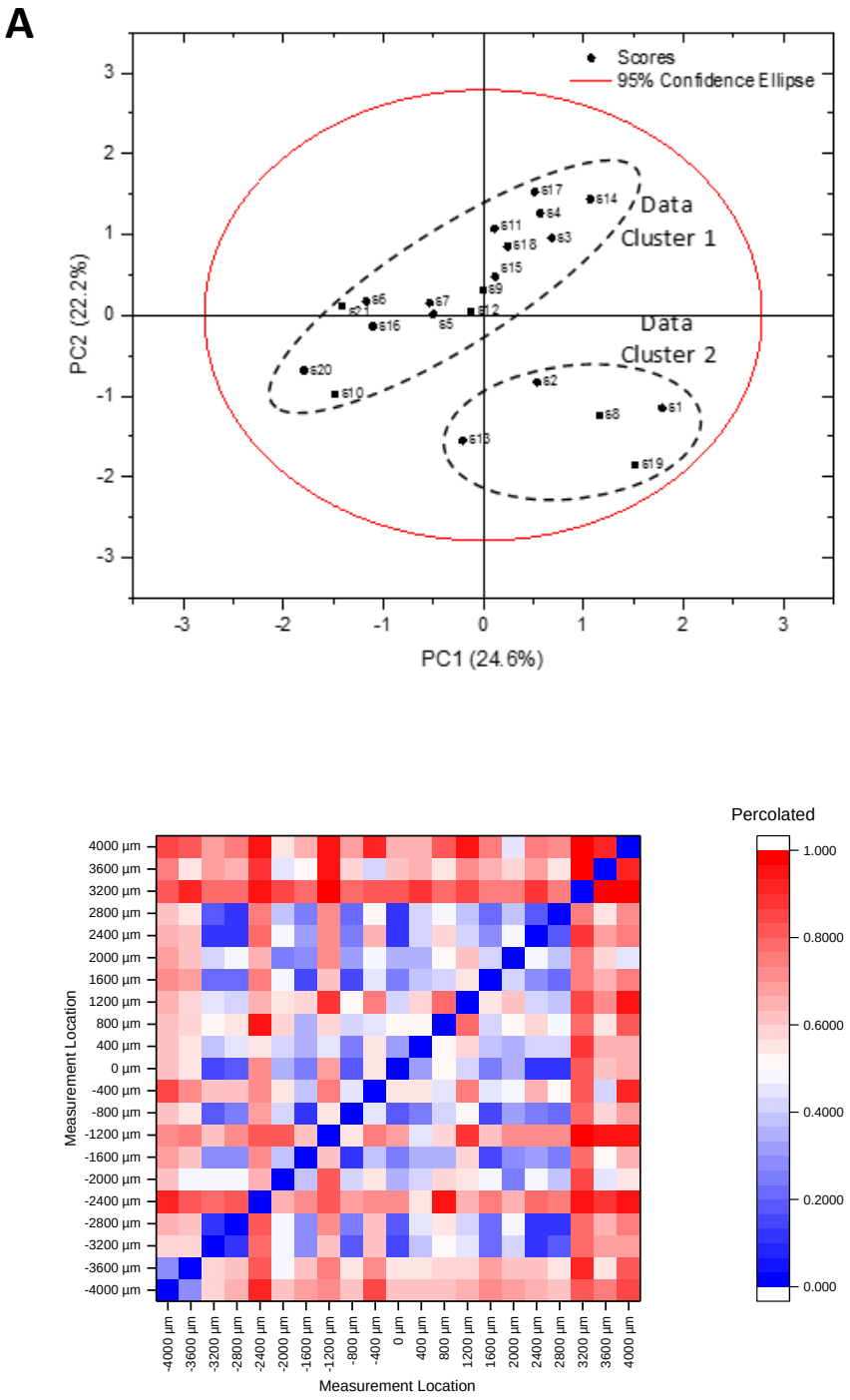

Figure 36: Principal component analysis of semen spectra on percolated, chemically-grown substrates. A score plot is shown with clusters traced in dashed ovals in Panel A while a heat map indicating Euclidean distances between spectra is shown in Panel B. The left edge of the stain is indicated as s1 or -4000 microns while the right edge is indicated as s21 or +4000 microns in the two panels.

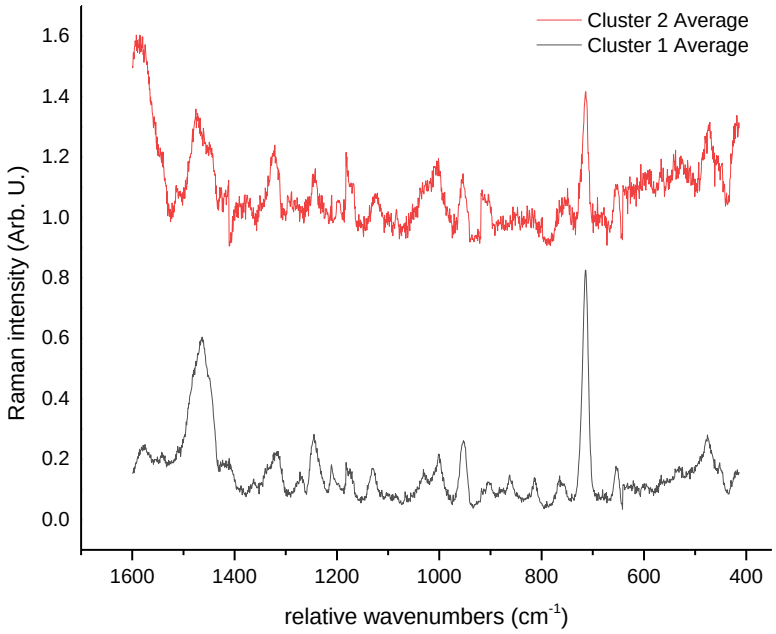

Figure 37: Average semen spectra from Cluster 1 (s1, s2, s8, s13, s19) and Cluster 2 (all others) from Figure 36 Panel A.

4.4 Inter-substrate fitting comparisons

To further clarify the impact each substrate has on the spreading of each component in the simulant, the calculated component fits for each solute, as well as the sums of all components, were plotted for each substrate in Figure 38. Each panel of Figure 38 shows not only the relative size of each component trace, but the changes in distribution for each solute as the substrate was changed, as reflected by the local maxima and minima in each curve.

As was seen previously, solute distribution was most largely impacted by the silver layer fabrication method as opposed to growth time or thickness; in other words, the clearest

difference between the fitting curves in Figure 38 is between the simulant data from chemically-grown and the thermally-grown substrates. Due to their higher wettability, the stains are much larger for both non-percolated and percolated chemically-grown substrates. There is no clear association between the trendlines for substrates made through different methods but grown to the same percolation state. That is, for all three substrates, the two non-percolated layers did not exhibit similar distributions, nor did either percolated substrate.

Interestingly, among all of the substrates, the percolated thermally-grown silver was the only surface upon which, for all solutes, the distribution appears identical. Given that the shape of the distributions and the position of the maxima in peak areas were seen at the same positions for each solute, it would indicate that the solutes separate least on the percolated, thermally-grown substrates.

The behavior of choline chloride on non-percolated chemically-grown silver was unique, given that it is the only curve in Figure 38 to form a plateau for a substantial range. Out of all combinations of solute and substrate, this was the only case where uniform distribution of a solute was seen. Since this plateau is also the maxima of this curve, conceivably this would be very useful for detecting choline chloride on a SERS substrate, since the distribution of the solute affording the best signal is apparently the widest on this substrate. Although further studies and enough replicates to produce statistically significant results would be needed, these results may suggest that the non-percolated chemically-grown silver is the best substrate of the four for detecting choline chloride in simulant stains, and as discussed previously, for detecting semen.

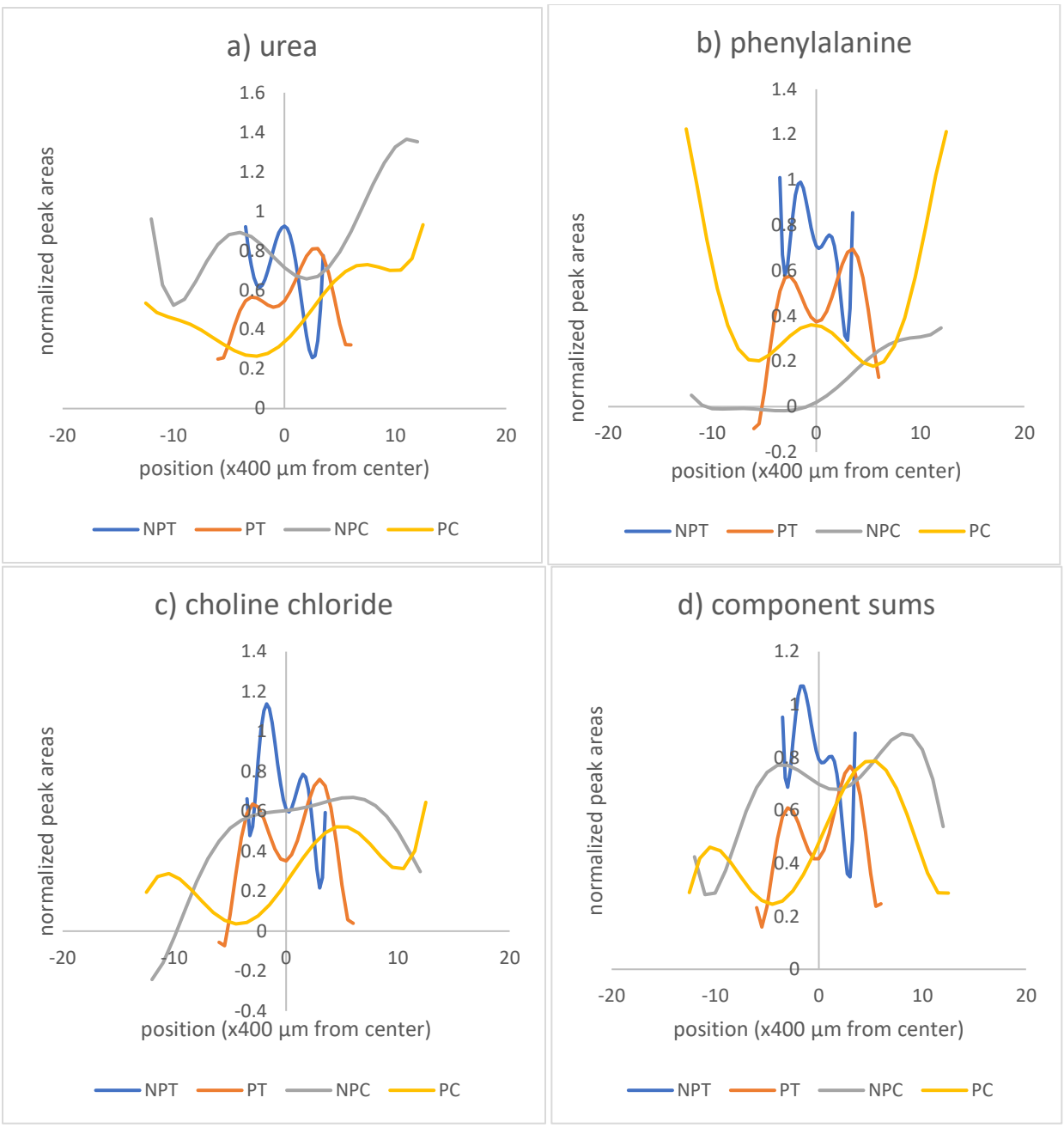

Figure 38: a) urea, b) phenylalanine, c) choline chloride, d) component sums for simulant SERS spectra taken on each substrate. NPT = non-percolated thermally-grown silver, PT = percolated thermally-grown silver, NPC = non-percolated chemically-grown silver, PC = percolated chemically-grown silver.

Figure 39 below compares how well the simulant reproduced the Raman spectra of semen taken along the horizontal diameter of each stain. For both substrates, there appears to be fair agreement between the simulant and semen distributions, in that the same maxima and minima are present, albeit offset from each other. Peak-to-peak distances for each curve in Figure 39 are given in Table 4. These offsets were attributed to differences in viscosity; since semen had a much higher viscosity than the simulant, the semen droplets did not spread out as much as the simulant on either chemically-grown substrate. Additionally, since AgNPs were added to semen stains after they had already dried, these stains would have been rewetted to some extent, and this may have altered where the solutes ultimately deposited in semen stains. A future study should be conducted wherein different volumes of AgNP droplets are added to semen stains to asses any extent of semen rewetting and/or dilution, which would affect where solutes are found in the stain. However, given the agreement of the curves in Figure 39, the addition of AgNPs to the semen stains was presumed to not significantly contribute to any deviation between the simulant and semen.

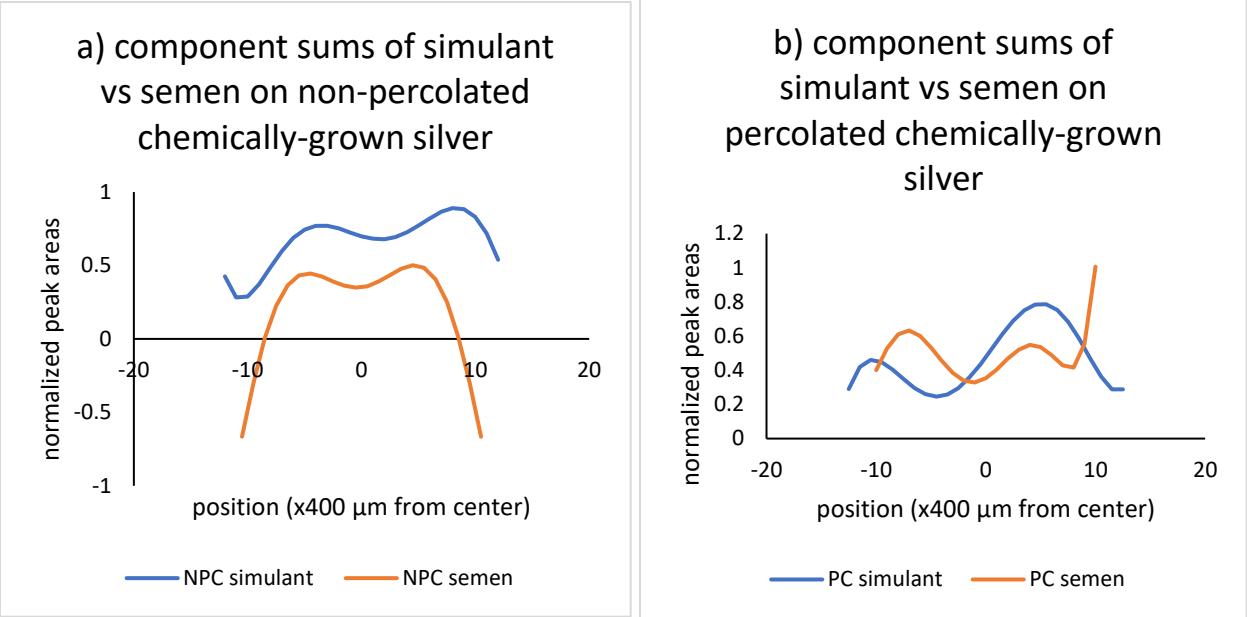

Figure 39: Component sums of simulant and semen fittings on a) non-percolated chemically-grown silver, and b) percolated chemically-grown silver. NPC = non-percolated chemically-grown silver, PC = percolated chemically-grown silver.

Table 4: Peak-to-peak distances for curves in Figure 39.

Substrate/sample	***Peak-to-peak distance (µm)***
NPC/simulant	4800
NPC/semen	3600
PC/simulant	6000
PC/semen	4400

4.5 Stain spreading on silver surfaces

Throughout the previous sections in this chapter, simulant and semen stains were shown to spread very far and discolor the substrate. This effect was only seen on silver substrates with

droplets that contained choline: droplets of simulant fluid, semen, or choline chloride solution. The spreading was not observed for any of these solutions on bare nylon. Therefore, the spreading was believed to be some sort of interaction between choline and silver. Further, the spreading of the simulant stains was much farther than those of the semen stains; this may have been because semen is comprised of a large number of other solutes not captured in the simulant, so any number of these additional solutes may have screened the effect of choline on silver.

The proposed interaction between choline and silver is corrosive electrolyte spreading; the proposed reaction between the choline chloride solution and silver is given as:

$$\mathrm{ChCl} + \mathrm{Ag} \rightarrow \mathrm{AgCl} + \mathrm{Ch}^{+} \quad \textbf{[3]}$$

where Ch = choline. In their research, Dai et al. found that a droplet of an ionic solution reacts with a metallic surface upon deposition and produces an interfacial layer between the droplet and the solid.[49] This interface was more wettable than the original metallic surface, so the droplet spread farther out, which allowed it to reach pristine metal to continue the reaction. This cycle that sustains the reactive spreading of the droplet is summarized in Figure 40 below. It is important to note that applying the mechanism from the drying study assumes the interfacial layer, or product of this reaction, is more wettable than silver. To confirm this, contact angle measurement should be performed on planar silver chloride layers produced by means other than reactions between choline and silver.

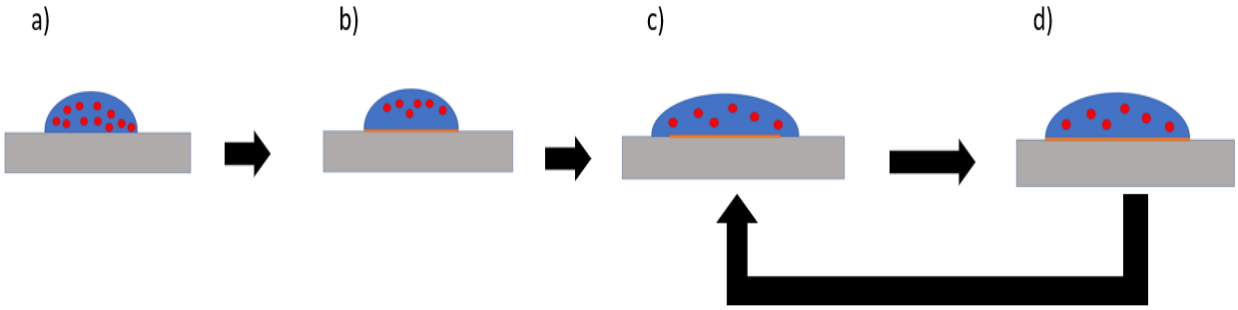

Figure 40: proposed reactive droplet spreading mechanism. a) A droplet (blue) containing dissolved choline chloride (red) is deposited on a silver substrate (grey). b) choline chloride reacts with silver, yielding an interfacial silver chloride layer. c) the interfacial layer is more wettable than silver, so the sessile droplet spreads further. d) the silver surface that is now coated by the droplet reacts with choline chloride. The droplet will again spread further, and a cycle is established between c) and d).

To assess the possibility of chemical spreading, 20 µL droplets of various solutions were deposited onto silver substrates. In addition to the Raman-active components discussed previously, NaCl was used to determine the effect of the chloride ion in choline chloride solutions. Droplet size was measured before and after drying; their ellipsoidal areas are given below in Table 5 through Table 8. Droplets of urea and/or phenylalanine were included to demonstrate their lack of significant spreading on these substrates. The concentrations of the urea, phenylalanine, and choline chloride solutions were the same as their respective concentrations in the simulant solution; the concentration of sodium chloride was set to the concentration of choline chloride. The data shows that consistent, significant spreading is only seen with droplets of choline chloride on silver. To illustrate this, Figure 41 below shows the progression of choline chloride droplet spreading on silver as a function of time.

Table 5: Changes in areas of stains on bare nylon approximated as ellipsoids.

Nylon	***Wet Area*** *(mm^2)*	***Dry Area*** *(mm^2)*	***Percent Change***
Simulant	16.8	17.1	1.59%
Choline chloride	14.4	19.4	35.0%

Table 6: Changes in areas of stains on non-percolated chemically-grown silver approximated as ellipsoids.

Non-percolated chemically-grown silver	***Wet Area*** *(mm^2)*	***Dry Area*** *(mm^2)*	***Percent Change***
Simulant‡	18.0	62.0	245%
Choline chloride	16.9	70.5	316%
Sodium chloride	25.9	55.7	115%
Urea‡	25.9	25.4	-2.16%
Phenylalanine‡	20.7	24.5	18.4%

‡data collected on chemically-grown silver for 45 minutes

Table 7: Changes in areas of stains on percolated chemically-grown silver approximated as ellipsoids.

Percolated chemically-grown silver	***Wet Area*** *(mm^2)*	***Dry Area*** *(mm^2)*	***Percent Change***
Simulant‡	28.7	81.8	190%
Choline chloride	17.9	198	1010%
Sodium chloride‡	35.3	59.1	67.7%
Urea	26.0	24.7	-4.88%
Phenylalanine	24.7	22.4	-9.54%

‡data collected on chemically-grown silver for 75 minutes

Table 8: Changes in areas of stains on percolated thermally-grown silver approximated as ellipsoids.

Percolated thermally-grown silver	***Wet Area*** *(mm^2)*	***Dry Area*** *(mm^2)*	***Percent Change***
Simulant	17.8	274	1410%
Choline chloride	14.4	364	2420%
Phenylalanine	10.8	8.55	-21.1%

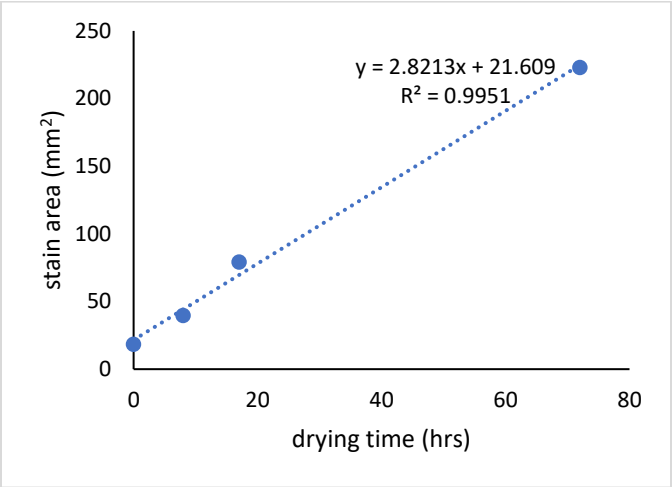

Figure 41: Progression of spreading of a 20 µL droplet of choline chloride on non-percolated chemically-grown silver. The trendline suggests that the stain spreads linearly with time, at a rate of approximately 2.82 mm^2/hour.

Table 9 below shows the results of t-tests for simulant and choline chloride stains before and after drying. On bare nylon, only the choline chloride stain grew significantly while drying. While this spreading was not as drastic as it was on silver surfaces, this was still a statistically significant change in spot size. This was primarily attributed to the high hygroscopicity of

choline chloride, which made the solute very hydrophilic; this can be verified in the future by using droplets of solutions incorporating other hygroscopic solutes to see if the same results manifest. Droplets of hydrophilic solutions tended to spread out further than hydrophobic solutions on the same substrate.

Table 9: 2-tailed t-tests for simulant and choline chloride stains

Substrate	***Simulant*** *(p value)*	***Choline chloride*** *(p value)*
Nylon	0.9	**0.05**
Non-percolated chemically-grown silver	--	**0.03**
Percolated chemically-grown silver	**0.03**	0.1
Percolated thermally-grown silver	**0.001**	**0.04**

The percolated thermally-grown substrates used for this experiment were not stored in argon-flushed containers, as the substrates from previous sections were. These silver substrates were exposed to air before and after the deposition of phenylalanine, choline chloride, and simulant fluid. It may be for this reason that the drastic spreading observed was so much greater than any stain from the previous sections, including the simulant stain on percolated thermally-grown silver, which should have had the same wettability. It is therefore hypothesized that the exposure to air permitted oxidation of the surface, which may have bolstered the wettability of the surface.[27] A follow-up experiment determining the effect of oxidation on wettability of these silver substrates is warranted.

Based on the findings by Dai et al.,[49] the significant spreading of choline chloride-containing solutions may have to do with ambient humidity. In their study, Dai et al. found that only under high-humidity conditions would sulfuric acid spread significantly on aluminum, since the humidity caused the corrosion product $Al_2(SO_4)_3$ to dissolve and increase the wettability of the surface. For this study, high-humidity environments were not prepared, and prominent spreading was only observed for choline chloride. Since choline chloride is extremely hygroscopic, the spreading effect could result from choline pulling in moisture, making the atmosphere around precipitated silver chloride very humid, enough so to dissolve the product. The spreading of choline chloride on non-percolated chemically-grown silver was monitored over time, as shown in Figure 41. A point of future studies will be to continue sampling points for this curve, and determining after how many hours the choline chloride droplet ceases to spread across the surface.

To discern if the interaction between choline chloride and silver is truly chemical, these stains should be evaluated with the methods used by Dai et al.,[49] particularly infrared reflection absorption spectroscopy (IRAS). This group used IRAS to identify products from corrosion of the metallic surface; this technique could be used with stains from this study to detect the ions that would result from reaction between the surface and liquid, and subsequent dissolving of the silver chloride precipitate. Further, since simulant stains did not spread as far as choline chloride stains on silver, the presence of other solutes may somehow act to screen the spreading effect; adding more solutes to the simulant in a future study could asses the validity of this claim.

4.6 Comparing semen spectra to previous studies

One of the goals of these experiments is to explore the findings of a previous study in this lab, conducted by Burleson,[16] who demonstrated a difference in Raman spectra for the same semen sample collected at different locations on the same SERS-active swab (see Figure 7). Once semen samples were prepared and their SERS spectra were collected, each spectrum was compared to the four spectra from Figure 7. The square of the residuals (difference in counts at each Raman shift) was calculated in Excel for each comparison of spectra, and the combination of spectra giving the smallest sum of square of residuals was deemed the closest match. The sums of squares of residuals were also calculated for all possible pairings of the spectra in Figure 7 to show the variation between those spectra was smaller than the variation between the spectra from that study and the closest matches from the current study (see Appendix section A.4). The expectation was that spectra that agree the most, or have the smallest sum of squares of residuals, should have similar component concentrations within the Raman collection volume, whether they were deposited on the AgNP-coated nylon swab or the AgNP-coated nylon sheet. Figures 42 and 43 below gives a qualitative comparison of the closes matches between spectra collected in this study and those from the previous study, based on the aforementioned calculations of sums of squares of residuals.

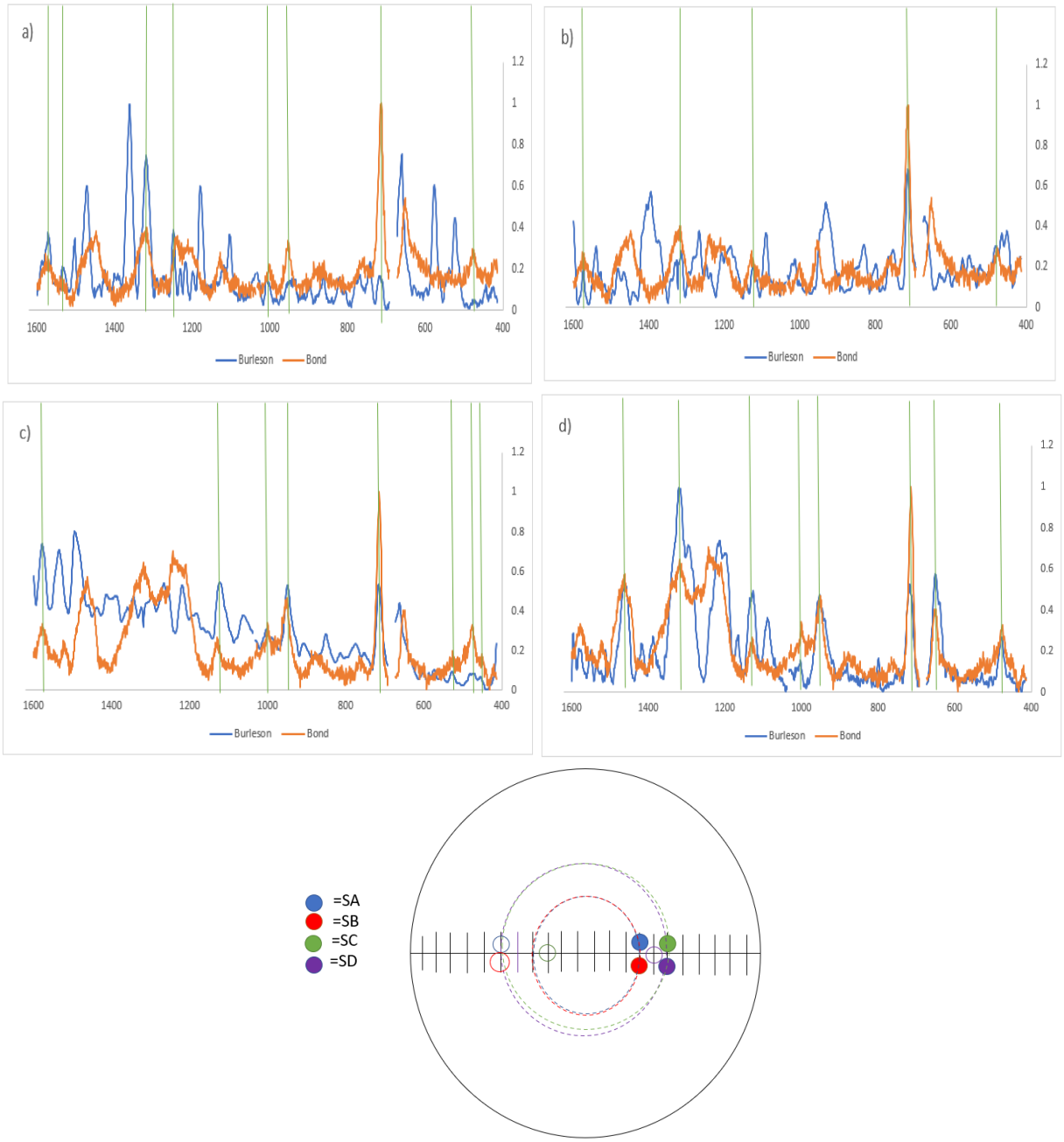

Figure 42: Comparisons between SERS semen spectra taken in a previous study (blue) in our lab to SERS semen spectra taken in this study (orange). a-d) comparisons of the closest matches between the spectra from Figure 7 and four spectra collected on non-percolated silver from this study; here a, b, c, d refer to Figure 7 a, b, c, d, respectively. e) approximate location of the spectra from the previous study in terms of semen stains collected on non-percolated silver layers during this study. Tick marks are positioned at 400 μm intervals. Solid circles=locations of spectra from this study most similar to those from the previous study. Dashed circles = hypothesized coffee rings of solutes captured in the spectra from the previous study. Empty circles = location of spectra from this study with next highest similarity to those from the previous study.

Figure 43: Comparisons between SERS semen spectra taken in a previous study (blue) in our lab to SERS semen spectra taken in this study (orange). a-d) comparisons of the closest matches between the spectra from Figure 7 and four spectra collected on percolated silver from this study; here a, b, c, d refer to Figure 7 a, b, c, d, respectively. e) approximate location of the spectra from the previous study in terms of semen stains collected on percolated silver layers during this study. Tick marks are positioned at 400 μm intervals. Solid circles=locations of spectra from this study most similar to those from the previous study. Dashed circles = hypothesized coffee rings of solutes captured in the spectra from the previous study. Empty circles = location of spectra from this study with next highest similarity to those from the previous study.

Because of the similarities between the blue and orange spectra in panels a-d of Figure 42 and 43, each blue spectrum was assigned the position of its respective orange spectrum collected during this study. These positions on both the non-percolated silver and percolated silver substrates are given in the circular graphic in Figures 42 and 43. Most of the spectra from Figure 7 had noteworthy overlap with spectra collected about 1200-2000 μm away from the center of either stain. The only exception seems to be on the semen stain formed on percolated silver; Figure 7d overlapped the most with the spectrum at the rightmost position sampled in this stain. Notably, the Figure 7 spectra were assigned similar positions on both substrates except for Figure 7d. Also, the principal matches between Burleson's data and semen SERS spectra from this study were always to one side of the droplet. This preferential adherence to one side over the other was seen in the simulant stains on silver. Given how all stains were prepared in controlled environments to ensure even spreading of the droplets, this is worth future investigation to see if more measures could have been taken to avoid this.

If the coffee-ring hypothesis were correct, then the Raman spectra from Figure 7 should theoretically be found at any location along their respective dashed circles in Figures 42 and 43. For example, the solutes should separate upon drying such that the Raman spectrum closest to Figure 7a, located at the solid blue circle in Figures 42 and 43, should be reproduced at any location along the dashed blue circle. Since a line scan was taken along the diameter of the semen stains, this means the spectrum closest to Figure 7a should resemble the spectrum taken 2400 μm from the left edge of the semen stain on non-percolated silver, since this position is equidistant from the center of the stain. To test this, the spectra with the second-highest degree of overlap with Figure 7 spectra, or the spectra with the second-lowest sums of squares of residuals,

were plotted in Figures 42 and 43 using open circles. Since these spectra have the next-closest similarity to the Figure 7 spectra, they should land on or near these proposed coffee rings.

While none of the second-closest matches had locations on any of their respective coffee rings, the second-closest matches to the spectra of Figure 7a-c did land within 600 microns of the expected rings. The spectra associated with Figure 7d belonged to very different locations along their respective stains; the closest match on the non-percolated substrate was found to be more interior to the stain, while the closest match on the percolated substrate was found at the edge. Given that the evidence reported earlier seems to indicate minimal component separation across the stain, the lack of clear matches in specific locations is perhaps not that surprising.

Interestingly, the separation of theoretical coffee rings seems to corroborate the findings of contact angle hysteresis calculations from Section 4.2. According to these calculations for chemically-grown silver, the percolated substrate had a smaller hysteresis value, making it more hydrophilic and allowing for more well-defined coffee ring formation. From Figures 42 and 43, the fact that theoretical coffee rings overlapped on the non-percolated substrate, and such overlap is absent on the percolated substrate suggests the percolated substrate is more wettable, as the hysteresis calculations show.

To further investigate the matching of previous spectra of semen to those collected in this study, PCA analysis was conducted in which the Burleson data was added into the semen spectra collected on non-percolated and percolated chemically-grown substrates, as these are the substrates that most closely match the swabs used in the Burleson study. The results of this analysis are shown in Figures 44 and 45. In each case, the PCA results were used to calculate Euclidean distances between spectra, which are presented as a heat map in Panel B. For the non-

percolated silver film, (cf. Figure 44), the data presented in Panel B indicates that Burleson spectra A & B are reasonably similar to most of the spectra within the contact line of the droplet, while C & D are not. The data presented in Figure 45 (percolated silver substrate) indicates that only Burleson spectrum B is similar to any of the data collected across the percolated substrate. This may indicate that the swab fabrication protocol developed by Burleson tends to produce non-percolated swab fibers. On the other hand, qualitative comparison of Panel B of Figures 44 and 45 seems to indicate a stronger match between Burleson spectrum B and the spectra collected within the boundaries of the droplet contact line.

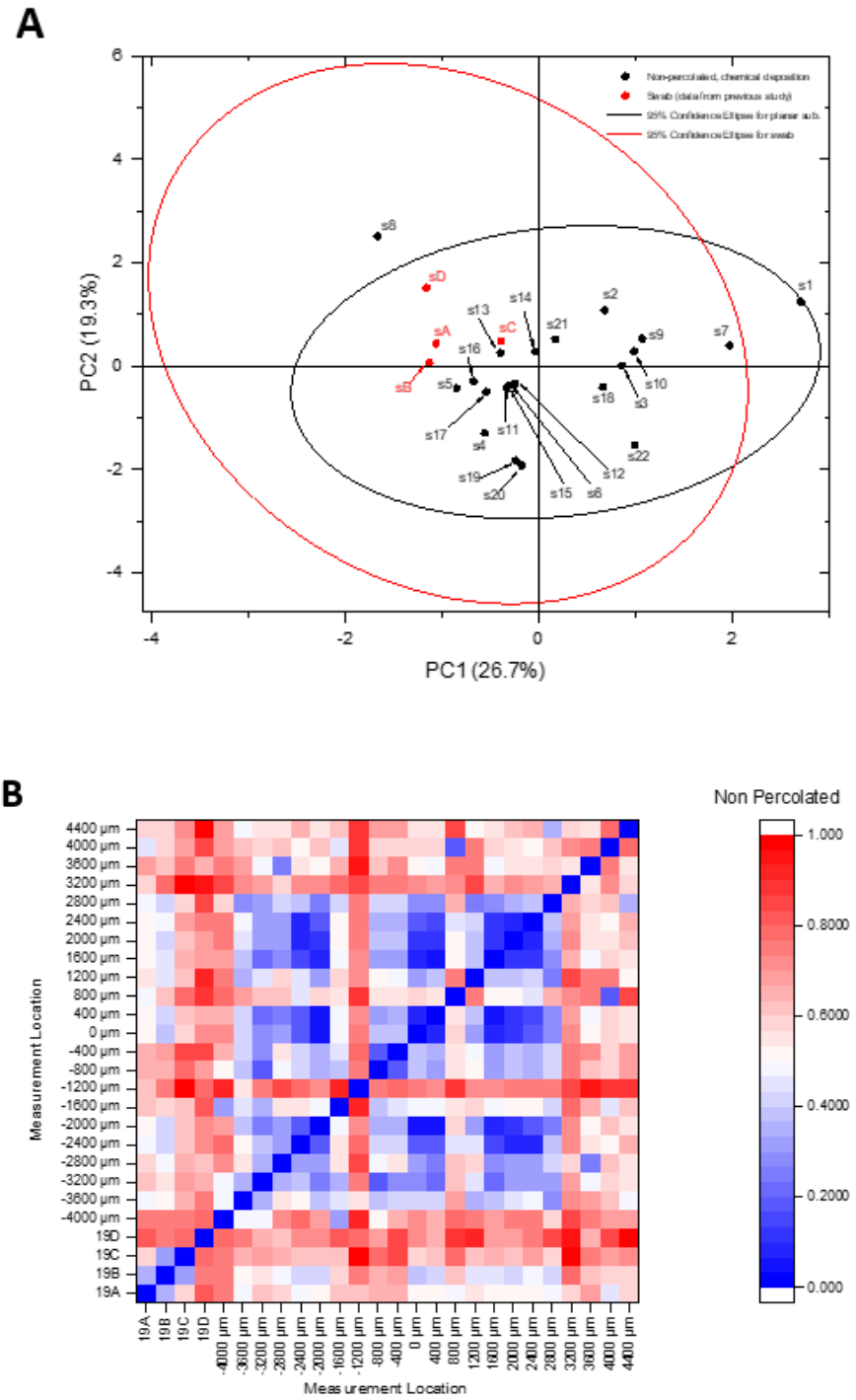

Figure 44: Principal component analysis (6 principal components accounted for 83% of variation) of semen spectra on non-percolated, chemically-grown substrates compared to spectra collected by Burleson on SERS active swabs. A score plot is shown in Panel A while heat map indicating Euclidean distances between spectra is shown in Panel B. The left edge of the stain is indicated as s1 or -4000 microns while the right edge is indicated as s21 or +4400 microns in the two panels. Burleson spectra are indicated as sA – sD.

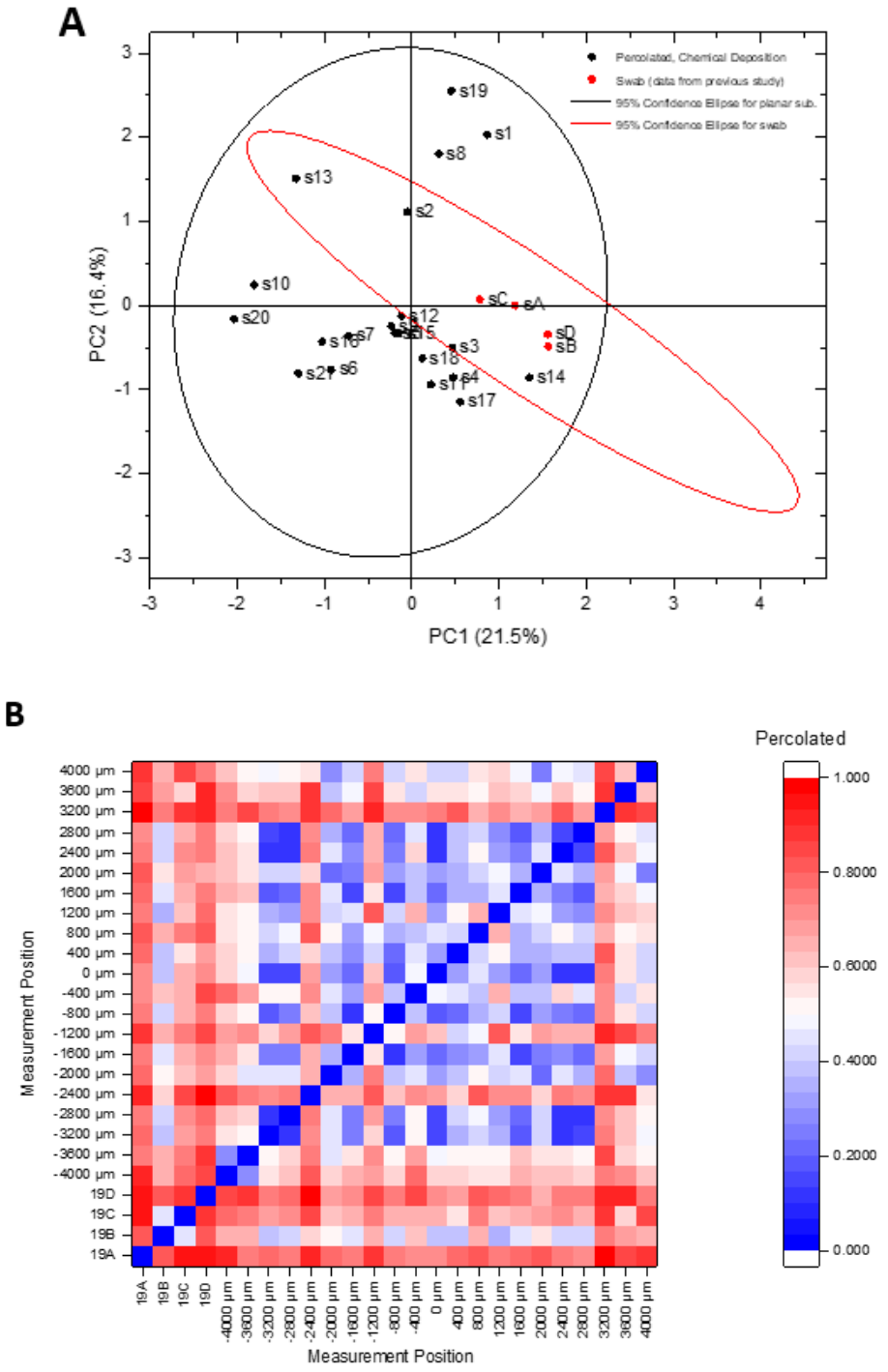

Figure 45: Principal component analysis (8 principal components accounted for 79% of variation) of semen spectra on percolated, chemically-grown substrates compared to spectra collected by Burleson on SERS active swabs. A score plot is shown in Panel A while heat map indicating Euclidean distances between spectra is shown in Panel B. The left edge of the stain is indicated as s1 or -4000 microns while the right edge is indicated as s21 or +4000 microns in the two panels. Burleson spectra are indicated as sA – sD.

The ability to assign spectra from a previous study to those obtained for the current study is valuable, as it demonstrates association between SERS spectra taken on substrates of similar makeup but starkly different topologies. As such, these associations demonstrate how the use of flat nylon sheets as initial substrates does in fact provide useful information that can be translated to future studies of spectral acquisition from bodily fluids prepared on AgNP-coated swab substrates.

CHAPTER 5: CONCLUSIONS AND FUTURE DIRECTIONS

The results from previous analysis in our lab were compared to SERS line scans from this study, and some of the spectra taken previously were correlated with spectra from these line scans. Because the nature of the previous study was to show SERS spectra from AgNP-coated swabs, no mention was made of the location along a swab where each spectrum was acquired. Because of the spacing and orientations of the swabs, AgNP deposition on nylon sheets was used instead; the results of this study showed SERS enhancement was still accessible and observations of fundamental interactions between semen and silver were possible.

This project also laid the foundation for a rigorous study in the percolation thresholds for silver on nylon, prepared by two different methodologies. So far the conductivity of silver experiences a significant increase when either chemically grown for approximately 61 minutes, or thermally deposited to a thickness of 15 nm. At the time of this study, no methods were utilized to assess the true thickness of these layers and the spatial layout of these percolating silver islands. It is recommended that this study is followed up with SEM data to yield more exact data. Further, gaps in the tables presented in the Appendix should be filled to confirm the findings from the previous chapter.

Similarly, contact angle hysteresis data was collected by manually rotating the stage; conventionally, this process is automated to ensure constant rotation. These results should then be considered preliminary as well, and ideally be followed up with a device that can ensure steady rotation. However, it is anticipated that those results should be in agreement with those exhibited here. That is, silver layers that were prepared chemically were consistently more

wettable than those prepared thermally; this resulted in having more wettable AgNP-coated nylon when prepared chemically.

This study demonstrated preliminary, but promising, results of the nature of semen stain formation on AgNP-coated nylon substrates. The original hypothesis was that urea, phenylalanine, and choline were going to form concentric coffee rings in that respective order of increasing radius on every stain. While some subtle differences were indicated, this preliminary study suggests that the separation of solutes may not happen in such an 'orderly' way. On bare nylon, choline was found in the middle of the stain, aligning with the findings of Filik et al.[31] On surfaces coated with silver, choline appeared to spread past the original pinned contact line of the droplet, where urea and phenylalanine were deposited. The findings from this study suggest a reactive spreading of choline along the surface of AgNP-coated substrates.

All of the Raman line scans on simulant and semen stains presented were conducted on a total of seven stains, each of which featured a unique combination of sample and substrate. As such, no duplicate trials were collected; this is the first step that needs to be taken going forward. It needs to be confirmed that no part of these results were a product of random variation. That being said, these results provide evidence that the vibrational mode of choline at 715 cm^{-1} is drastically enhanced. Further, the repetitive spreading of choline past the contact line of each stain on silver shows some sort of interaction is occurring between the substrate and choline. Based on similar processes reported in the literature, this was attributed to reactive spreading of choline chloride on silver; a follow-up study determining the presence of the expected silver chloride product from said reaction should be undertaken to confirm this.

Overall, every silver-coated substrate exhibits an expansion of choline, as well as other components, past the contact line of their respective stain, indicated by a discoloration of the silver. Since choline is unique to semen compared to other bodily fluids typically found in sexual assault kits,[5,16] is easily detectable in Raman spectra, and is not limited to the center of the stain where highly-soluble solutes tend to aggregate in complex stains, the choline marker should be used as an overall marker for the presence of semen on silver. This may be especially useful in a study of bodily fluid mixtures where semen could be clearly identified by this mode.

In the future, a new semen simulant should be prepared that incorporates more semen solutes. This will not only give more realistic trends in relative placement of coffee rings, but this will also help capture other properties of semen that the ternary simulant in this study was not able to show. Perhaps most importantly, steps should be taken to approximate the viscosity of semen in the simulant. This should be done by incorporating enough albumin into the mixture to allow the viscosity to match the literature value of 3 cP.[38] Since the spread of choline past stain contact lines was not as drastic in semen as it was for the simulant, adding more solutes is expected to aid in mimicking the choline spreading seen in semen stains. The presence of other solutes may somehow act to screen the spreading effect; adding more solutes to the simulant could asses the validity of this claim.

CHAPTER 6: REFERENCES

1. Quinlan, A. Visions of public safety, justice, and healing: The making of the rape kit backlog in the United States, *Social and Legal Studies*, **2019**, *29*, 225-245.

2. Bell, S. Forensic Chemistry, Second. Jaworski, A., Zalesky, J., Eds.; Pearson Prentice Hall: Upper Saddle River, 2013.

3. Virkler, K.; Lednev, I. K. Analysis of body fluids for forensic purposes: From laboratory testing to non-destructive rapid confirmatory identification at a crime scene, *Forensic Sci. Int.*, **2009**, *188*, 1-17. advances in colloid and interface science acs abbreviation

4. Lehrer, S.; Terk, M.; Piccoli, S. P.; Song, H. K.; Lavagnini, P.; Luderer, A. A. Reverse transcriptase-polymerase chain reaction for prostate-specific antigen may be a prognostic indicator in breast cancer, *Br. J. Cancer*, **1996**, *74*, 871-873.

5. Virkler, K.; Lednev, I. K. Raman spectroscopic signature of semen and its potential application to forensic body fluid identification, *Forensic Sci. Int.*, **2009**, *193*, 56-62.

6. Granger, II, R. M.; Yochum, H. M.; Granger, J. N.; Sienerth, K. D. *Instrumental Analysis*, First. (revised),; Oxford University Press: New York, 2017.

7. Muro, C. K.; Doty, K. C.; de Souza Fernandes, L.; Lednev, I. K. Forensic body fluid identification and differentiation by Raman spectroscopy, *Forensic Chem.*, **2016**, *1*, 31-38.

8. Fikiet, M. A.; Lednev, I. K. Raman spectroscopic method for semen identification: Azoospermia, *Talanta*, **2019**, *194*, 385-389.

9. Muro, C. K.; Lednev, I. K. Race differentiation based on Raman spectroscopy of semen traces for forensic purposes, *Anal. Chem.*, **2017**, *89*, 4344-4348.

10. Tilley, R. Colour and the Optical Properties of Materials, Second. John Wiley and Sons: West Sussex, 2011.

11. Daniels, J. K.; Chumanov, G. Nanoparticle-mirror sandwich substrates for surface-enhanced Raman scattering, *J. Phys. Chem. B*, **2005**, *109*, 17936-17942.

12. Sharma, B.; Frontiera, R. R.; Henry, A.I.; Ringe, E.; Van Duyne, R. P. SERS: Materials, applications, and the future, *Mater. Today*, **2012**, *15*, 16-25.

13. Evanoff, Jr., D. D; Chumanov, G. Synthesis and optical properties of silver nanoparticles and arrays, *Chem. Phys. Chem*., **2005**, *6*, 1221–1231.

14. Kneipp, K.; Wang, Y.; Kneipp, H.; Perelman, L. T.; Itzkan, I.; Dasari, R. R.; Feld, M. S. Single molecule detection using surface-enhanced Raman scattering (SERS), *Phys. Rev. Lett.*, **1997**, *78*, 1667-1670.

15. Nie, S.; Emory, S. R. Probing single molecules and single nanoparticles by surface-enhanced Raman scattering, *Science*, **1997**, *275*, 1102-1106.

16. Burleson, M. D. SERS-active nylon fiber evidence swabs for forensic applications. Master's Thesis, Western Carolina University, Cullowhee, NC, 2016.

17. Evanoff, Jr., D. D. Development of SERS-active forensic evidence swabs for rapid, non-destructive confirmatory serological screening and STR typing of human bodily fluids,

National Institutes of Justice, Research and Development in Forensic Science for Criminal Justice Purposes, 2019, Grant 2015-NE-BX-K003.

18. Oates, T. W. H.; Ryves, L.; Bilek, M. M. M.; McKenzie, D. R. Accurate determination of optical and electronic properties of ultra-thin silver films for biosensor applications, *Sensor. Actuat. B*, **2005**, *109*, 146-152.

19. Kreibig, U.; Vollmer, M. Optical Properties of Metal Clusters, Springer Series in Materials Science, 25. Springer: Germany, 1995.

20. Brouers, F.; Blacher, S.; Lagarkov, A. N.; Sarychev, A. K.; Gadenne, P.; Shalaev, V. M. Theory of giant Raman scattering from semicontinuous metal films, *Phys. Rev. B*, **1997**, *55*, 234-245.

21. Gadenne, P.; Gagnot, D.; Masson, M. Surface enhanced resonant Raman scattering induced by silver thin films close to the percolation threshold, *Physica A*, **1997**, *241*, 161-165.

22. Enders, D.; Nagao, T.; Pucci, A.; Nakayama, T.; Aono, M. Surface-enhanced ATR-IR spectroscopy with interface-grown plasmonic gold-islands films near the percolation threshold, *Phys. Chem. Chem. Phys.*, **2011**, *13*, 4935-4941.

23. Sefiane, K. Patterns from drying drops, *Adv. Colloid. Interfac.*, **2014**, *206*, 372-381.

24. Deegan, R. D.; Bakajin, O.; Dupont, T. F.; Huber, G.; Nagel, S. R.; Witten, T. A. Capillary flow as the cause of ring stains from dried liquid drops, *Nature*, **1997**, *389*, 827-829.

25. Uno, K.; Hayashi, K.; Hayashi, T.; Ito, K.; Kitano, H. Particle adsorption in evaporating droplets of polymer latex dispersions on hydrophilic and hydrophobic substrates; *Colloid. Polym. Sci.*, **1998**, *276*, 810-815.

26. Chen, R.; Zhang, L.; Zang, D.; Shen, W. Wetting and drying of colloidal droplets: Physics and pattern formation, In *Advances in Colloid Science*, Rahman, M.; Asiri, A. M., Eds.; InTech: Rijeka, Croatia, 2016; 3-25.

27. Osman, M. A.; Keller, B. A. Wettability of native silver surfaces, *Appl. Surf. Sci.*, **1996**, *99*, 261-263.

28. Kumar, G.; Prabhu, K. N. Review of non-reative and reactive wetting of liquids on surfaces, *Adv. Colloid. Interfac.*, **2007**, *133*, 61-89.

29. Giovambattista, N.; Debenedetti, P. G.; Rossky, P. J. Effect of surface polarity on water contact angle and interfacial hydration structure, *J. Phys. Chem. B*, **2007**, *111*, 9581-9587.

30. Wong, T. S.; Chen, T. H.; Shen, X. S.; Ho, C. M. Nanochromatography driven by the coffee ring effect, *Anal. Chem.*, **2011**, *83*, 1871-1873.

31. Filik, J.; Stone, N. Analysis of human tear fluid by Raman spectroscopy, *Anal. Chim. Acta*, **2008**, *616*, 177-184.

32. Cameron, J. M.; Butler, H. J.; Palmer, D. S.; Baker, M. J. Biofluid spectroscopic disease diagnostics: A review on the processes and spectral impact of drying, *J. Biophotonics*, **2018**, *11*, 1-12.

33. Schürmann, U.; Takele, H.; Zaporojtchenko, V.; Faupel, F. Optical and electrical properties of polymer metal nanocomposites prepared by magnetron co-sputtering, *Thin Solid Films*, **2006**, *515*, 801-804.

34. Lam, C. N. C.; Wu, R.; Li, D.; Hair, M. L.; Neumann, A. W. Study of the advancing and receding contact angles: Liquid sorption as a cause of contact angle hysteresis, *Adv. Colloid. Interfac.*, **2002**, *96*, 169-191.

35. Eral, H. B.; 't Mannetje, D. J. C. M.; Oh, J. M. Contact angle hysteresis: A review of fundamentals and applications. *Colloid. Polym. Sci.*, **2013**, *291*, 247–260.

36. Mampallil, D.; Eral, H. B. A review on suppression and utilization of the coffee-ring effect, *Adv. Colloid. Interfac.*, **2018**, *252*, 38-54.

37. Krasovitski, B.; Marmur, A. Drops down the hill: Theoretical study of limiting contact angles and the hysteresis range on a tilted plane, *Langmuir*, **2005**, *21*, 3881-3885.

38. Owen, D. H.; Katz, D. F. A review of the physical and chemical properties of human semen and the formulation of a semen simulant, *J. Androl.*, **2005**, *26*, 459-469.

39. Gupta, A.; Mahdi, A. A.; Ahmad, M. K.; Shukla, K. K.; Jaiswer, S. P.; Shankhwar, S. N. ^{1}H-NMR spectroscopic studies on human seminal plasma: A probative discriminant function analysis classification model, *J. Pharmaceut. Biomed.*, **2011**, *54*, 106-113.

40: Sharma, U.; Chaudhury, K.; Jagannathan, N. R.; Guha, S. K. A proton NMR study of the effect of a new intravasal injectable male contraceptive RISUG on seminal plasma metabolites, *Reprod.*, **2001**, *122*, 431-436.

41. Frost, R. L.; Kristof, J.; Rintoul, L.; Kloprogge, J. T. Raman spectroscopy of urea and urea-intercalated kaolinites at 77 K, *Spectrochim. Acta A*, **2000**, *56*, 1681-1691.

42. Jeffers, R. B.; Cooper, J. B. FT-surface-enhanced Raman scattering of phenylalanine using silver-coated glass fiber filters, *Spectrosc. Lett.*, **2010**, *43*, 220-225.

43. Akutsu, H. Direct determination by Raman scattering of the conformation of the choline group in phospholipid bilayers, *Biochemistry*, **1981**, *20*, 7359-7366.

44. Mamunya, Y. P.; Davydenko, V. V.; Pissis, P.; Lebedev, E. V. Electrical and thermal conductivity of polymers filled with metal powders, *Eur. Polym. J.*, **2002**, *38*, 1887-1897.

45. Evanoff, Jr., D. D.; Chumanov, G. Size-controlled synthesis of nanoparticles. 1. "Silver-only" aqueous suspensions via hydrogen reduction, *J. Phys. Chem. B*, **2005**, *108*, 13948-13956.

46. Li, L; Li, L.; Chen, W. D.; Zheng, J.; Wang, L. W., Chen, Y. Characterization of silver nanoparticles thin films with various thicknesses by AFM, *Journal of Materials Science and Chemical Engineering*, **2016**, *4*, 34-39.

47. Stephens, J. S.; Chase, D. B.; Rabolt, J. F. Effect of the electrospinning process on polymer crystallization chain conformation in nylon-6 and nylon-12, *Macromolecules*, **2004**, *37*, 877-881.

48. Le Ru, E. C.; Blackie, E.; Meyer, M.; Etchegoin, P. G. Surface enhanced Raman scattering enhancement factors: A comprehensive study, *J. Phys. Chem. C*, **2007**, *111*, 13794-13803.

49. Dai, Q.; Hu, J.; Freedman, A.; Robinson, G. N.; Salmeron, M. Nanoscale imaging of a corrosion reaction: Sulfuric acid droplets on aluminum surfaces, *J. Phys. Chem.*, **1996**, *100*, 9-11.

APPENDIX

A.1 Representative simulant spectra

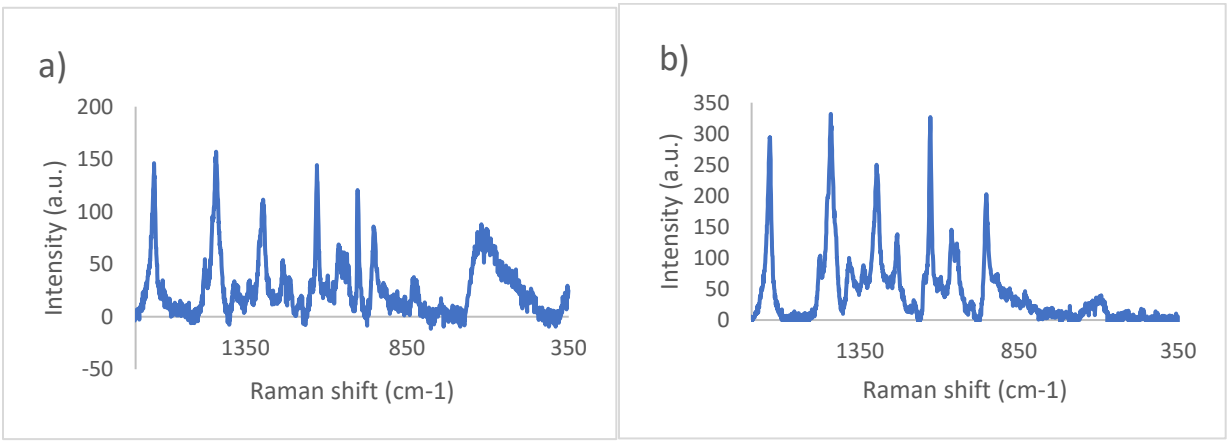

Figure A1: representative spectra of semen simulant on bare nylon. a) spectrum taken on left edge of stain, b) spectrum taken near center of the stain.

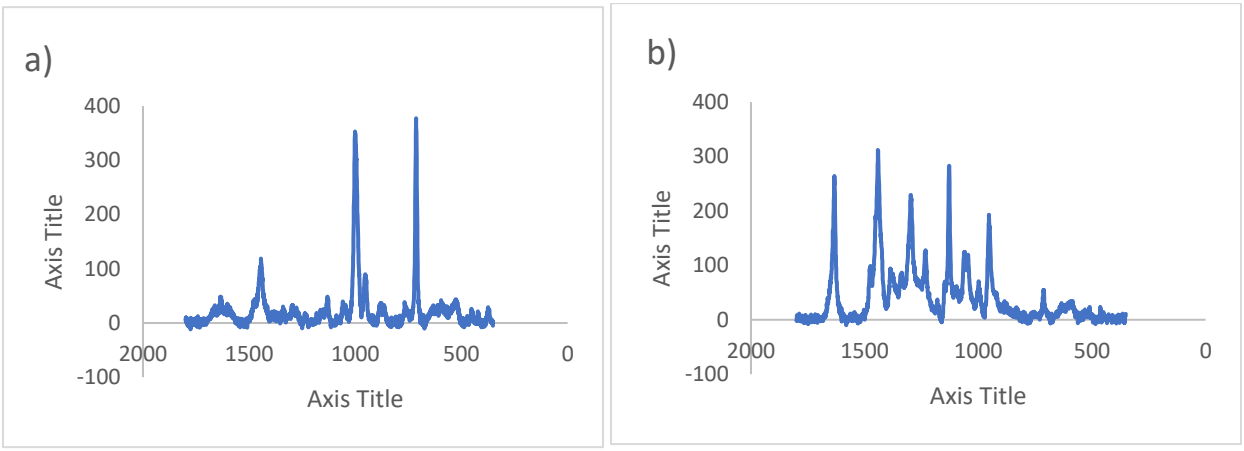

Figure A2: representative spectra of the edge of the semen simulant on bare nylon. a) spectrum taken on outside edge of coffee ring, b) spectrum taken at the inside edge of the ring.

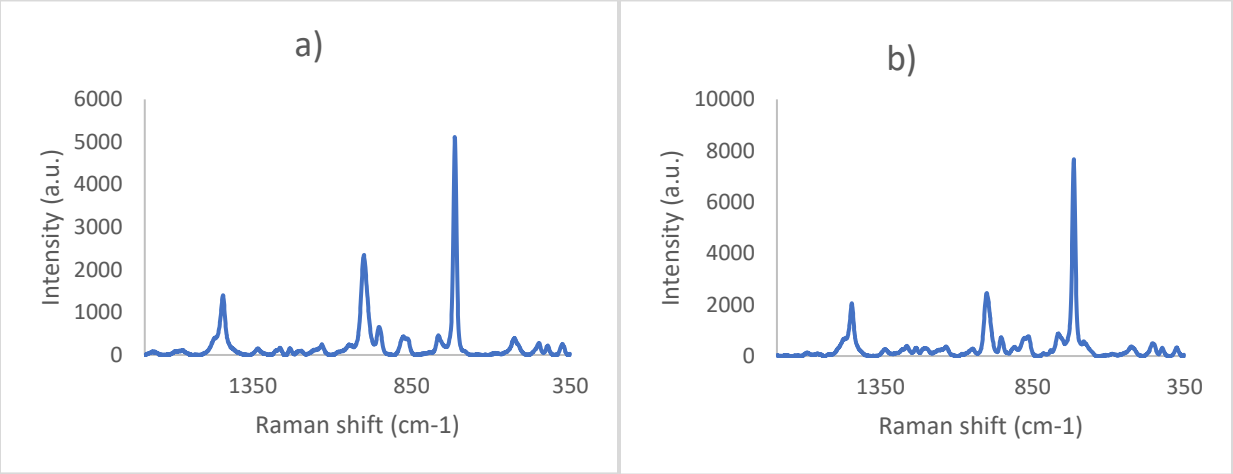

Figure A3: representative spectra of semen simulant on non-percolated thermally-grown silver. a) spectrum taken on left edge of stain, b) spectrum taken near center of the stain.

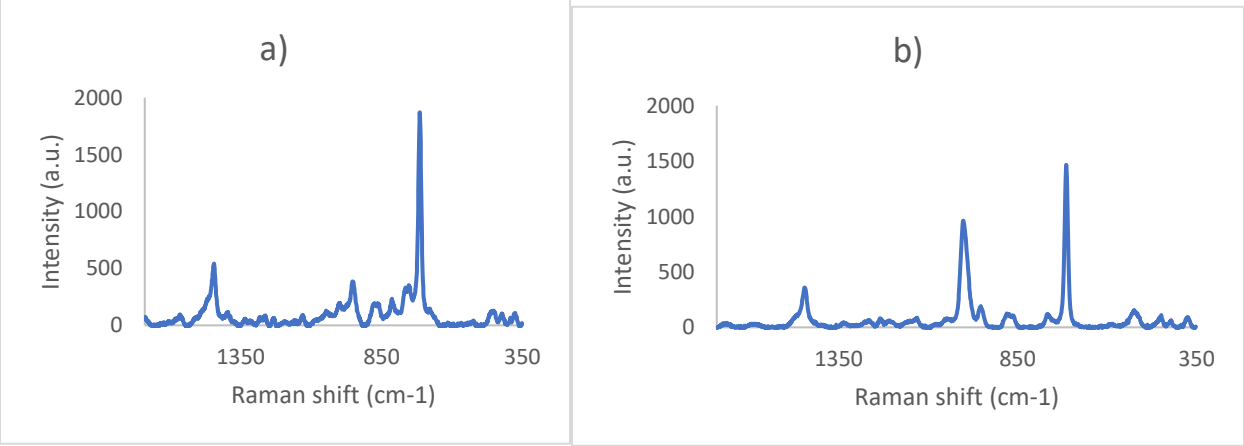

Figure A4: representative spectra of semen simulant on percolated thermally-grown silver. a) spectrum taken on left edge of stain, b) spectrum taken near center of the stain.

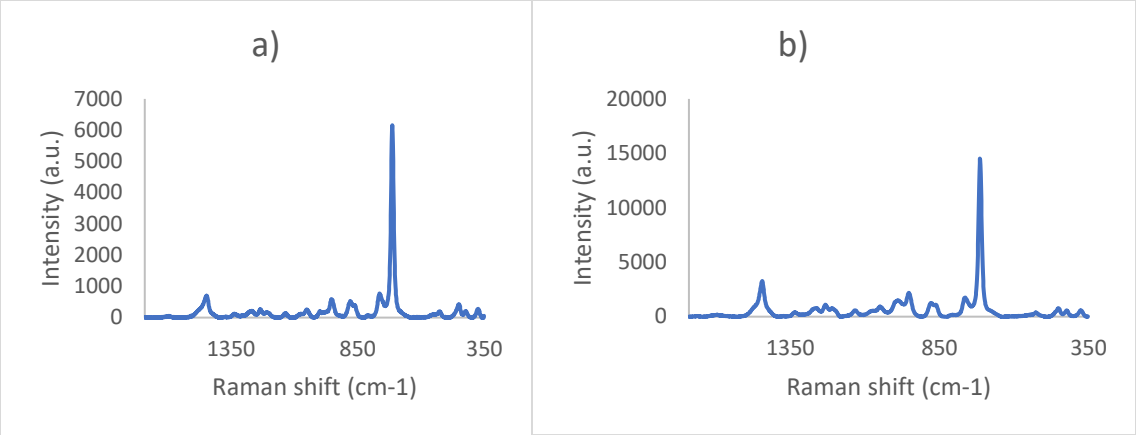

Figure A5: representative spectra of semen simulant on non-percolated chemically-grown silver. a) spectrum taken on left edge of stain, b) spectrum taken near center of the stain.

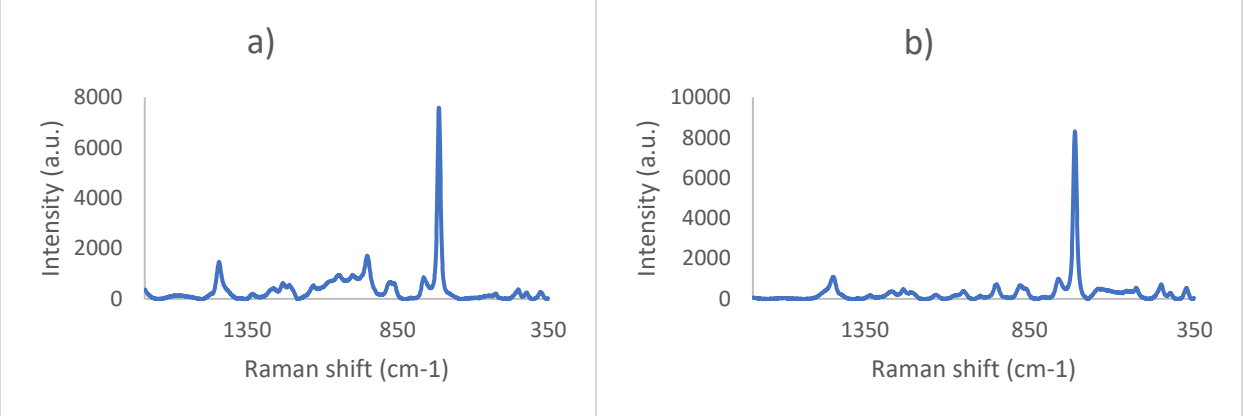

Figure A6: representative spectra of semen simulant on percolated chemically-grown silver. a) spectrum taken on left edge of stain, b) spectrum taken near center of the stain.

A.2 All semen spectra

A.2.1 Semen on non-percolated chemically-grown silver

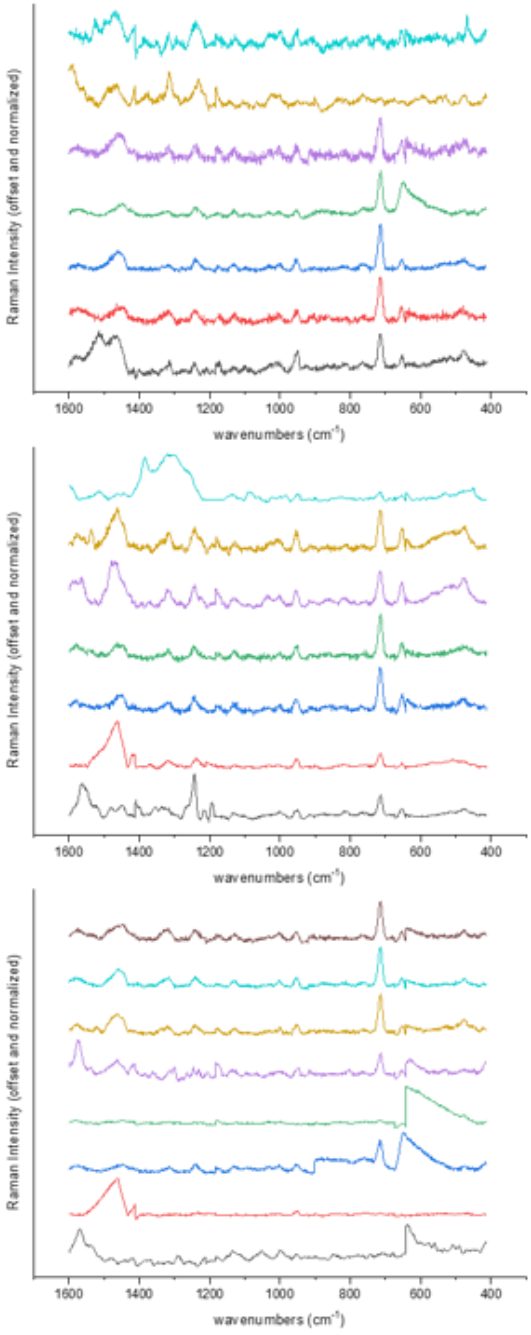

Figure A7: SERS scans taken along the diameter of a semen stain on non-percolated chemically-grown silver.

A.2.2 Semen on percolated chemically-grown silver

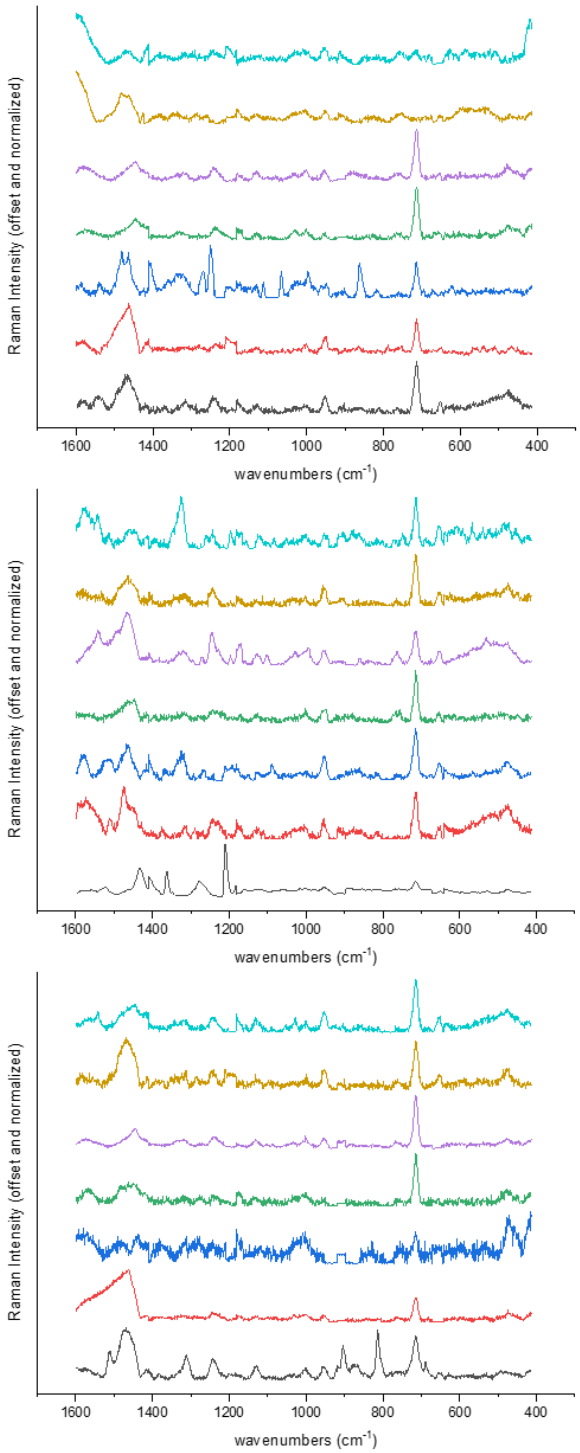

Figure A8: SERS scans taken along the diameter of a semen stain on percolated chemically-grown silver substrate. Within the three panels, spectra are ordered from left of stain (top) to right of stain (bottom)

A.3 Alternate fittings

A.3.1 Fitting simulant data to 713cm^{-1} mode

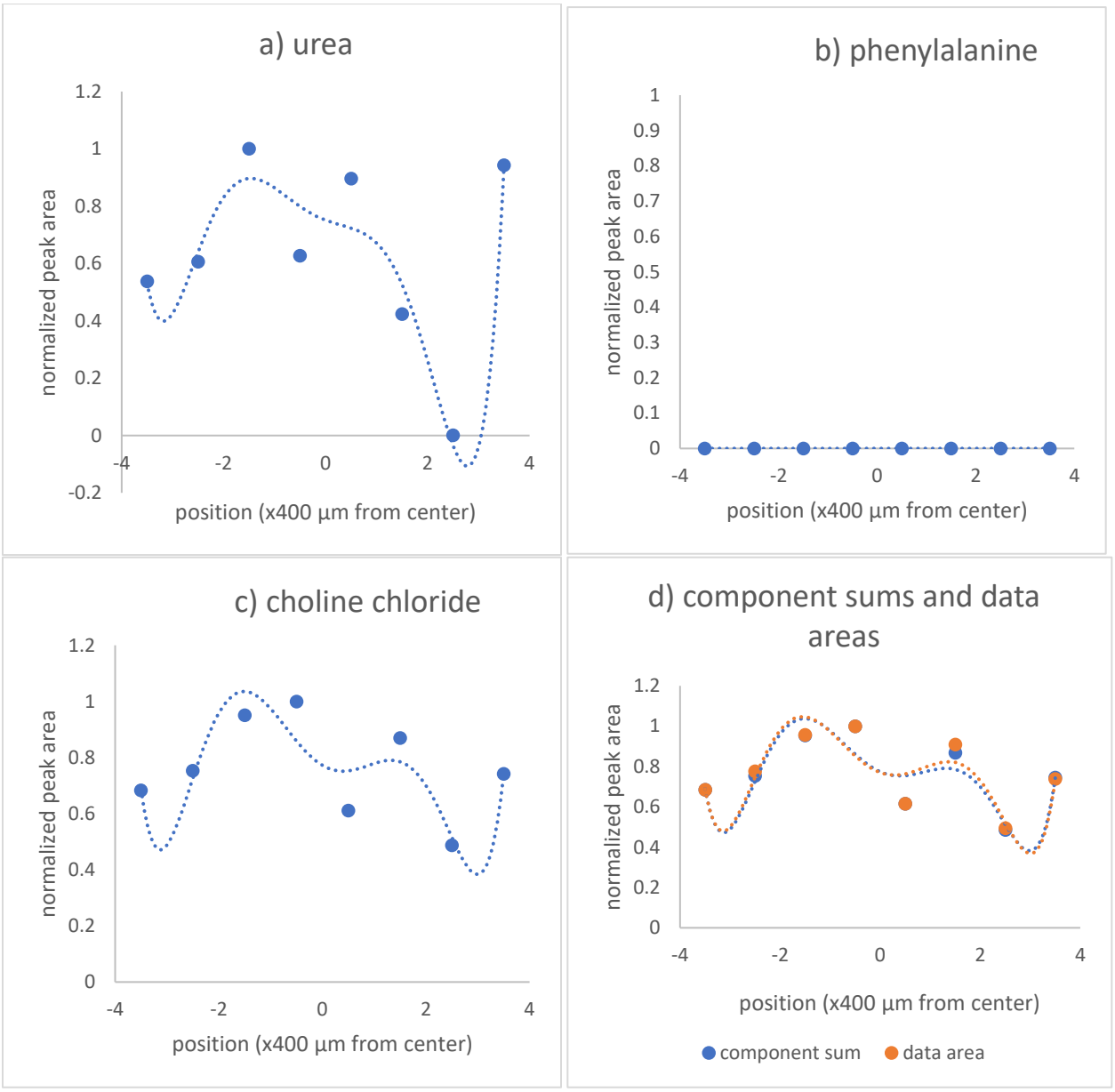

Figure A9: Peak areas of deconvoluted components of a) urea, b) phenylalanine, and c) choline chloride from the 713 cm^{-1} mode of simulant SERS spectra on non-percolated thermally-grown silver. In d), the sum of these components is given in blue, and the original data area is given in orange. All curves are sixth order polynomials.

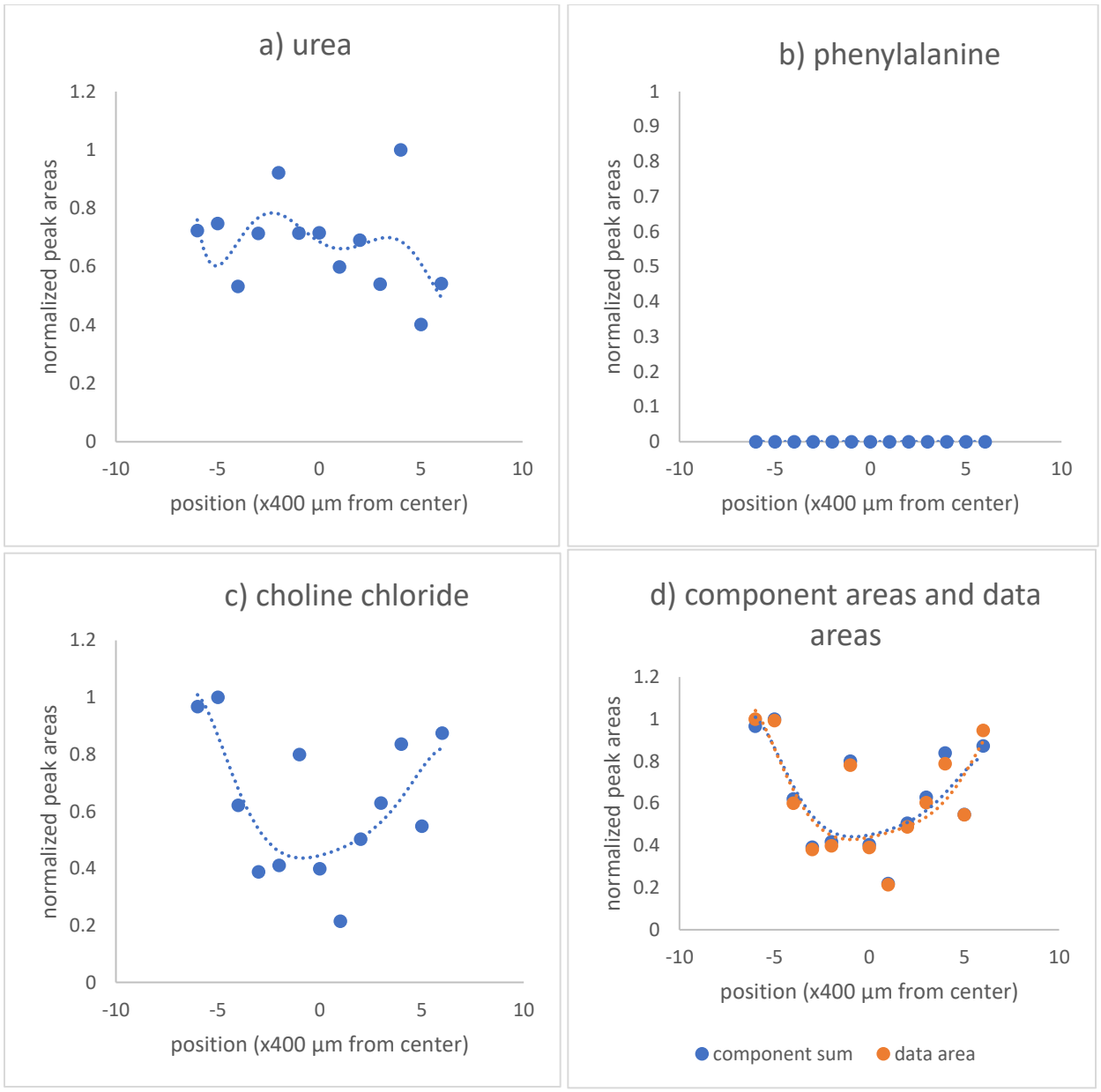

Figure A10: Peak areas of deconvoluted components of a) urea, b) phenylalanine, and c) choline chloride from the 713 cm^{-1} mode of simulant SERS spectra on percolated thermally-grown silver. In d), the sum of these components is given in blue, and the original data area is given in orange. All curves are sixth order polynomials.

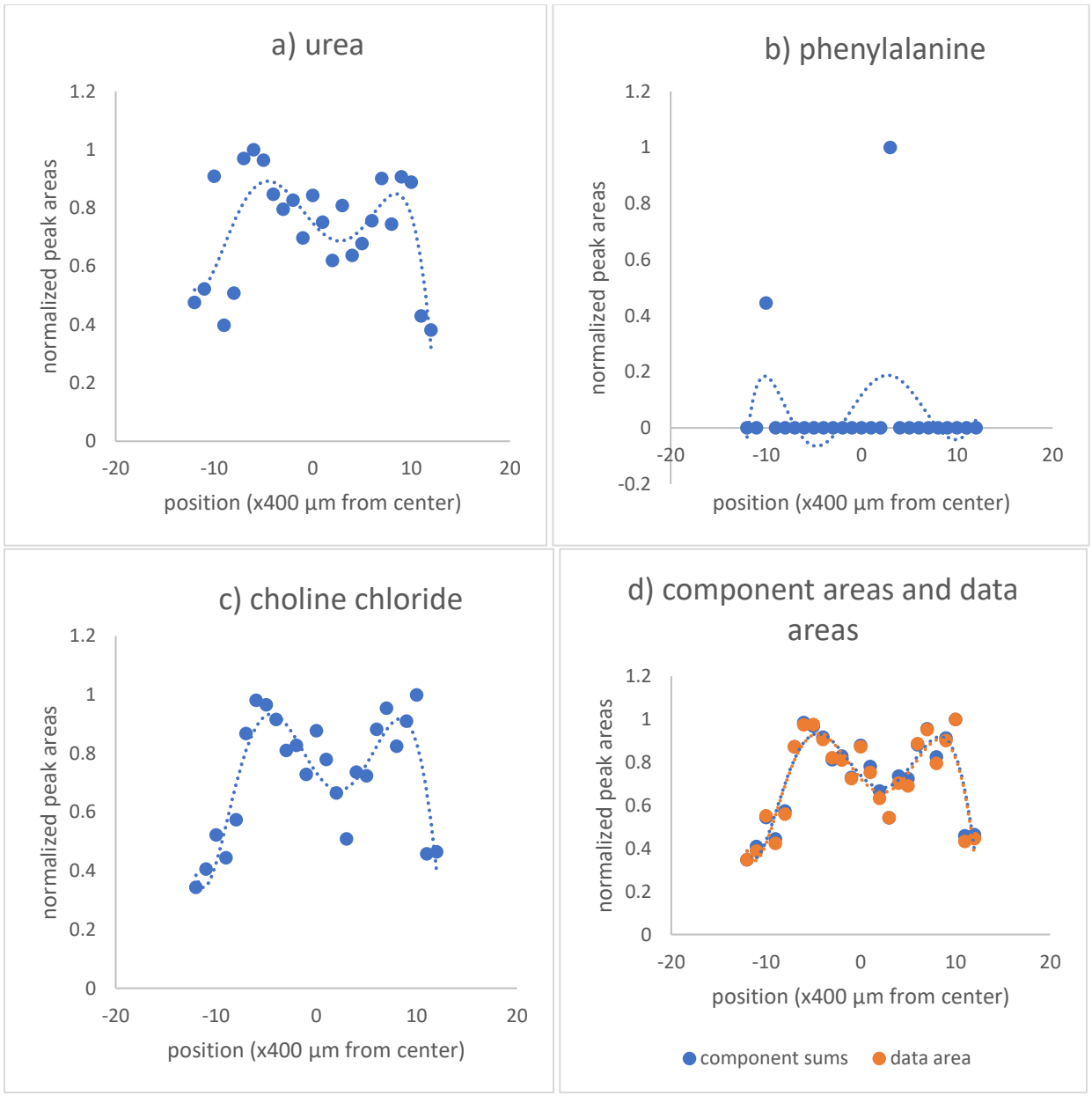

Figure A11: Peak areas of deconvoluted components of a) urea, b) phenylalanine, and c) choline chloride from the 713 cm^{-1} mode of simulant SERS spectra on non-percolated chemically-grown silver. In d), the sum of these components is given in blue, and the original data area is given in orange. All curves are sixth order polynomials.

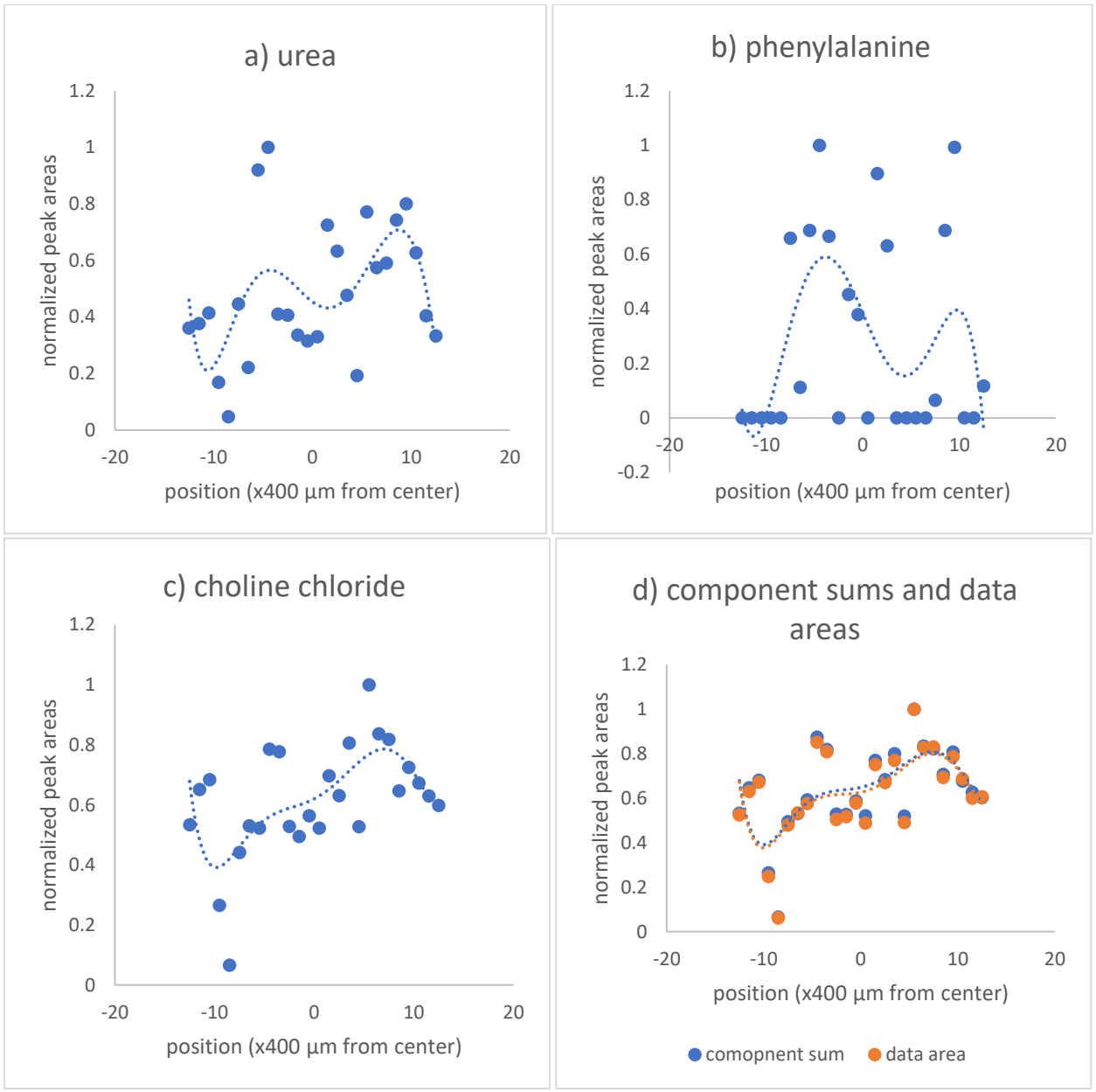

Figure A12: Peak areas of deconvoluted components of a) urea, b) phenylalanine, and c) choline chloride from the 713 cm^{-1} mode of simulant SERS spectra on percolated chemically-grown silver. In d), the sum of these components is given in blue, and the original data area is given in orange. All curves are sixth order polynomials.

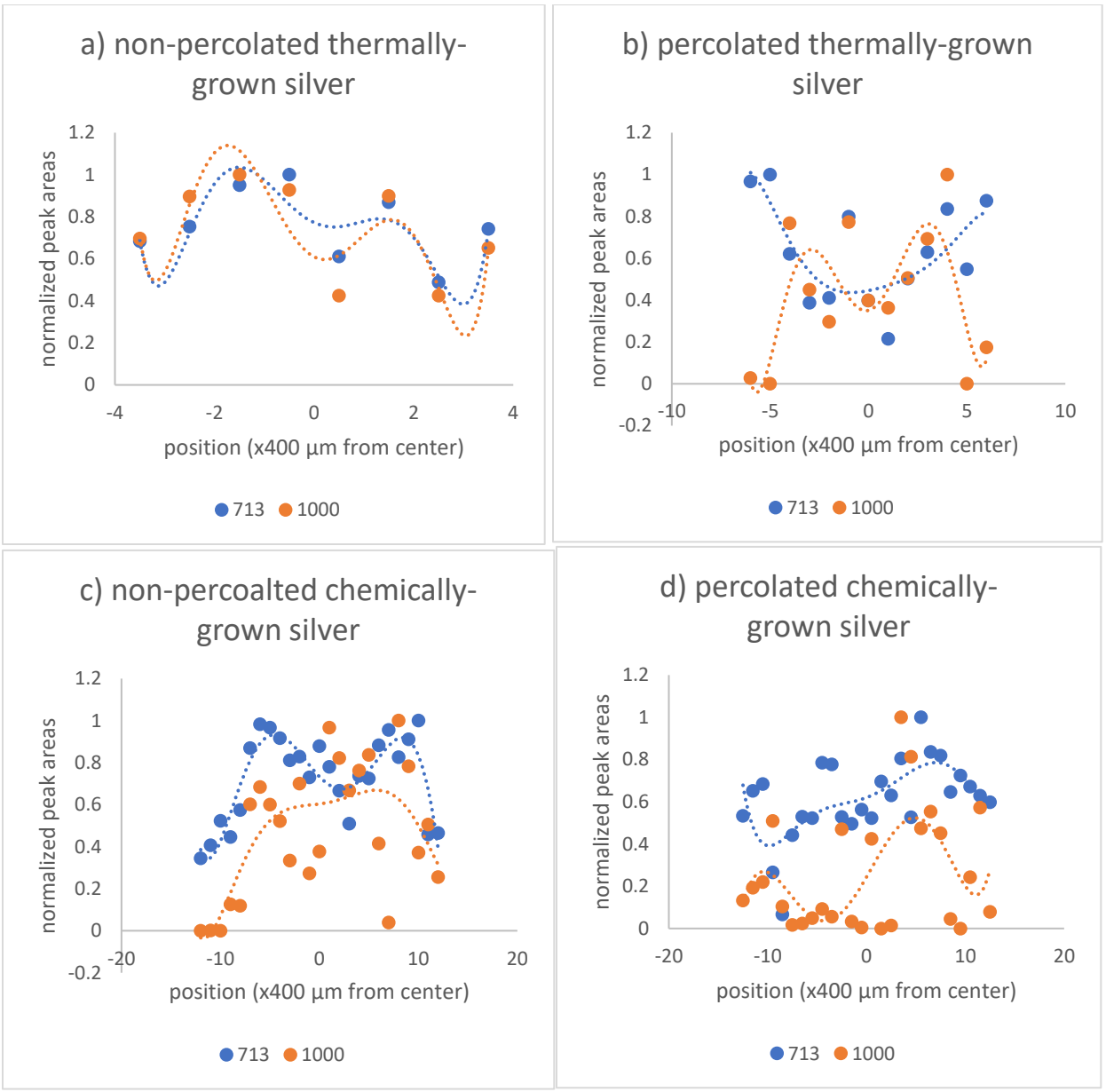

Figure A13: Comparing choline components from 1000 fits vs 713 fits for simulant stains on each substrate

A.3.2 Fitting semen data to 1000 cm^{-1} mode

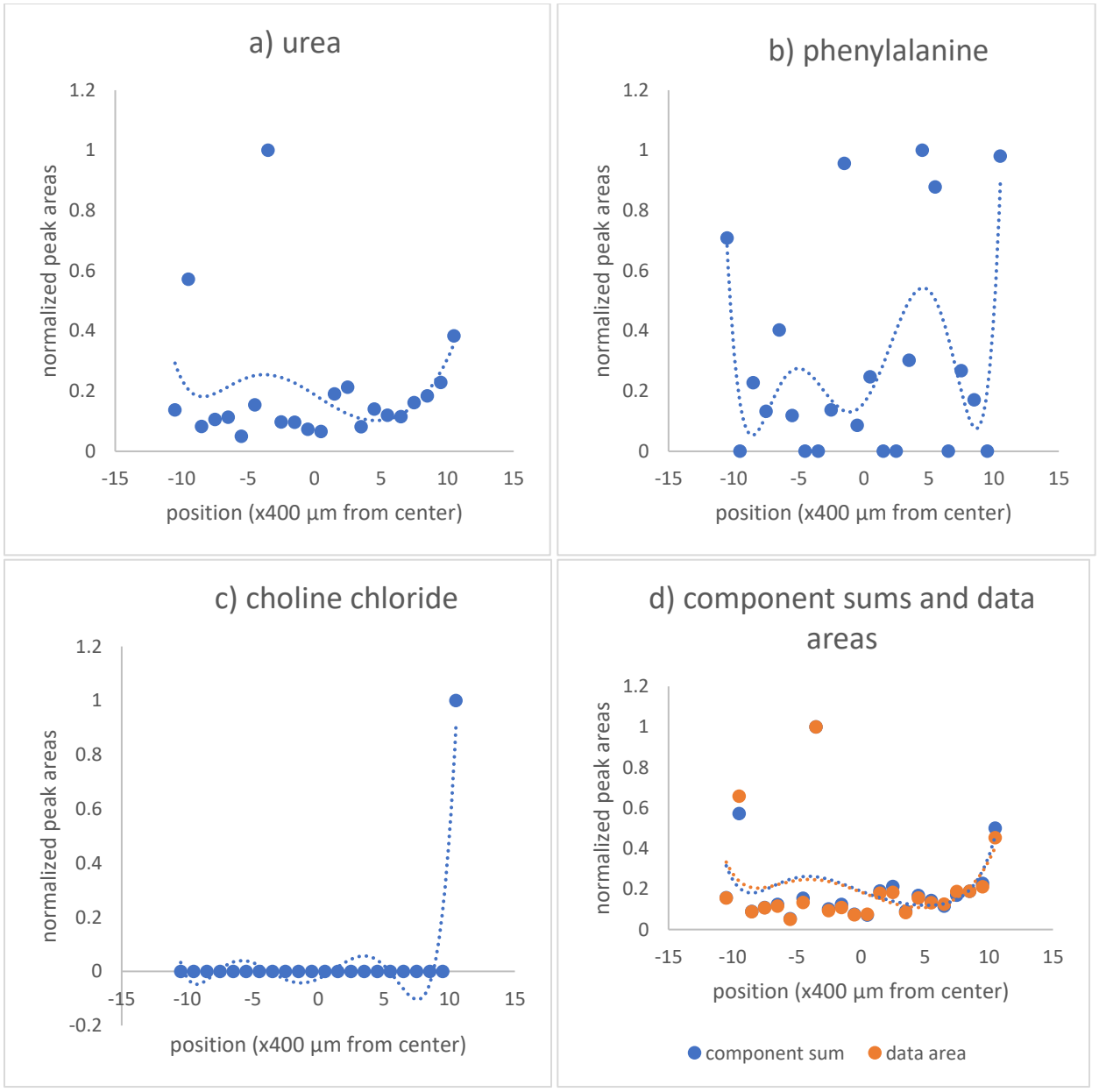

Figure A14: Peak areas of deconvoluted components of a) urea, b) phenylalanine, and c) choline chloride from the 1000 cm^{-1} mode of semen SERS spectra on non-percolated chemically-grown silver. In d), the sum of these components is given in blue, and the original data area is given in orange. All curves are sixth order polynomials.

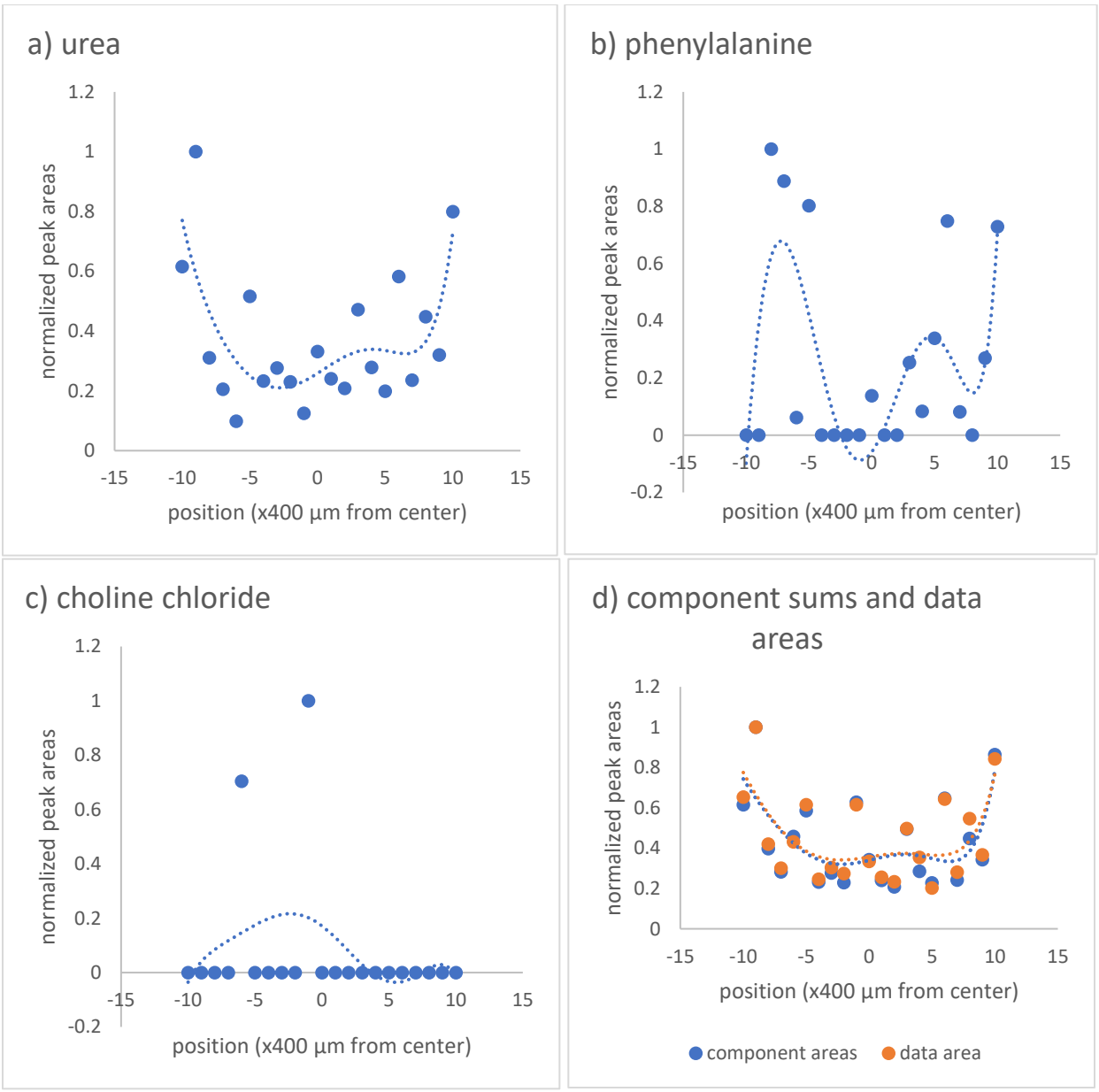

Figure A15: Peak areas of deconvoluted components of a) urea, b) phenylalanine, and c) choline chloride from the 1000 cm^{-1} mode of semen SERS spectra on percolated chemically-grown silver. In d), the sum of these components is given in blue, and the original data area is given in orange. All curves are sixth order polynomials.

A.4 Comparison of semen SERS spectra with a previous study

Table A1: Sum of squares of residuals between each pairing of spectra collected on AgNP-coated swabs from a previous study, as shown in Figure 7.

Comparisons	Sum of squares of residuals
7a vs 7b	52.6
7a vs 7c	81.6
7a vs 7d	70.7
7b vs 7c	79.2
7b vs 7d	69.3
7c vs 7d	78.2

Table A2: Sum of squares of residuals between reference semen spectra and line scans taken in this study.

a) Reference semen spectrum	b) collection of spectra for comparison to a)	Sum of squares of residuals for the spectrum in column b) with the closest match to that of column a)
7a	Non-percolated chemically-grown silver	44.4
7b	Non-percolated chemically-grown silver	29.5
7c	Non-percolated chemically-grown silver	51.4
7d	Non-percolated chemically-grown silver	27.3
7a	Percolated chemically-grown silver	50.8
7b	Percolated chemically-grown silver	28.4
7c	Percolated chemically-grown silver	41.8
7d	Percolated chemically-grown silver	55.5
Average of 7a-7d	Non-percolated chemically-grown silver	20.9
Average of 7a-7d	Percolated chemically-grown silver	34.9
Average of spectra collected from non-percolated chemically-grown silver	Non-percolated chemically-grown silver	4.46
Average of spectra collected from percolated chemically-grown silver	Percolated chemically-grown silver	15.1

A.5 Four-point probe measurement statistics

Table A3: Averages, standard deviations, and standard errors for thermally-grown silver layer conductivity values. Rows = layer thicknesses, columns = deposition rates. Coefficients of variation greater than one are shown underlined and in bold.

	3-4 A/s	**4-5 A/s**	**5-6 A/s**	**6-7 A/s**	**7-8 A/s**	**Ramp**
10 nm	Average (S): 4.49×10^{-4} St. Dev: 7.39×10^{-4} **Coeff of Var: 1.65**	Average (S): 7.62×10^{-10} St. Dev: 6.89×10^{-11} Coeff of Var: 0.0904	Average (S): 4.97×10^{-10} St. Dev: 1.97×10^{-10} Coeff of Var: 0.397	Average (S): 7.62×10^{-10} St. Dev: 5.39×10^{-11} Coeff of Var: 0.0708	Average (S): 7.42×10^{-10} St. Dev: 5.99×10^{-11} Coeff of Var: 0.0807	Average (S): 7.79×10^{-10} St. Dev: 5.91×10^{-11} Coeff of Var: 0.0759
15 nm	Average (S): 7.50×10^{-10} St. Dev: 8.62×10^{-11} Coeff of Var: 0.115	Average (S): 1.77×10^{-3} St. Dev: 3.83×10^{-3} **Coeff of Var: 2.17**	Average (S): 9.64E-03 St. Dev: 1.19E-02 **Coeff of Var: 1.24**	Average (S): 7.33×10^{-10} St. Dev: 7.92×10^{-11} Coeff of Var: 0.108	Average (S): 2.31×10^{-3} St. Dev: 3.57×10^{-3} **Coeff of Var: 1.55**	Average (S): 1.36×10^{-3} St. Dev: 2.52×10^{-3} **Coeff of Var: 1.85**
20 nm	Average (S): 0.0781 St. Dev: 0.0310 Coeff of Var: 0.397	Average (S): 1.09×10^{-3} St. Dev: 2.25×10^{-3} **Coeff of Var: 2.06**		Average (S): 0.0525 St. Dev: 0.0403 Coeff of Var: 0.767		Average (S): 0.0504 St. Dev: 0.0257 Coeff of Var: 0.510
30 nm	Average (S): 0.153 St. Dev: 0.0986 Coeff of Var: 0.644	Average (S): 0.0533 St. Dev: 0.0320 Coeff of Var: 0.600	Average (S): 0.395 St. Dev: 0.103 Coeff of Var: 0.260	Average (S): 0.439 St. Dev: 0.146 Coeff of Var: 0.334		Average (S): 0.370 St. Dev: 0.175 Coeff of Var: 0.473

Table A4: Averages, standard deviations, and standard errors for chemically-grown silver layer conductivity values. Coefficients of variation greater than one are shown underlined and in bold.

Time (min)	30	45	53	60
Average	8.21×10^{-10}	7.66×10^{-10}	7.44×10^{-10}	7.15×10^{-10}
St dev	3.49×10^{-11}	6.29×10^{-11}	4.77×10^{-11}	7.60×10^{-11}
Coeff var	0.0425	0.0821	0.0641	0.106

Time (min)	62	63	65	66
Average	0.0677	0.0192	0.0777	1.96×10^{-3}
St dev	0.0986	0.0292	0.190	4.79×10^{-3}
Coeff var	**1.46**	**1.52**	**2.44**	**2.44**

Time (min)	68	90	120
Average	0.409	0.145	0.634
St dev	0.360	0.154	0.354
Coeff var	0.880	**1.06**	0.559